Cavity Enhanced Magneto Optic Rotation

for Measurement of HO_2

A Thesis

Submitted to the Faculty

of

Drexel University

by

Michael Stichter

in partial fulfillment of the

requirements for the degree

of

Doctor of Philosophy

November 2016

Dedications

To my beautiful wife and our precious son.

In memory of Dr. Richard Billmers, who directed the initial development work on CEMOR.

Acknowledgements

I have very much appreciated the opportunity to work with a great group of people in the Mechanical Engineering Department at Drexel. In the total of eleven years the I have been a student in the department I have seen fellow students, faculty, and department heads come and go, yet I have formed lasting relationships with colleagues and friends alike. I wish to express recognition for several people who have contributed to my success.

I first thank my advisors, Dr. Nicholas P. Cernansky and Dr. David L. Miller who, in providing an opportunity to me to work with them, have shaped me as a person by guiding me through the doctoral process. I could not have chosen better mentors to apprentice under or friends to attend conferences with. Gratitude goes to the rest of my thesis advisory committee as well; Dr. E.C. Kumbur, Dr. Kevin Owens, and Dr. Tein-Min Tan. They have pushed me to be a better researcher and communicator.

My previous laser labmates, Jamie Lane and Liang Wu, have significantly contributed to my development as a laser spectroscopist and provided many enlightening discussions on related topics. Undergraduate students, Andy Gnias, Hannah Talisse (REU), Ilya Semenov (REU), performed several helpful computational, data acquisition, and control tasks and were gracious mentees. Fellow Combustion Chemistry groupmates Julius Corrubia, Farinaz Farid, Yulei Li provided opportunities to broaden my experimental combustion research and assistance with challenges in my own work.

Jeremy Robbins was instrumental in setting up the magnetic field strength work. His programming assistance in modeling using FEMM, controlling the resonance tracking system, and monitoring the lab temperature and humidity was invaluable. Our discussions about best practices and troubleshooting benefited both of us in our laboratory work and careers afterward.

Dr. Richard Billmers offered his help in the continued development of CEMOR; I wish we would have had more time to discuss the intricacies of the project.

My family deserves much thanks. They have loved and encouraged me throughout the process. I would not have started–and I could not have finished–this endeavor without their support. My wife, Jessica, has generously stood with me through the joys and challenges of this work and has been a strong partner in numerous ways. The arrival of our son, Harvey, gave me a deadline for

completion. I am thankful for that.

Finally, I acknowledge the National Science Foundation for supporting my initial work with spectroscopy of Plasma Enhanced Combustion through CBET-0755632, the initial exploratory period of this project through an NSF EAGER Grant CBET-1142312, and the development period of CEMOR under NSF grant CBET-1335760.

Table of Contents

List of Figures

Abstract

Cavity Enhanced Magneto Optic Rotation
for Measurement of HO_2

Michael Stichter

Advisors: Nicholas P. Cernansky, PhD and David L. Miller, PhD

The goal of reduced emissions and increased efficiency in transportation has required investigation into advanced engine designs. Some of these advanced engines use charge reactivity to closely control the engine ignition and combustion process and thus the overall engine operation. Reactivity controlled operation requires models of the chemical kinetics at the low end of operating temperatures. The current models are lacking detail in the low and intermediate temperature region where hydroxyl (OH), hydroperoxy (HO_2), and alkylperoxy (RO_2) radicals play an important role in the oxidation chemistry. Measurement of these radicals is made difficult in combustion systems because of the strongly absorbing stable products of combustion, such as CO_2 and H_2O, which obscure the absorption features of HO_2 and RO_2. Therefore, there is a need for sensitive and selective diagnostics which can quantitatively measure these weakly absorbing small peroxy radicals in combustion systems.

This work advances the development and application of a sensitive and selective laser diagnostic technique called Cavity Enhanced Magneto-Optic Rotation (CEMOR) for quantitative measurement of paramagnetic species, specifically HO_2 radicals. CEMOR combines the sensitivity of cavity ringdown spectroscopy (CRDS) and the selectivity of magneto-optic rotation (MOR) spectroscopy.

This work presents a novel design of CEMOR with a continuous wave laser source for measurement of HO_2. The narrower bandwidth of continuous wave lasers offers increased spectroscopic resolution over the pulsed Nd:YAG/OPO laser used for previous CEMOR development. Continuous wave cavity ringdown spectroscopy (cw-CRDS) is integrated with MOR in order to make high resolution scans of HO_2 in a flash photolysis cell.

Modeling results of the magnetic field strength in studies of MOR and CEMOR with a slot burner using permanent magnets, and of CEMOR in a flash photolysis cell using a solenoid are presented. Magnetic field strength effect is shown to have a linear relationship with MOR signal

and a mechanism for measurement of its effect on CEMOR signal is described.

The objective of this dissertation is to demonstrate that CEMOR can be used to make measurements of HO_2 by increasing its resolution through the incorporation of a continuous wave distributed feedback (DFB) diode laser. The intellectual merit of this work is found in the design of a novel laser spectroscopy technique which is capable of sensitive and selective detection of paramagnetic species. This initial work did not demonstrate successful application of continuous wave CEMOR to measurement of HO_2, yet it provides a path forward for this goal in a flash photolysis cell and cool flame burner. The present work also provides a method which can easily be adapted to measurement of alkyl peroxy (RO_2) radicals.

1. Introduction

Combustion remains the most common energy utilization method. In 2014, US consumption (by combustion) of liquid fuels reached 33 quadrillion BTU (see Figure 1.1). While oil prices are less than $50 per barrel, consumption is at 90 million barrels per day, prompting a desire to reduce oil usage. There is great interest in developing novel engine designs which reduce emissions and increase fuel efficiency, while not significantly decreasing stability of the combustion process. These designs operate in Low Temperature Combustion (LTC) conditions where control of the combustion cycle comes from preignition reactivity. To develop these engines, further understanding of the underlying combustion chemistry is necessary. Predictive modeling of new engine concepts for a changing fuel stream requires detailed understanding of the autoignition chemistry of a large set of organic molecules over a wide range of pressure and temperature.

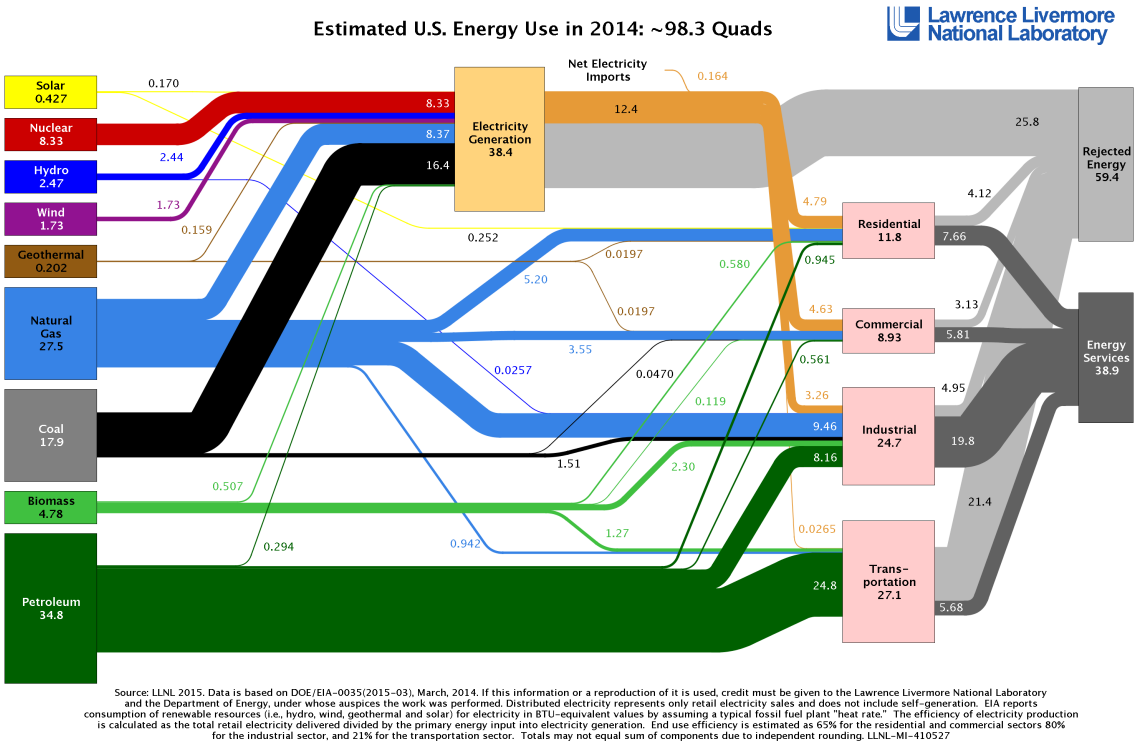

Figure 1.1: Estimated energy usage flow chart by source and usage. (U.S. Department of Energy)

Small peroxy radicals play an important role in combustion chemistry as well as atmospheric chemistry (Taatjes and Oh, 1997; Johnson et al., 1991; Wood and Charest, 2014). Peroxy and hydroperoxy radicals are particularly important in ignition chemistry, specifically in the low-temperature region (less than ∼900 K) (Zádor et al., 2011). Diagnostic techniques which can measure these radicals in reacting environments are important in the development of models of chemical kinetics. At present, combustion chemical kinetic models lack detail in the low temperature combustion region. Several studies have measured OH radicals in combustion environments using standard diagnostics, however small peroxy radicals (i.e., HO_2 and RO_2) have been more difficult to measure, due to their relatively small absorption cross section and spectral overlap with stable species such as H_2O and CO_2, the main products of combustion and hydrocarbon oxidation.

1.1 Thesis Overview

The objective of this work is to develop a laser diagnostic technique that can sensitively and selectively measure paramagnetic species. This work specifically focuses on demonstrating that cavity enhanced magneto-optic rotation (CEMOR) can be used to make measurements of HO_2 in a photolysis cell by increasing its resolution through the use of a continuous wave distributed feedback (DFB) diode laser.

The CEMOR spectroscopy method (Emig et al., 2002b) was developed at Drexel University more than a dozen years ago, and proved its capability to provide sensitive and selective measurements of paramagnetic species in a combustion flame. With the goal of application of CEMOR to measurements of HO_2, CEMOR was recently presented by Lane (2012) to measure [OH] in a lean methane-air flame with high spatial and temporal specificity. His research demonstrated an increased sensitivity over MOR and near the detection limit of CRDS for [OH]. He concluded that, for application to [HO_2] measurements in our photolysis cell, there were two deficiencies in the existing CEMOR setup:

1. The magnetic field strength is too low to have a strong signal (sufficient signal to noise) and
2. The laser linewidth is too broad to resolve the spectral features of HO_2

These deficiencies need to be addressed in order to make measurements in the flash photolysis cell (FPC) and in burners.

Previous researchers at Drexel have taken steps in order to develop CEMOR as a diagnostic tool. These steps include development of the experimental setup, calibration with known concentrations, and analysis using theory to understand the results. This same approach is being used to continue the development of CEMOR.

The initial work was based on measurement of a known concentration of paramagnetic atomic gallium atoms aspirated into an acetylene-air flame. Gallium was used because it is a simple atom whose spectroscopy is well understood and it does not interact with the combustion process. To demonstrate the selective potential of CEMOR, gallium atoms were measured by MOR in the presence of non-paramagnetic laser dye which would overlap the spectrum in standard absorption spectroscopy (Fig 2.1).

The next phase of CEMOR development focused on measurement of OH in a lean methane-air slot burner flame (Lane, 2012). The hydroxyl radical (OH) is an important and well characterized radical in combustion chemistry and is also paramagnetic so it provided a good platform for this stage of development. Cavity Ringdown Spectroscopy (CRDS) and laser induced fluorescence (LIF) were used to establish calibration OH concentrations for later measurement using MOR and CEMOR. Using the CRDS and LIF results as the baseline, CEMOR was demonstrated to detect OH in a real combustion system and provide higher sensitivity than MOR, on the order of the sensitivity of CRDS.

In order to further the development of peroxy radical detection, a flash photolysis cell (FPC) facility was developed to provide a calibrated source of HO_2 for CEMOR development work. Both CRDS and CEMOR were applied to this facility. The results of CRDS and CEMOR measurements of HO_2 in the FPC showed promise for further development work, but also demonstrated limitations of the pulsed CEMOR diagnostic method. Analysis of these results showed that the linewidth of our pulsed Nd:YAG laser was too broad to resolve the spectral features of HO_2 in the region of interest, the low lying electronic band ($A^2A' \leftarrow X^2A''$) near 1430 nm (7000 cm^{-1}). Additionally, the electromagnetic solenoid coil did not provide sufficiently large Zeeman splitting to observe a detectable CEMOR signal.

This dissertation presents the progress made on several tasks to improve the CEMOR method for sensitive and selective measurement of peroxy radicals in complex reacting environments.

The first part of Chapter 2 describes the development of diagnostic skills by applying established spectroscopy techniques to a related and important observation of long OH lifetimes in a plasma enhanced combustion system. A background on CRDS—including cw-CRDS—is included. The theories of MOR and CEMOR are described. A survey of methods that have been applied to measurement of HO_2 is provided in this chapter. A brief review of combustion chemistry, specifically the importance of reaction intermediate radicals OH, HO_2, and RO_2 in chemical kinetics is presented.

Chapter 3 describes the experimental facilities and procedures employed in this research work; slot burner, Flash Photolysis Facility, and stabilized flame facilities for experimental HO_2 studies.

The next two chapters discuss the results and roadblocks to progress. Chapter 4 focuses on the development of CEMOR. It describes the research objectives and goal of measurement of peroxy radicals. It also includes investigation into the magnetic fields used in previous CEMOR measurements and the effects of magnetic field strength on MOR.

Chapter 5 summarizes previous measurements made of HO_2 using CRDS with a pulsed laser and further analyzes the signal. This chapter also includes preliminary results of modeling study of HO_2 in a photolysis cell.

Chapter 6 provides a summary and intellectual merit of and conclusions resulting from this work, and provides recommendations for future related work as well.

2. Background and Literature Review

The background is divided into six sections. Section 2.1 discusses plasma enhanced combustion study of H_2 and C_1 to C_3 alkanes by monitoring [OH] using LIF. This study was undertaken to develop necessary diagnostic skills by investigating the paramagnetic OH radical in an important and related exploration of pre-ignition reaction chemistry.

Section 2.2 discusses the two spectroscopic techniques which combine to form cavity enhanced magneto-optic rotation (CEMOR): cavity ringdown spectroscopy (CRDS) and magneto-optic rotation (MOR). These sections describe their theory of operation and application of them to combustion related molecules. The CRDS section (2.2.4) addresses the separate methods based on pulsed (p-CRDS) and continuous wave (cw-CRDS) laser sources. Section 2.3 describes methods to enhance the sensitivity of MOR. Section 2.4 presents a similar review of the CEMOR spectroscopy method and potential improvements on it. Section 2.5 describes the theory of cw-CEMOR and the development and application of similar methods.

Section 2.6 provides a brief review of low temperature combustion chemistry and specifically focuses on the small peroxy radicals HO_2 and RO_2. And the final section describes the reaction chemistry in the flash photolysis cell.

2.1 LIF for Plasma Enhanced Combustion Studies

Skills in the basics of LIF and CRDS spectroscopy presented in this work were developed while working on the NSF CBET-0755632 project "Role of Excited Species in Plasma Enhanced Combustion". The results of that work were presented by Wu (2013), and key findings are presented here. The goal of that work was to measure excited species in the afterglow of a non-equilibrium nanosecond pulse plasma under various conditions in order to determine fundamental mechanisms which promote autoignition and combustion. The study focused on determining the effects of various species generated in a corona discharge on fuel-air mixtures. The main method of monitoring the reaction was laser induced fluorescence (LIF) (described in Section 2.2.1) of the OH radical.

The experiments were performed using a reactor which heated fuel-air mixtures at low equiv-

alence ratio ($\Phi = 0.1$) and flowed it over a low temperature plasma (Wu et al., 2010). Methane, ethane, propane, butane, and hydrogen were used as fuels in these experiments. The resulting time evolution of OH after the plasma pulse indicated long lifetimes of the excited radical which were not predicted by models. The OH lifetime was longer as temperatures increased (500→800 K). Cool flame behavior was observed when using propane (C_3H_8) and butane (C_4H_{10}) at temperatures above 500 K. These two fuels are the smallest ones which exhibit two stage ignition behavior.

Two additional laser spectroscopy techniques were used in this project (Wu et al., 2011b). In order to observe the spatial distribution of the OH radical, planar LIF (PLIF) measurements were taken. In PLIF experiments, the laser was spread into a sheet and the resulting two dimensional picture of fluorescence was recorded using an intensified charged coupled device (ICCD) camera. The PLIF images showed that the dynamics of the OH radical were uniform in the channel of the plasma discharge. For absolute concentration measurements of OH, cavity ringdown spectroscopy (CRDS) was used, the results of which agreed with the LIF measurements made previously.

In order to find the route to the long lifetime of OH radical concentration, experiments were performed to determine whether NO and vibrationally excited nitrogen (N_2 X^1 $\Sigma(\nu > 0)$ represented as $N_2(\nu)$) were contributing (Wu et al., 2013). Addition of 50-100 ppm NO had little effect on the OH lifetime. A "synthetic air" mixture consisting of 80% CO_2 and 20% O_2 was used to in place of compressed air to test whether removal of N_2 from the reactant gases had an effect on OH. Use of the synthetic air significantly reduced the OH lifetime. Further investigation into this pathway is needed, and direct measurement of $N_2(\nu)$ and HO_2 will be illuminating. Additional studies with different spectroscopic techniques will need to be applied in order to effectively measure these molecules. Coherent Anti-Stokes Raman Spectroscopy (CARS) can measure the $N_2(\nu)$. The CEMOR technique may contribute to the necessary spectroscopy developments to measure HO_2 under these conditions.

2.2 Absorption Spectroscopy

The fundamental concept of absorption spectroscopy is that atoms and molecules absorb radiation at wavelength-specific levels due to the interaction of the radiation with the individual structures

of nuclei and electrons. The details of atomic and molecular structure are covered elsewhere (for example, books by Herzberg (1945); Herzberg and Spinks (1944) and textbooks by Incropera (1974) and Laurendeau (2005)) and only briefly covered here.

In direct absorption spectroscopy, the attenuation of radiation (usually light) is measured where the intensity transmitted through the sample can be given by the Beer-Lambert law

$$I = I_0 e^{-\alpha d} \tag{2.1}$$

where I_0 is the incident light intensity, α is the absorption coefficient, and d is the interaction pathlength of the sample. In the simplest case of a single species being present, the frequency dependent absorption coefficient is given by

$$\alpha(\nu) = N\sigma(\nu) \tag{2.2}$$

where N is the number density (molecules per volume) of the absorbing species, $\sigma(\nu)$ is the frequency dependent absorption cross-section, and ν is the radiation frequency. All of the species which absorb at specific frequency—and within the linewidth of the laser—contribute to the signal attenuation. In order to account for the entire frequency attenuation observed, a summation of all absorption and scattering losses should be performed.

For single pass absorption spectroscopy, the sensitivity is limited because the information contained in the signal is a small change in intensity against a large background. The large pulse-to-pulse intensity fluctuations of a pulsed laser make it poorly suited to sensitive measurements with direct absorption spectroscopy. Indirect methods have been used to make sensitive measurements using pulsed lasers by measuring an effect of the absorption rather than the absorption directly. Laser induced fluorescence (LIF, see Section 2.2.1) is an example of indirect absorption which measures the intensity of light emitted at a different frequency due to electronic excitation caused by the incoming laser pulse. The subsequent relaxation from the excited state emits light which is collected and measured. The LIF technique has become commonplace in combustion chemistry measurements and has been used in our lab to measure OH in a slot burner (Lane, 2012) and a nanosecond pulsed plasma reactor (Wu et al., 2011a). Indirect absorption techniques like LIF

have high sensitivity, but only provide a relative absorption coefficient and are not self-calibrating. In contrast, direct absorption spectroscopy provides an absolute (frequency dependent) absorption coefficient.

By inspection of equation 2.1, the sensitivity of direct absorption spectroscopy is dependent on the interaction pathlength, d. The sensitivity of this method can then be improved by increasing d through multi-pass configurations such as a Herriott cell (Herriott et al., 1964) or a White cell (White, 1976). These methods rely on highly reflective mirrors which direct the laser beam along several paths through the sample of interest. Higher sensitivities are achieved by increasing the number of passes which requires larger sample volumes in order to maintain the separation required. Crossed beams cause interference fringes which increase the noise and should be avoided. Ju has used a 21 pass Herriott cell for sensitive measurements of OH and HO_2 (Ju et al., 2016). The multiple passes extend the pathlength to 19.17 m in their bench top cell.

Rapid frequency modulation (f_m approx. 100 MHz) can improve sensitivity by detecting high frequency absorption at a faster rate than the laser noise. The theory is that this method rejects the lower frequency noise and shows no signal unless there is absorption or phase shift of the signal. In practice, the frequency modulation is performed at the same time as some amplitude modulation due to the rapid scanning from modulating the current to the laser. This method can be combined with multipass cells to improve sensitivity even further (Bomse et al., 1992).

To shrink the sample volume, yet increase the absorption pathlength, all of the passes in the sample cell can be overlapped. This will significantly increase the interaction path length where the limits come from the absorption and scattering from a sample, and the transmission losses through the mirrors. This is what prompted cavity ringdown spectroscopy and thinking of the cavity with highly reflective mirrors (a high finesse cavity) as a storage volume for light.

While multipass and cavity ringdown methods increase the sensitivity of direct absorption spectroscopy, they are unable to differentiate between overlapping spectra from different molecules. As pressure increases, this becomes even more challenging because of broadening of the spectral lines. Methods to increase the selectivity for specific molecules became important in reacting systems with multiple species in the same volume.

2.2.1 Laser Induced Fluorescence

Saturated laser induced fluorescence (LIF) is an indirect laser spectroscopy technique whereby a laser pulse at a selected wavelength excites a species from a specific quantum state (electronic, vibrational, rotational) to a higher energy quantum state. Upon excitation to the higher energy state and a delay of a few nanoseconds, the excited species releases fluorescent radiation at a measurably but slightly longer wavelength. This longer wavelength light can usually be filtered out from the background by a bandpass filter and then collected by a suitable detector. The intensity of the signal is correlated to the concentration of the species which fluoresces. This is an indirect method of measurement, yet is sensitive to OH and several other short lived molecules of interest in combustion. It has found widespread use in monitoring OH, CH, and NO in combustion systems, where a significant database of spectroscopic and quenching parameters is available (Kohse-Höinghaus and Jeffries, 2002). The signal can be collected by sensitive detectors such as photomultiplier tubes and photodiodes.

For OH measurement, 283 nm light can excite the initial ground $X^2\Pi$ electronic state to the first excited $A^2\Sigma$ state. A portion of the energy is then released by fluorescence at 308 nm or by quenching. Because other pathways that do not radiate can also be taken when the energy is released, they must be considered when attempting quantitative interpretation of the LIF signal Wu (2013).

The excitation to upper energy state occurs by absorption of photons from the laser source. At the same time, laser photons can cause stimulated emission which removes energy from the upper state. The rate of absorption is linearly dependent on the Einstein B coefficient as shown;

$$W_{12} = \frac{I_\nu B_{12}}{c} \tag{2.3}$$

where W_{12} is the absorption rate, B_{12} is the Einstein B coefficient, I_ν is the laser irradiance, and c is the speed of light. The stimulated emission rate, W_{21} is similar;

$$W_{21} = \frac{I_\nu B_{21}}{c} \tag{2.4}$$

Planar LIF (PLIF) uses the same absorption and emission concept as LIF, but the detection is performed by a fast gated camera (nanosecond) to capture a two dimensional image of the fluorescence on an array of photodetectors.

2.2.2 CRDS and MOR Spectroscopy

Magneto optic rotation (MOR) describes the effect of the rotation of the plane of polarization of linearly (plane) polarized light due to interaction with a paramagnetic species in an external magnetic field. The magnetic field causes Zeeman splitting of electron states of paramagnetic species and makes it optically active. In MOR, linearly polarized light is applied to a sample in an external magnetic field between two crossed polarizers. The detected signal increase, measured after the second polarizer, is a function of number density and interaction pathlength. MOR allows selective detection of paramagnetic species in crowded spectral regions as shown by Emig et al. (2002b), Fig. 2.1.

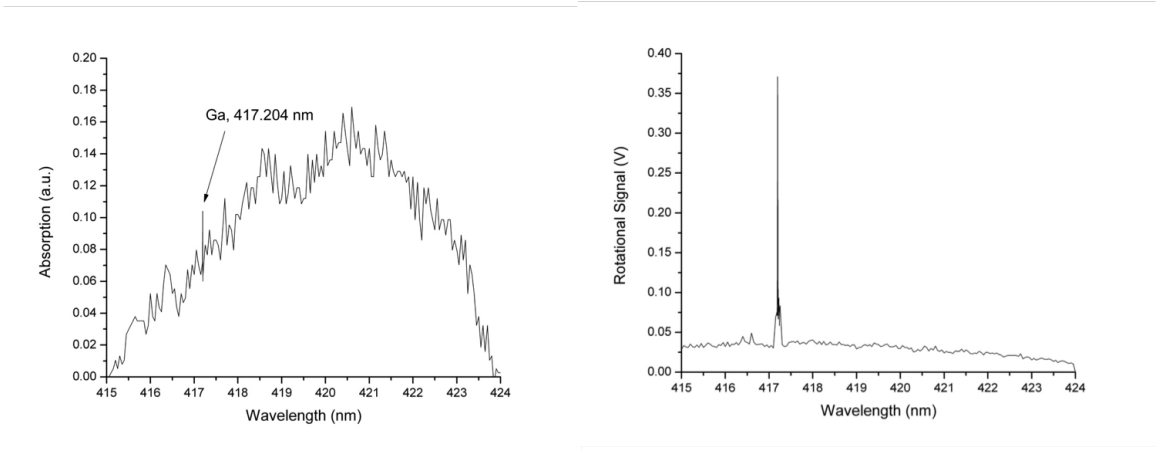

Figure 2.1: Ga line is obscured in a traditional absorption experiment due to strong absorption from C540a laser dye, and the line is clear using MOR (Emig et al., 2002b).

Cavity ringdown spectroscopy is a sensitive form of absorption spectroscopy often applied to measuring the absolute concentration of trace gases and is capable of measurements at sub-ppm levels. In CRDS, a high finesse optical resonator (Fabry-Perot cavity) is used where the high mirror

reflectivity increases interaction pathlength of the laser with absorbing species by making many multiple passes through the species of interest. Ringdown mirrors with reflectivity greater than 99.9% are most commonly used. For pulsed CRDS, the ringdown happens because an incident laser pulse resonates in the cavity, diminishing exponentially with time as the small portion transmitted through the second mirror is monitored by a sensitive detector. The increased pathlength increases detection sensitivity, and the increase in sensitivity is dependent on mirror reflectivity. The decay rate is measured and plotted versus laser frequency to provide an absorption spectrum. Measurement of the rate of decay, rather than absolute beam attenuation, is particularly useful for pulsed laser systems where there are large pulse-to-pulse energy fluctuations.

A brief introduction and review of CRDS theory is contained in Sec 2.2.4. For useful introductory discussions see Scherer et al. (1995); Zalicki and Zare (1995); Wilson (1996); Paul and Saykally (1997), and for more detailed review see Paldus and Kachanov (2005).

2.2.3 Magneto-Optic Rotation Spectroscopy

Magneto-optic rotation (MOR) spectroscopy, also called magnetic rotation spectroscopy (MRS), is a method which utilizes the optical activity caused by interaction of light with paramagnetic species in the presence of a magnetic field. For more detail on the spectroscopic fundamentals that describe this interaction see for example Steinfeld (2012); Incropera (1974); Herzberg (1945).

A brief history of MOR starts with Michael Faraday, who in 1862 experimented with the alteration of light with a magnetic field. Experimentation to further understand the theory inspired Zeeman to make the first successful observation of the widening and splitting of sodium D lines and published his description (Zeeman, 1897), a discovery that earned him and his advisor, Lorentz, the Nobel Prize in Physics. At that time, they knew about electromagnetism and that there was something about certain molecules that responded to the magnetic field. In the early application of this discovery, the visible emission spectrum was monitored from a flame onto a dark background. Later, Thomas Carroll observed magnetic rotation by passing polarized light from an arc lamp through a cell where he generated I_2, K_2, and Na_2 and recorded the absorption spectrum on photographic plates (Carroll, 1937, 1936). After World War II, microwave sources saw more widespread use in scientific applications and by 1955, Townes and Schawlow were using masers in MRS experiments

(Townes and Schawlow, 1955). Shortly after that, the first Ruby laser was demonstrated earning both Townes and Schawlow Nobel prizes. Kankare and Stephens (1980) presented a unified theory in magneto-optic phenomena observed in analytical spectroscopy.

Magneto-optic rotation is a sensitive spectroscopy technique which exploits the Zeeman effect to make measurements of paramagnetic species in an external magnetic field. In MOR, the plane of polarization of linearly polarized light rotates due to birefringence and dichroic effects as the light travels through the analyte gas species in a magnetic field. The magnetic field causes splitting of spectral lines each one having a different index of refraction (causing birefringence and a rotation in the plane of polarization) and absorption coefficient (causing dichroism and an ellipticity to the polarization (as well as rotation of polarization)).

Where a laser beam is propagating in the z direction, the beam can be described with oscillation orthogonal electric, $\mathbf{E}$, and magnetic, $\mathbf{H}$, vectors which are functions of space and time and form a transverse wave. For linear polarization, the propagating fields stay in plane until acted upon otherwise and the polarization is taken as the transverse plane of the electric field.

Two configurations describe the external magnetic field orientation $\mathbf{B}$ in relation to the laser propagation. They are the Faraday configuration and the Voigt configuration. In the Faraday configuration the $\mathbf{B}$ field is parallel to the direction of laser propagation such that the light waves are in a transverse orientation to the applied magnetic field independent of the direction of linear polarization. In the Voigt configuration, the laser propagates orthogonal to the direction of the $\mathbf{B}$ field.

Each configuration has different selection rules for the shift in spectra. Based on the selection rules, the light which interacts with molecules in a Voigt configured (transverse) external magnetic field will demonstrate linear birefringence and dichroism (the Voigt effect). In a Faraday configured (longitudinal) magnetic field, the left and right circularly polarized components [1] of the $\mathbf{E}$ vector of the laser interact with the left and right circularly polarized components of the Zeeman absorption multiplet.

For both the Faraday and the Voigt configuration of the external magnetic field and the laser

[1] linear polarized light can be considered as a combination of left and right circularly polarized light propagating collinearly and in phase.

propagation, the incident light is polarized in a known direction before crossing the analyte and collected after a polarizer which is crossed ($\pi/2$) with it. In the Faraday configuration, the incoming light polarization can be set arbitrarily because the $\mathbf{E}$ polarization is always transverse to the applied $\mathbf{B}$ field. In the Voigt configuration, greatest sensitivity is achieved by making the polarization plane of the light ($\mathbf{E}$) be at an angle of $\pi/4$ with the applied magnetic field. Kankare and Stephens (1980) have shown that theoretically the Faraday configuration has a better maximum sensitivity by approximately 1.5 at magnetic field strengths near optimum, whereas at low magnetic field strengths, the advantage of Faraday is greater because the transmitted intensity from the Voigt configuration depends on the fourth power of the magnetic field. This also means that at high magnetic field strengths the advantages changes to the Voigt configuration.

Some examples of MOR applied to radicals important to combustion can be found in studies by Brecha et al. (1997); Pfeiffer et al. (1981) and Lane (2012). The MOR concept has been applied in combination with sensitive techniques to make measurements of paramagnetic species; for example, O_2 (Engeln et al., 1998), HO_2 (Ju et al., 2016), and OH (Lane, 2012).

2.2.4 Cavity Ringdown Spectroscopy

Cavity Ringdown Spectroscopy (CRDS), alternatively called Cavity Ringdown Laser Absorption Spectroscopy (CRLAS), was first demonstrated as a method to measure trace gases by O'Keefe and Deacon (1988). The concept of measuring the rate of decay of light in a high finesse cavity was first demonstrated by Anderson et al. (1984) as a method to measure the reflectivity (R) of a set of mirrors. While Anderson et al., used a continuous wave laser in their experiments, the majority of early development of CRDS was performed with pulsed laser sources.

The version of CRDS which uses a pulsed laser was recently applied to measurement of [OH] in a slot burner at Drexel (Lane, 2012) and as a method to evaluate and calibrate the development of CEMOR. For this reason, and because it is likely simpler to explain, this first section will cover pulsed CRDS.

Pulsed CRDS

Pulsed CRDS is easiest to first describe and understand as a 'photon bullet model', which considers a group of photons bouncing back and forth between two mirrors with an exponential decay in intensity as a small portion is transmitted through the mirrors on each pass. In pulsed CRDS, the light acts more like a particle than a wave, when the pulse duration is less than the roundtrip time within the laser cavity (FWHM < t_r). The signal from a suitable detector placed after the exit mirror will record a string of decreasing intensity pulses with a separation of the round trip time of the cavity, $t_r = 2L/c$. The intensity of this signal decays because of transmission through the mirror and absorption within the cavity. In theory, $T = 1 - R$, but in practice $T \approx 0.1$ to $0.5 * (1 - R)$ because of absorption and scattering losses which are not included in the measured value of R (Berden and Engeln, 2009).

The envelope of the signal exiting the cavity can be described by a slightly different form of the Beer-Lambert equation:

$$I(t) = I_0 e^{-\frac{t}{\tau}} \tag{2.5}$$

where τ is the "ringdown time" of the cavity; the time for $I = I_0/e$. A shorter ringdown time indicates increased losses through absorption and scattering. Where the ringdown mirrors have equal reflectivity and $R \approx 1$, $\ln R \approx -(1 - R)$, so the ringdown time is given by:

$$\tau = \frac{L}{c(1 - R + \alpha d)}. \tag{2.6}$$

From (Berden and Engeln, 2009), the ringdown time in an empty cavity is dependent on the mirror reflectivity, R, the distance between the ringdown mirrors, L, and the speed of light, c. As stated in 2.2, all absorption and scattering losses should be summed that contribute to $\alpha(\nu)$, for a more general case of τ:

$$\tau(\nu) = \frac{L}{c\left[1 - R(\nu) + \Sigma_i \sigma_i(\nu) \int_0^d N_i(x)\,\mathrm{d}x\right]} \tag{2.7}$$

The summation is over all i species with absorption and scattering cross-sections $\sigma_i(\nu)$ and the

number density integrated over the absorption line given as $\int_0^d N_i(x)\,\mathrm{d}x$.

Over a small wavelength range, the wavelength dependent mirror reflectivity and scattering losses can be considered constant over the absorption feature. Where the contributers to the absorption spectrum are known and not overlapping, the absorption losses at a specific wavelength can be given by $\sigma_a N_a l_a$. Because of this, the difference between τ on resonance with the absorption feature and τ off resonance, but very close by, can be considered to come solely from absorption losses. With known path lengths and wavelength dependent absorption cross-sections, the number density is the remaining variable contributing to the difference in τ. Where the cavity decay rate is $k_\nu = 1/\tau$:

$$k_\nu = \frac{1-R}{L} + \alpha_\nu \frac{d}{L} \tag{2.8}$$

and

$$\left(\frac{1}{\tau_{on}} - \frac{1}{\tau_{off}}\right) = \frac{c}{L}\left(\sigma_0 N_a l_a\right) \tag{2.9}$$

where

$$\tau_{on} = \frac{L}{c\left[(1-R) + NAL + k_\nu l\right]} \tag{2.10}$$

$$\tau_{off} = \frac{L}{c\left[(1-R) + NAL\right]} \tag{2.11}$$

The concentration of the absorbing species is then,

$$N = N_a = \frac{L}{cl\sigma_0}\left(\frac{1}{\tau_{on}} - \frac{1}{\tau_{off}}\right) \tag{2.12}$$

substituting

$$\sigma_0 = h\nu_0 B_{ij} f_b \tag{2.13}$$

where B_{ij} is the Einstein B coefficient for absorption at the desired transition and f_b is the Boltzmann fraction at the lower energy level. A more useful integral form where all contributions at that

wavelength can be included in the count:

$$N = \frac{L}{clh\nu_0 B_{ij} f_b} \int_{-\infty}^{\infty} \left(\frac{1}{\tau_{on}} - \frac{1}{\tau_{off}} \right) dv \tag{2.14}$$

Optical Cavity Properties A more accurate conceptual model of CRDS is not the 'photon bullet' described above, but that of a high finesse etalon. To understand this more fully, we need to discuss the properties of optical cavities. A description of optical resonators is included in this section. A more complete explanation is available in (Siegman, 1986).

A passive optical cavity (Fabry-Perot) is characterized by the quality of its resonance (the finesse, F). The finesse is given as:

$$F = \frac{\pi\sqrt{R}}{1-R}, \tag{2.15}$$

where R is the reflectivity of the mirror pair.

High finesse cavities have longer effective path lengths because the light stays in the cavity longer upon ringdown. This same quality means that they can achieve higher maximum power within the cavity.

An optically stable cavity is important in CRDS measurements to achieve long ringdown times. In order to ensure stability, the length of the cavity, L, and the radius of curvature, RoC, of the mirrors should be specifically selected. There are so called g-parameters which are used to describe a cavity;

$$g_n = \left(1 - \frac{L}{RoC_n} \right), \tag{2.16}$$

where RoC_n is the radius of curvature of the mirror and n is the mirror index. In some cases mirrors with different radius of curvature are used to form the optical cavity. Stability of the cavity is achieved when $0 \leq g_1 g_2 \leq 1$. Which means that an optical cavity is stable between two identical mirrors if $0 < L < r$ or $r < L < 2r$.

An optical cavity is resonant with a specified wavelength of light when the distance between the mirrors is a multiple of the half wavelengths, $n\lambda/2$, where n is an integer. This is a necessary requirement for constructive interference. There can be multiple modes within a cavity of any length because of the transverse modes that can be supported. The fundamental mode, without any

transverse excitation, is the TEM_{00} mode and this mode typically has a Gaussian shape with a waist w which describes the extent from the axis where the intensity falls to $1/e$. The additional transverse modes are described by subscripts n and m which refer to either polar (Laguerre-Gaussian) or orthogonal components (Hermite-Gaussian). It is important to note that each mode will have a different decay rate which will impact the signal that is collected.

Spot Size The spot sizes of the TEM_{00} mode at the focal point and the mirror surfaces can be used to define the cavity (Berden and Engeln, 2009). The spot sizes for a mirror pair are:

$$w_{1,2} = \sqrt{\frac{L\lambda}{\pi}} \left[1 - \frac{g_{2,1}}{g_{1,2}(1 - g_1 g_2)} \right]^{0.25}, \tag{2.17}$$

and the beam waist spot size is:

$$w_0 = \sqrt{\frac{L\lambda}{\pi}} \left[1 - \frac{g_1 g_2 (1 - g_1 g_2)}{(g_1 + g_2 - 2 g_1 g_2)^2} \right]^{0.25}. \tag{2.18}$$

Mode Coupling Kogelnik (1964), Berden and Engeln (2009), and Siegman (1986) describe methods for mode coupling of lasers to an optical cavity. A ringdown cavity has inherent properties which should be matched by the incoming laser radiation in order to most effectively couple them. Either the laser radiation, the cavity, or both together can be modified in order to achieve the highest coupling efficiency. In most cases, the TEM_{00} mode is excited by matching the waist size of the beam and the cavity, as well as matching the beam front radius of curvature, by using lenses located in front of the first CRD mirror.

The beam front radius of curvature r_c, and the complex beam parameter q, can be used to define the Gaussian beam (Berden and Engeln, 2009).

$$\frac{1}{q} = \frac{1}{r_c} - i \left(\frac{\lambda}{\pi w^2} \right). \tag{2.19}$$

At the focal point of the cavity the beam will be flat, so $r_c = \infty$. The same condition applies for a properly collimated laser beam. From this we know that

$$q_i = i(\pi {w_i}^2 / \lambda) \tag{2.20}$$

and

$$q_0 = i(\pi {w_0}^2/\lambda) \tag{2.21}$$

so we can use ray transfer matrices to determine the focal length and separation distance of lenses to use for best mode coupling.

Ray Transfer Matrix For simplicity in analyzing an optical system, the paraxial approximation is used ($\sin\theta \approx \theta, \cos\theta \approx 1$, and $\tan\theta \approx \theta$). The system transfer matrix for the CRDS cavity of the photolysis cell (see Section 3.2) consists of the ABCD matrices of each optical component in the system. For translation, the matrix is:

$$\begin{bmatrix} 1 & d \\ 0 & 1 \end{bmatrix}$$

For the lens effect of a mirror:

$$\begin{bmatrix} 1 & 0 \\ \frac{2}{RoC} & 1 \end{bmatrix}$$

For the effect through a lens:

$$\begin{bmatrix} 1 & 0 \\ -\frac{1}{f} & 1 \end{bmatrix}$$

In a CRDS system, working back from the beam waist in the center of the cavity; $d_1 = L/2$, d_2 is the distance between the second lens and the mirror, d_3 is the distance between mirrors, and $f_{1,2}$ are the focal lengths of the first and second lenses as viewed by the propagating beam. So the system ABCD matrix is:

$$S_{CRDS} = \begin{bmatrix} 1 & d_1 \\ 0 & 1 \end{bmatrix} \begin{bmatrix} 1 & 0 \\ \frac{2}{RoC} & 1 \end{bmatrix} \begin{bmatrix} 1 & d_2 \\ 0 & 1 \end{bmatrix} \begin{bmatrix} 1 & 0 \\ -1/f_2 & 1 \end{bmatrix} \begin{bmatrix} 1 & d_3 \\ 0 & 1 \end{bmatrix} \begin{bmatrix} 1 & 0 \\ -1/f_1 & 1 \end{bmatrix}$$

In Gaussian beam propagation, q_i is related to q_0 by;

$$q_i = \frac{Aq_0 + B}{Cq_0 + D} \tag{2.22}$$

which can be solved for f_1, f_2, d_2, and d_3.

2.2.5 cw-CRDS

Conceived by Lehmann in 1994, Lehmann and Romanini performed early development and application of cw-CRDS (Romanini et al., 1997a,b) as a spectroscopy tool by rapidly cutting off the laser with an acousto-optic modulator (AOM), and they continue to develop and apply it (Huang and Lehmann, 2008). Lehmann and Romanini's former students have continued applying cw-CRDS to radical measurement (e.g.Kassi and Campargue (2012)). At nearly the same time, (Engeln et al., 1997) also developed the technique by using either accidental coincidence of the frequency of the laser and the cavity, or by locking the laser to the cavity. The group of Fittschen has, since 2006, been using cw-CRDS to measure many peroxy radicals in atmospheric oxidation chemistry (Thiébaud and Fittschen, 2006; Thiebaud et al., 2007; Fittschen, 2012; Ibrahim et al., 2007; Faragó et al., 2015), mostly focusing on HO_2 and alkyl peroxy radicals (RO_2).

In pulsed laser CRDS, the broad linewidth of the short pulse laser source is usually wider than the mode spacing (FSR) in the cavity. Because overlap with one or more resonant modes is virtually assured in a properly constructed cavity, ringdown within the cavity after a laser pulse is also virtually assured. In continuous wave CRDS, the linewidth of the laser is less than the FSR of the cavity, so the laser is likely to be between cavity modes of a stable ringdown cavity. In order for ringdown to occur in these cavities, the signal must first build up. This build up occurs when the laser is on resonance with a cavity mode.

Resonance and signal buildup in cw-CRDS cavity can be achieved by scanning the wavelength of the laser over the FSR of a stable optical cavity, scanning the length of the optical cavity while the laser wavelength is set, or mode locking the cavity and laser wavelength together. The most common cw-CRDS method today is to use a tubular piezoelectric actuator (TPA) mounted to one of the cavity mirrors to change length of the cavity. The TPA is driven by a triangle wave signal with sufficient intensity to change the length of the cavity slightly more than one free spectral range which causes resonance to occur and constructive interference to happen twice per period.

One challenge with cw-CRDS is that there is not a convenient 'trigger' event for ringdown. For this reason, an external circuit is needed to monitor the intensity in the cavity and rapidly cut off

the incoming laser. Often an acousto-optic modulator (AOM) is used for this purpose. It functions by diverting the beam path through a Bragg crystal when an acoustic signal is applied by a pressure transducer.

The scanning rate of the triangular wave voltage supplied TPA to modify cavity length should be slow enough that the signal is allowed to build and decay while on resonance. A scanning rate that is too rapid will cause a Doppler shift and change the rate of rise and fall of the signal within the cavity near resonance and make curve fitting more difficult.

2.3 Sensitivity Enhancement of MOR

Magneto-optic rotation was shown to be selective to only paramagnetic species, but its sensitivity was not much better than direct absorption (DA). Methods have been used to enhance the sensitivity of MOR. Frequency modulation (FM) has been used by McCarthy et al. (1994). Ju et al., has used Faraday Rotation Spectroscopy (FRS) to modulate both the magnetic field (Brumfield et al., 2013) and the laser wavelength (Brumfield et al., 2014) to increase sensitivity as well as a Herriott cell to increase the interaction path length (Ju et al., 2016).

2.4 Pulsed CEMOR

The CEMOR spectroscopy method has been described in detail by (Lane, 2012). Cavity enhanced magneto-optic rotation (CEMOR) is an absorption spectroscopy diagnostic technique based on a combination of two established spectroscopy methods; cavity ringdown spectroscopy (CRDS), which is highly sensitive, and magneto-optic rotation (MOR), which is highly selective.

When linearly polarized light is injected into a ringdown cavity containing a paramagnetic species of interest, placed in a suitable magnetic field, the plane of polarization rotates. A suitable detector placed after the output polarizer collects a rotational signal that builds with time. For all other parameters held constant, the rate of rotational buildup increases at higher concentration of the paramagnetic species. This ‘ringup time’ has been shown to have a power series relationship with the concentration of OH in a slot burner flame (Lane, 2012).

2.5 cw-CEMOR

Soon after continuous wave lasers began to be used for CRDS, this method was applied to sensitivity enhancement of MOR. Berden et al. (1998) have applied cw-CRDS to measurement of O_2 in fields up to 20 T. This method is similar to cw-CEMOR developed in our lab (see 4), with the main difference being that they mode locked the cavity rather than using an AOM to shut off the laser signal. They found that the reflections in a ringdown cavity have little, if any, effect on the polarization state of the incoming light. They measured the rate of optical rotation due to magnetically induced birefringence and dichroic effects.

When using continuous wave laser source with CEMOR, it is expected that the rotational signal will build with each pass to a maximum at the threshold point. The rate of ring-up will depend on the strength of rotation. The rate of ring-up and ringdown of the signal are the important data for analysis.

2.6 Oxidation Chemistry

The oxidation chemistry of a fuel contributes fundamentally to the combustion process because it determines the end products of combustion and the heat released along the way. Especially in the ignition phase, measuring and controlling the chemistry can have large effects on the overall reaction. The overall reaction is made up of a large number of elementary reactions which depend on temperature, pressure, and local equivalence ratios to determine reaction pathways. When the pressure and temperature in a combustion system are functions of time, such as in internal combustion (IC) engines, the ignition and oxidation becomes complex.

2.6.1 Peroxy Radical Chemistry

Reaction intermediates, specifically small peroxy radicals made up of C, H, and O, control the oxidation chemical kinetics. For most fuels (carbon chain greater than three) there are three temperature ranges that show different oxidation chemical kinetics. Low temperature combustion (LTC) has been defined as less than $\sim$900 K (Zádor et al., 2011), with high temperature being anything above that. At the upper end of the LTC temperature region there exists an intermediate

region (∼650 K-900 K) where chain branching and chain terminating reactions compete for the radicals. In the LTC region the alkyl peroxy radical (RO_2) controls oxidation. In the intermediate temperature region, oxidation proceeds through the hydroperoxy radical (HO_2) and hydroxyl radical (OH). At high temperature, oxygen radical (O), hydrogen radical (H), and hydroxyl (OH) are most important. The interesting phenomena of two-stage ignition, cool flames, and Negative Temperature Coefficient (NTC) behavior can be explained by competition between reaction pathways for these radicals.

Many studies have focused on modeling low-temperature oxidation of the components of fossil fuels and of mixtures of several of them, which have been proposed as surrogates for current fuels, in modeling the complete fuels, and in creation of custom blended fuels for desired characteristics. There has been renewed interest in improving the understanding of low-temperature gas phase oxidation of the wide range of organic compounds that can be found in fuels and bio-fuels.

Peroxy Radical Measurements

Peroxy radical measurements have been made by various means in the past. Most commonly, indirect measurements have been used such as titration and measurement of products. Because of the complex chemical kinetics occurring in combustion systems, indirect methods like measuring [OH] (or other products) and inferring [HO_2] cannot be used. In atmospheric chemistry, Chemical Amplification has been used to measure NO_2 as a product of HO_2 reactions with mixtures of high concentrations of NO and CO. A method that increases the sensitivity of chemical amplification with a cavity attenuated phase shift (CAPS) has been demonstrated by Wood and Charest (2014).

Various direct measurement methods have been used to measure HO_2 in "clean" reactors and in atmospheric pressure flames with limited success. Wavelength modulation spectroscopy (Taatjes and Oh, 1997), frequency modulation (Johnson et al., 1991), and cw-CRDS (Thiébaud and Fittschen, 2006) have applied continuous wave lasers to measure HO_2 in a photolysis cell similar to ours.

The Hanson group at Stanford has used the broad and structureless UV band near 227 nm to monitor the relative shape of the time history of HO_2 in a shock tube (Hong et al., 2013), but the lack of high fidelity UV absorption-cross section data does not allow absolute concentration

measurements.

Ethyl peroxy $C_2H_5O_2$ and methyl peroxy (CH_3O_2) have been measured in their near IR $\tilde{A} - \tilde{X}$ transition at 1.3 μm by Faragó et al. (2015).

Faraday rotation spectroscopy (FRS) has recently been used to measure HO_2 near 1396.9 cm^{-1} (7159 nm) by Brumfield et al. (2013) at atmospheric pressure at the exit of a flow reactor of DME and air, although this method requires comparison to the HITRAN database.

Quantitative measurements of HO_2 have been performed in a jet stirred reactor (JSR) with cw-CRDS with selected fuels: methane (Bahrini et al., 2012), butane (Djehiche et al., 2014), and dimethyl ether (DME) (Le Tan et al., 2015).

With the goal of application of CEMOR to measurements of HO_2, CEMOR was recently demonstrated by Lane (2012) to measure [OH] in a lean methane-air flame. His research concluded that the present CEMOR setup was not able to be used for measurement of HO_2 in our flash photolysis cell (FPC).

2.6.2 Flash Photolysis Cell

The use of laser photolysis to initiate chemical reactions has become common. The basic concept is that sufficient radiation energy is applied to dissociate a reactive species which then initiates chain reactions.

HO_2 Generation Chemistry As described by Lane et al. (2013), an essential step towards making quantitative measurements of HO_2 and RO_2 in a combustion environment is to first generate these species in a controlled environment. A flash photolysis technique has been employed to generate a "clean", room temperature source of HO_2 radicals (Taatjes and Oh, 1997; Thiebaud et al., 2007; Glover and Miller, 2005), which consists of dissociating chlorine molecules with 355 nm photons in the presence of methanol (CH_3OH), oxygen (O_2), and helium (He). Chlorine radicals (Cl) react with CH_3OH to produce HO_2 via the following effectively first-order reaction sequences:

$$\mathrm{Cl_2} \xrightarrow{\mathrm{hv}} 2\,\mathrm{Cl} \qquad \text{(R 2.1)}$$

$$Cl + CH_3OH \longrightarrow CH_2OH + HCl \quad \text{(R 2.2)}$$

$$CH_2OH + O_2 \longrightarrow HO_2 + CH_2O \quad \text{(R 2.3)}$$

The reaction rate coefficients for reactions (R 2.1) and (R 2.2) are 5.7 x 10^{-11} and 9.1 x 10^{-12} cm^3 $molecule^{-1}$ s^{-1}, respectively (Atkinson et al., 1997). Methanol is in excess of the Cl radical so that HO_2 is produced in a 1:1 ratio with Cl radicals. HO_2 depletion takes place through the well-known self-reaction pathway producing hydrogen peroxide and oxygen (R 2.4).

$$HO_2 + HO_2 \longrightarrow H_2O_2 + O_2 \quad \text{(R 2.4)}$$

The second-order reaction rate coefficient for R 2.4 has been measured to be 2.1 x 10^{-12} cm^3 $molecule^{-1}$ s^{-1} (Taatjes and Oh, 1997).

RO_2 Generation Chemistry A similar method can be used to generate C_3 peroxy radicals, where propane replaces methanol in the photolysis cell (Zalyubovsky et al., 2005; Melnik et al., 2010).

Following reaction R 2.1:

$$C_3H_8 + Cl \longrightarrow C_3H_7 + HCl \quad \text{(R 2.5)}$$

$$C_3H_7 + O_2 \longrightarrow C_3H_7O_2 \quad \text{(R 2.6)}$$

Both the normal and isomer propyl peroxy (n-$C_3H_7O_2$ and i-$C_3H_7O_2$) radicals are produced with this method.

Photo-dissociation of Cl_2 produces Cl at a near 1:1 conversion efficiency of 355 nm photons from the Nd:YAG pulsed laser. At a known output energy of the dissociation laser, a known quantity of Cl is produced. Because methanol is in excess, reactions R 2.2 and R 2.3 proceed to produce HO_2 at 1:1 with Cl. Therefore, a known 355 nm energy input produces a known concentration of HO_2 within the reactor for measurement. The energy of the 355 nm pulse can be controlled by varying the timing delay between the amplifier flash lamp and laser q-switch pulses in the dissociation laser (Continuum Precision 8000). The maximum energy per pulse occurs when the timing is set at 290 μs, and decreases with longer delay.

The timing between the photolysis pulse and the cw-CRDS ringdown event is not directly controlled, so absolute [HO_2] is measured by the cw-CRDS event and calibrated against the expected concentration based on the modeling results.

3. Experimental Facilities and Procedures

Several facilities were used for laser spectroscopy experiments in the laser lab. During the course of these experiments, the laser laboratory was shutdown, placed in storage, and moved across campus which prompted modifications and upgrades to the facilities which may not have otherwise been performed. While the disruption delayed the present research, it did not otherwise impact the objectives and accomplishments.

A slot burner facility was used for measurements of OH in a lean methane air flame using MOR, CRDS, and CEMOR. This facility was used for preliminary observations of the effect of magnetic field strength on MOR signal. Modifications to the slot burner were tested for stabilization of a lifted flame for use in laser diagnostics of the preflame region of C3 and higher alkanes for cool flame behavior. A flash photolysis facility was used to generate and measure HO_2 for CEMOR development.

3.1 Slot Burner

The CEMOR method was successfully applied to measurement of [OH] in a methane-air slot burner (see Figure 3.1). In these experiments the probe laser propagates through the mode coupling optics, through an initial polarizer and half wave plate to control the light intensity and a second polarizer. The laser beam then propagates into the cavity through the backside of the first mirror and reflects back and forth between the two cavity mirrors. The separation of the mirrors is adjusted to ensure the TEM_{00} mode within the cavity. The interaction of the magnetic field produced by the two neodymium magnets and the paramagnetic species in the flame causes increased rotation in the polarization plane with each trip through the cavity. A small portion of the laser exits the second mirror, through the analyzing polarizer to the detector. The signal is collected by oscilloscope and transferred to the computer for recording and analysis.

In these experiments, the 0.6 T permanent magnets are held at a separation distance of 8.8 cm which provides a nearly homogeneous magnetic flux density of approximately 0.12 T along the full flame width.

For the quantitative CRDS measurements the experimental setup was the same except we removed the polarizers and the magnets.

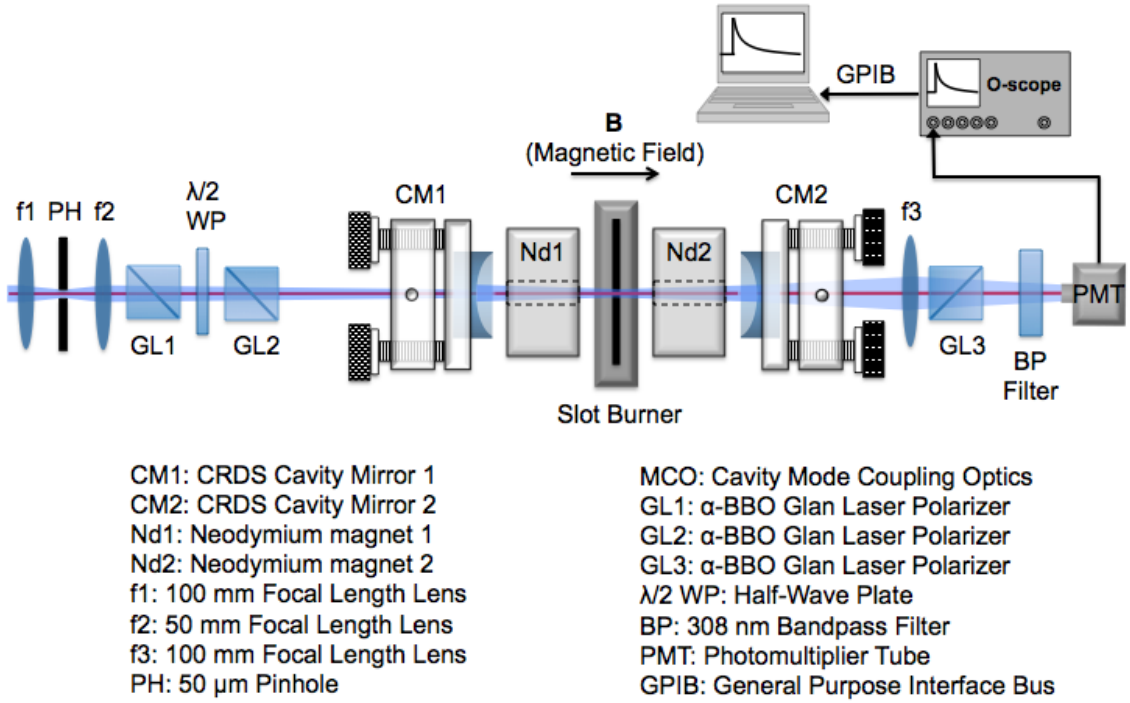

Figure 3.1: CEMOR diagnostic applied to measurement in a methane-air slot burner flame (Lane, 2012)

The experimental system for MOR is illustrated in Figure 3.1 and has been described in detail elsewhere (Emig et al., 2002a; Lane, 2012), so only a brief description will be provided here. The necessary laser light was generated using an optical parametric oscillator (OPO) (Continuum Sunlite EX) which was pumped by the third harmonic output of a 10 Hz Nd:YAG laser (Continuum Precision 9010). The OPO generates plane-polarized light that has a manufacturer's quoted 0.075 cm^{-1} linewidth and is 90% horizontally polarized. The output of the OPO laser was sent through doubling crystals (Continuum FX-1) and then directed to the MOR experimental setup. A HeNe laser beam was used for cavity alignment by making it collinear with the pulsed laser. Its

633 nm visible beam significantly increased the ease and safety of alignment over the uv beam of the Nd:YAG laser. A 0.52 equivalence ratio Φ methane-air flame was stabilized on a Perkin-Elmer (AAnalyst) slot burner placed in the absorption path of the laser so that the laser crossed the thin width of the flame. The burner was attached to a linear stepper motor to precisely control the height in the flame. Two ring permanent magnets (K&J Magnetics, RY04Y0) that generate a magnetic flux density (**B**) of approximately 0.12 Tesla, nearly constant over the flame width, were placed coaxially with the laser beam and equally spaced from the burner. The experiments were conducted in the Faraday configuration, where the laser beam propagates parallel to the magnetic field; the magnetic field lines were axisymmetric about the laser beam. The output polarizer (GL2) was set 90° relative to the input polarizer (GL1). The laser was then scanned over the $Q_1(1)$ transition line at $\sim$ 308 nm (32474 cm^{-1}), and the transmitted signal intensity was detected using a PMT (Hamamatsu R562) connected to an oscilloscope (50 Ω termination). The signal from the PMT was averaged 50 times at each step in the wavelength scan (0.002 nm between steps) and transmitted to a custom LabVIEW program for analysis and data collection. The collected data were fit to Gaussian profiles.

3.2 Photolysis Experiments

The main goal of CEMOR is to make in situ sensitive and selective measurements of paramagnetic species in complex reacting environments where traditional methods have difficulty due to spectral congestion with stable species. Specifically, the peroxy radical species of interest have the strongest overlap with the main products of combustion, CO_2 and HO_2. In order to develop CEMOR for measurement of peroxy radicals, the next step was to generate HO_2 in an environment without other species which cloud the absorption spectrum.

A Flash Photolysis Cell (FPC) was developed by (Lane et al., 2013) for study of known concentrations of peroxy radicals in a "clean" environment. This facility will allow measurement by CRDS, cw-CRDS, and CEMOR diagnostic methods. The CRDS methods can generate data used to calibrate CEMOR for quantitative measurement. The Fittschen group (Thiébaud and Fittschen, 2006), the Miller group (Chhantyal-Pun et al., 2010), Zalyubovsky et al. (2001), and Melnik et al. (2010) have all used versions of low pressure photolysis facilities in their study of peroxy radicals.

The FPC facility has been used with CRDS to make measurements of HO_2 (see Figure 3.2). The FPC cell is designed with overlapping photolysis and probe beams for increased absorption pathlength of the peroxy radicals generated. The endplates of the cell incorporate ringdown mirrors and an electromagnet coil has been inserted in the center of the cell to generate the required magnetic field for MOR and CEMOR measurements. The wetted portion is a 53.3 cm long by 7.6 cm PTFE chamber which is closed by a flange on each end. The flanges have angled photolysis windows next to the probe beam path providing an overlap of 17.2 cm between the 0.5 cm probe beam and the 1.6 cm photolysis beam. The probe beam is axisymmetric with the photolysis cell, passing through CRD mirrors which are mounted on extension arms which serve to extend the optical path length and provide a longer and larger volume for the shielding flow of helium in front of each mirror. Two 99.99% reflective, 25.4 mm diameter, 1 m RoC, CRD mirrors (CRD-Optics) form the ends of the 77.5 cm ringdown cavity. Each window and CRD mirror is sealed by an o-ring. The first mirror is held in place by a kinematic mirror mount. The second mirror is mounted to a tubular piezoelectric actuator (Physik Instrumente) by a PTFE adapter ring and held in place by a kinematic mirror mount (ThorLabs).

In these experiments Cl_2, O_2, and He gas flow rates are controlled via rotometers. A nebulizer delivers the methanol into heated tubing that carries a flow of helium, which is then directed into the mixing chamber with the other gases and are then passed into the reactor. The photolysis reaction produces corrosive gases (primarily HCl), so the majority of wetted surfaces within the photolysis cell are made from PTFE for resistance to corrosion. The HCl and remaining Cl_2 are passed into a scrubbing system which is constructed of two washing bottles containing sodium hydroxide (NaOH) and a cold trap to neutralize and separate the corrosive gases before the vacuum system.

In the initial measurements of HO_2, a pulsed Nd:YAG laser (the same used in slot burner experiments) was used as the probe beam. Laser timing is by externally triggering both Nd:YAG lasers via TTL signals from function generators. Delay between Flash Lamp and Q-Switch triggers is 290 μs for maximum power for both YAG lasers. This is more power than necessary for the photolysis laser, so the delay is increased to reduce the photolysis laser output to 70 mJ. Once the trigger pairs are set for desired output, the delay between lasers can be adjusted to collect data at different concentrations of HO_2 (see Figure 3.3).

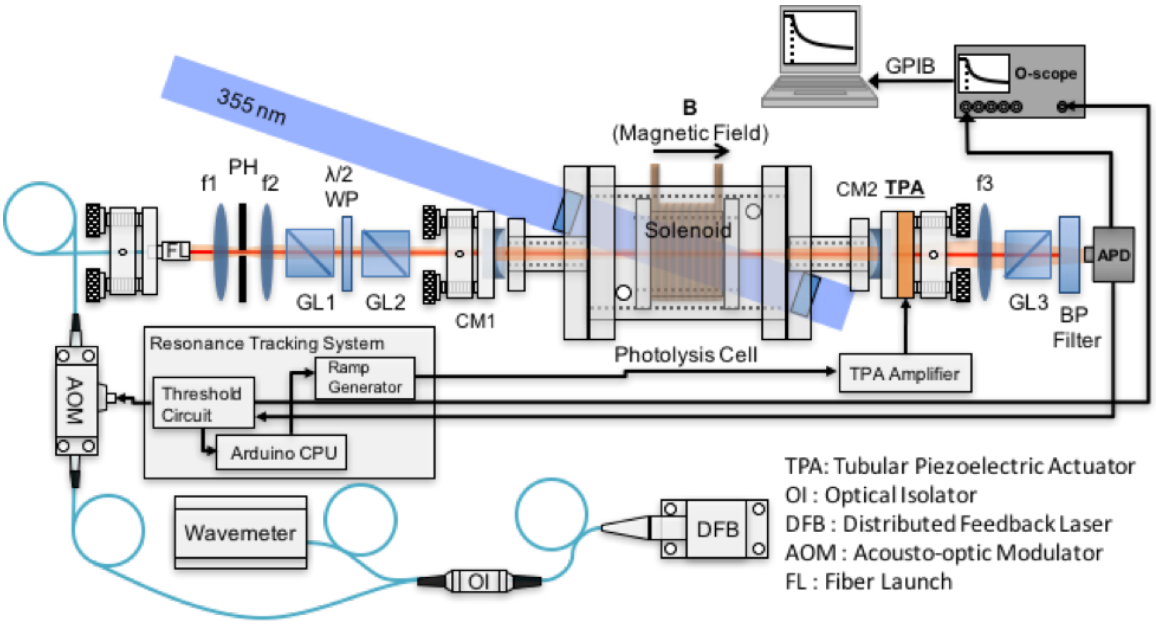

Figure 3.2: Flash Photolysis Cell with cw-CEMOR system. The cw-CRDS system is similar except the polarizers and $\lambda/2$ waveplate are removed, and the electromagnet coil is not activated.(Based on design by Lane (2012))

An important part of the design of the photolysis facility was the construction of a stable optical resonator for the CRDS and CEMOR diagnostics. The probe beam is coupled to the TEM_{00} mode of the optical cavity via mode coupling optics (f_1 and f_2). The relative positions of f_1 and f_2 with the optical cavity are calculated via a ray transfer matrix approach discussed in Section 2.2.4.

The spectral region of interest for measurement of HO_2 is the low lying electronic band ($A^2A' \leftarrow X^2A''$) near 1430 nm (7000 cm^{-1}). This band in the IR region was selected because the more typically used UV band, although having stronger absorption, is broad and structureless making identification and quantification more difficult, and the mid-IR bands are more strongly effected by pressure broadening.

3.3 cw-CRDS experimental setup

The free spectral range of the ringdown cavity in the FPC is: 1.31 pm, where L is 77.5 cm and the vacuum wavelength, λ, is 1.428 μm. The laser diode (LD) employed in these experiments was a NEL NLK1E5EAAA single mode, 14-pin butterfly package with thermoelectric cooler. The

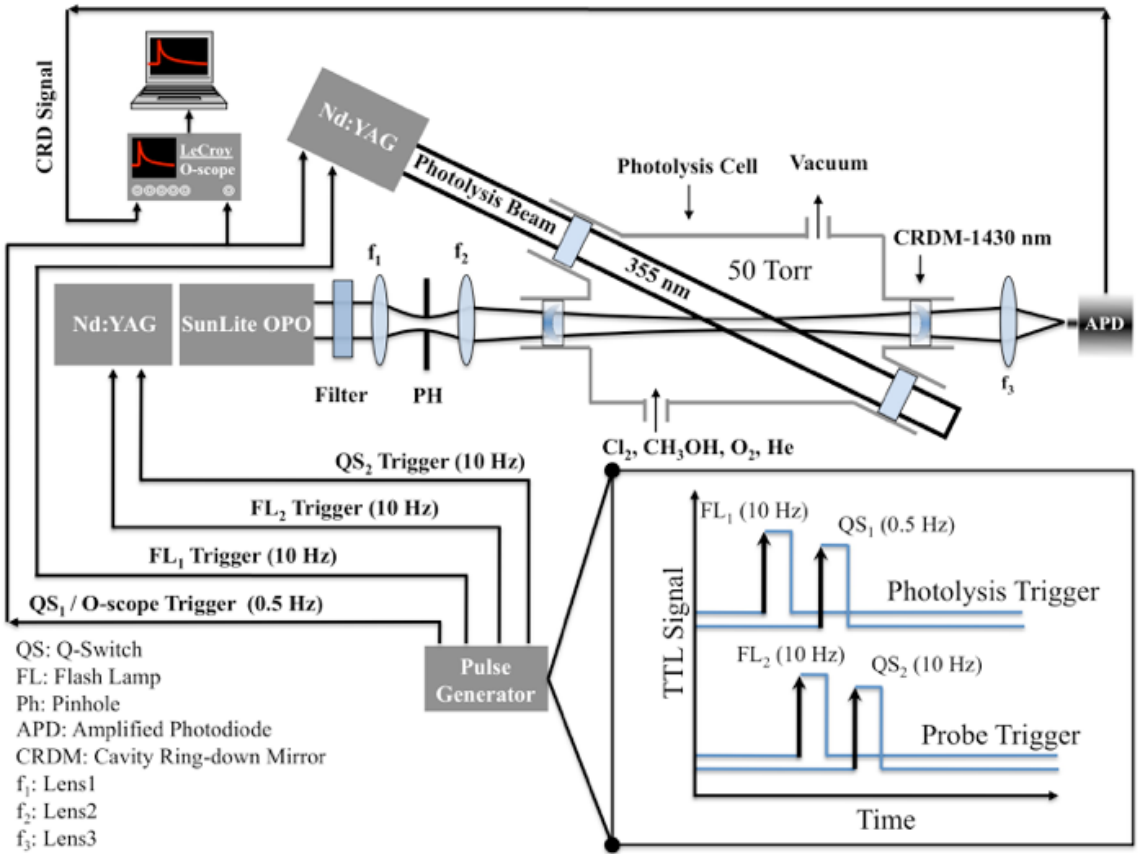

Figure 3.3: Pulsed CRDS experimental setup and timing scheme for measurement of HO_2 (Lane, 2012)

LD chip is coupled with a panda style polarization maintaining fiber and ended with an FC/APC[1] connector. The output is centered at 1428.6 nm.A similar laser diode (NEL, NLK1S5EAAA) with output centered at 1504 nm is available for experiments probing the vibrational overtone band of O-H stretch near 1.504 μm.

The LD was mounted to a butterfly mount (Arroyo Instruments 203) and controlled by temperature (Peltier heater/cooler) and current stabilization with controllers (LaserSource 4201-DR 50 mA/100 mA, and TECSource 5240 4A/7V). The threshold current is typically 10 mW. The linewidth of the laser was certified at less than 2 MHz.

The experimental setup is shown in Fig 3.2 with components mounted to a vibration-isolation

[1]FC/APC stands for fixed connection with angled physical contact. These are used to prevent reflection back into the fiber and keyed to align polarization between connections

table (Newport RS-48-12), but thermal motion of the optical elements (including the ring-down cavity) was not addressed. The output of the laser is connected to an optical isolator (OI) with tap coupler (Fiberon F4M-PMTI-1-43-10-D-9L-25-1) where 90 % goes to an Acousto-Optic Modulator (AOM) (AA Opto-Electronic MT80-IIR30-Fio-PM0,5-J1-A-VSF, driven by MODA80-D41k51k-344575) and 10 % by fiber to a wavelength meter (Bristol Instruments 821B-NIR) with an accuracy of ±0.02 cm^{-1}. The AOM is PM fiber coupled to the OI. The AOM is driven by an 80 MHz driver. This designation indicates that an 80 Mhz acoustic wave is generated across an optical crystal by a piezo-electric transducer to create multiple orders of light beams at different directions through the crystal. In this experimental setup, the 0th order beam is blocked inside the AOM and the 1st order beam is allowed to pass to the PM fibered output when activated by the driver. As a consequence of the 80 MHz driven frequency of the AOM, the 1st order beam has an +80 MHz shift in frequency from the input, where at 7000 cm^{-1} the shift is $\sim$0.0027 cm^{-1} which is a known quantity that can be considered as an offset when necessary, and lies within the accuracy range of the wavemeter. The first order output passes through optional beam shaping optics (a pair of anamorphic prisms and mode-coupling lenses) before entering the Fabry-Perot resonator. The ringdown cavity is 77.5 cm in length where two 1 in. (25 mm) mirrors (CRD Optics, 901-0010-1400) with 1 m radius of curvature (RoC) form the ends of the FPC. The mirrors are located in kinematic mirror mounts (Thorlabs KC-1) for cavity adjustment.

Cavity output detection is performed by an InGaAs avalanche photodetector (Thorlabs APD110C) digitized to an oscilloscope with 50 Ω termination. The ringdown signal is fitted using a Levenberg-Marquardt algorithm in a custom LabVIEW program.

The pressure in the FPC is monitored with a capacitance monometer pressure transducer (Setra 730). Before introducing any samples for measurement, the FPC is evacuated to 100 Torr using a mechanical pump. Background scans are also performed at this pressure. A constant pressure is maintained within the FPC by controlling the inflow rate of gases and the evacuation rate. For atmospheric pressure water vapor measurement, the FPC was valved open to air.

Resonance within the continuous wave cavity ringdown system is controlled by the resonance tracking system (RTS). An Arduino microcontroller monitors the signal intensity exiting the ring-down cavity by measuring the avalanche photodetector, controls the rear mirror scanning, and

rapidly switches off the laser. When the signal is above a threshold value the RTS system triggers the acousto-optic modulator to rapidly block the laser from entering the cavity.

The control circuit is based on a design published by Votava et al. (2012). The design was customized for our system in order to provide faster operation and a longer period of laser shut off which allows longer ringup and ringdown times to be measured.

3.4 Cool Flame Facilities

3.4.1 Stabilized cool flame reactor

Application of the CEMOR diagnostic to HO_2 in combustion environments is a major goal. HO_2 is most important in cool flame reaction conditions, so cool flame conditions need to be established. A stabilized cool flame reactor (SCFR) (Figure 3.4) was constructed for the lab and evaluated by Lane et al. (2009), so only a brief description is given here.

The SCFR is a facility designed for laser diagnostics of cool flame and first stage ignition conditions. The observation chamber is a custom made quartz piece with four 1 cm laser ports located 40 mm above the burner. The quartz reactor is 190 mm tall in a vertical, co-annular configuration on a stainless steel mixing and gas supply system. The premixed flame burner is surrounded by a flow of N_2 between the walls of the double wall quartz chamber. There is a mixing chamber for premixing the fuel and air and immediately downstream, a stainless steel bead bed which ensures a homogeneous mixture and acts as a heat sink to eliminate flashback. The reacting gases are preheated by four honeycomb ceramic heaters and flow through a laminar flow element before reaching the 6 cm inner quartz tube.

Nitrogen is used to maintain temperature in the inner burner chamber. The flow is preheated by a 3 kW heater before entrance to the reactor. The heated N_2 is then passed through a laminar flow element before entering the 9 cm ID outer quartz tube. Temperatures of all of the incoming gases are monitored by thermocouples and controlled in six zones. Gas flows are controlled by mass flow controllers which can be set from a custom LabVIEW program.

(Ballinger and Ryason, 1971) have demonstrated stable cool flames by using a similar type of reactor with an annular channel of nitrogen as a shroud gas.

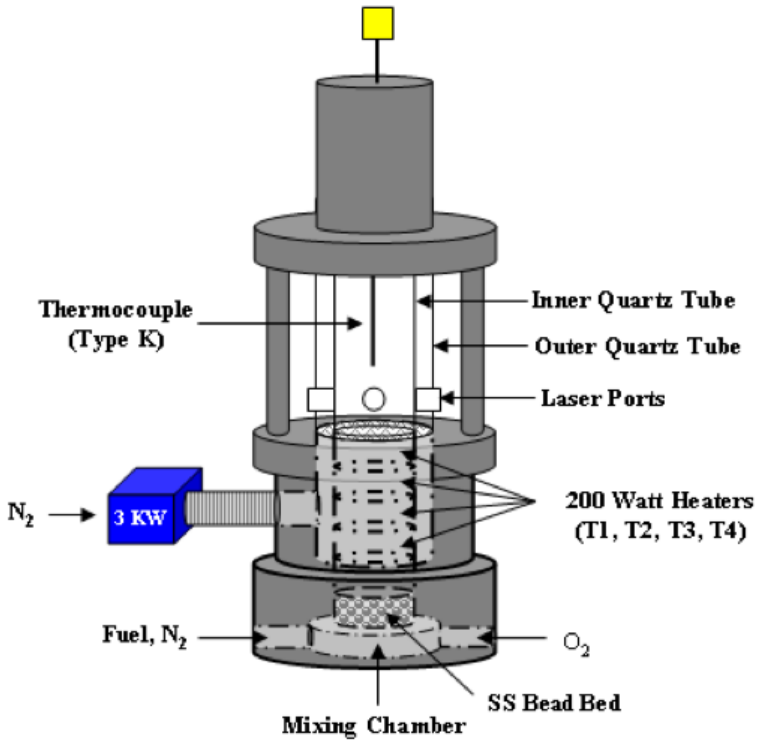

Figure 3.4: Stabilized cool flame reactor facility (Lane, 2012)

3.4.2 Lifted flame burner

Investigations were performed to determine whether a lifted flame can be stabilized above the slot burner used in MOR, CRDS, CEMOR experiments (Section 6.1). This facility lacks the sophistication of the SCFR, yet has demonstrated that a portion of the flame can be stabilized lifted from the burner head. The lifted laminar premixed flame is susceptible to convective currents in the room because it relies on heat transfer to maintain stability. Gas flow rate also needs to be finely controlled in order to maintain stable conditions.

A mesh screen, placed above the slot burner, stabilizes a flame below or above the mesh. Flames stabilize below the mesh at higher velocities than without the mesh. The most promising orientation is with the mesh at an angle to the slot burner surface. In this method, the premixed flow jet can lift the flame at a location close to the burner surface. The flame is attached to the mesh at a location further from the burner surface and sufficient heat and chemistry from the attached portion of the flame stabilizes the lifted flame.

3.5 Closure

Several experimental facilities were employed in this study. The slot burner and FPC setups were reused from Lane (2012). The cw-CRDS facility is similar to the systems that others have used in literature. The cw-CEMOR facility is an adaptation of our previously used CEMOR facility and the new to us cw-CRDS facility with some upgrades. The cw-CRDS/CEMOR experimental facility is a new design which has not yet been proven.

The laboratory move offered opportunities and challenges in setting up experimental equipment and facilities. Some components were lost in the move and some others were damaged. The new lab layout required reorienting the slot burner CEMOR setup.

4. Cavity Enhanced Magneto-Optic Rotation Development

4.1 Introduction

As stated previously, the development of CEMOR as a sensitive and selective laser diagnostic started with application of MOR to selective detection of paramagnetic species mixed with non-paramagnetic laser dye (Emig et al., 2002b). In the next step, they measured Ga in an acetylene/air flame. Using atomic absorption they had a detection limit of 70 ppm and with MOR they could detect down to 60 ppm. By applying CEMOR in a Voigt configuration to the same setup, they were able to achieve 200 ppb sensitivity, a significant improvement.

Lane et al. (2011), analyzed the results presented in Emig et al. (2002b) to evaluate the spectroscopic fundamentals which allow MOR to selectively measure Ga atoms. The next major step was application of MOR, CRDS, and CEMOR to measurement of OH radical in a methane-air flame (Lane, 2012). The sensitivity limit of OH using MOR was determined to be 2.5 x 10^{12} cm^{-3} for the ground level population of the $Q_1 1$ line. CRDS demonstrated a sensitivity of 3.8 x 10^{11} cm^{-3}, and CEMOR demonstrated an improvement over MOR by a factor of 10.

Although much progress has been made in development and application of CRDS and CEMOR to concentration measurements of paramagnetic species, some work is yet to be done in the development of the continuous wave (cw) version of CRDS and CEMOR.

Further characterization of the CEMOR signal is necessary. This will require characterizing the effect of magnetic field strength on the CEMOR signal. An experimental test fixture has been designed to vary the separation distance of two 50 mm OD neodymium magnets (the same magnets which were used in the previous CEMOR [OH] measurements by Lane (2012)). The strength of the magnetic field exponentially decays with increased separation distance between them. It is expected that a weaker magnetic field measuring the same concentration will change the signal by reducing the rotational buildup, thereby extending the ring-up time and changing the shape of the signal generated.

Previous results have demonstrated a power series relationship of CEMOR ring-up time with

concentration of OH in a methane-air slot burner. The results of the magnetic field strength characterization work described here are integral to understanding the underlying physics of CEMOR spectroscopy.

4.2 Research Objectives

The literature review identified remaining needs in measurement of small peroxy radicals in combustion chemistry and limitations of spectroscopic methods which have been applied to measurement of these so far. The specific goals that were set out to be addressed by this research are listed below:

4.2.1 Apply CEMOR to radical measurement in Flash Photolysis Cell

The main goal of this work is to make measurements of HO_2 concentrations generated in the Flash Photolysis Cell (FPC). The FPC has been developed and used with an in-house Nd:YAG/OPO laser system to generate HO_2 and measure HO_2 and H_2O. Several upgrades were made to this CEMOR spectroscopy system in order to make the necessary measurements.

Develop and apply continuous wave laser CEMOR (cw-CEMOR)

Previous CEMOR development has been accomplished exclusively with pulsed Nd:YAG/OPO laser. Although application of CEMOR with a pulsed laser requires a simpler setup than with a continuous wave laser, the pulsed laser is more difficult to operate and the laser linewidth is insufficiently narrow to make measurements of the spectral features of HO_2. The development and application of a continuous wave version (with higher resolution) of CEMOR is covered in this task.

Design and build cw-CRDS/cw-CEMOR spectroscopic facility The cw-CRDS facility is inspired by setups used by other researchers, i.e. Romanini, Fittschen, and Atkinson (Macko et al., 2004; Morville et al., 2004; Thiébaud and Fittschen, 2006; Thiebaud et al., 2007; Atkinson, 2001; Atkinson and Spillman, 2002). These other groups have made hydroperoxy and alkylperoxy measurements in a "clean" environment as well. See Figure 4.1 for an example cw-CRDS setup.

The main difference between pulsed and continuous wave laser CRDS is the laser source (i.e. solid state (Nd:YAG) vs. semiconductor diode laser). The step to incorporate a narrow linewidth laser is not as simple as changing the laser source, although the changes are expected to increase the stability and reliability of the system. This difference in the source of the laser significantly influences the necessary components used to achieve the ringdown effect. Two important differences are the need to quickly cut-off the laser source from the ringdown cavity, and the narrow linewidth of continuous wave lasers is not likely to always overlap a transverse mode in the ringdown cavity. Because of this, the length of the cavity needs to actively changed to cause overlap. When overlap occurs, the energy in the ringdown cavity builds and the laser needs to be rapidly cut off, and the ringdown time of the light exiting the cavity measured. A fast optical switch is needed to quickly cut-off the laser to the cavity.

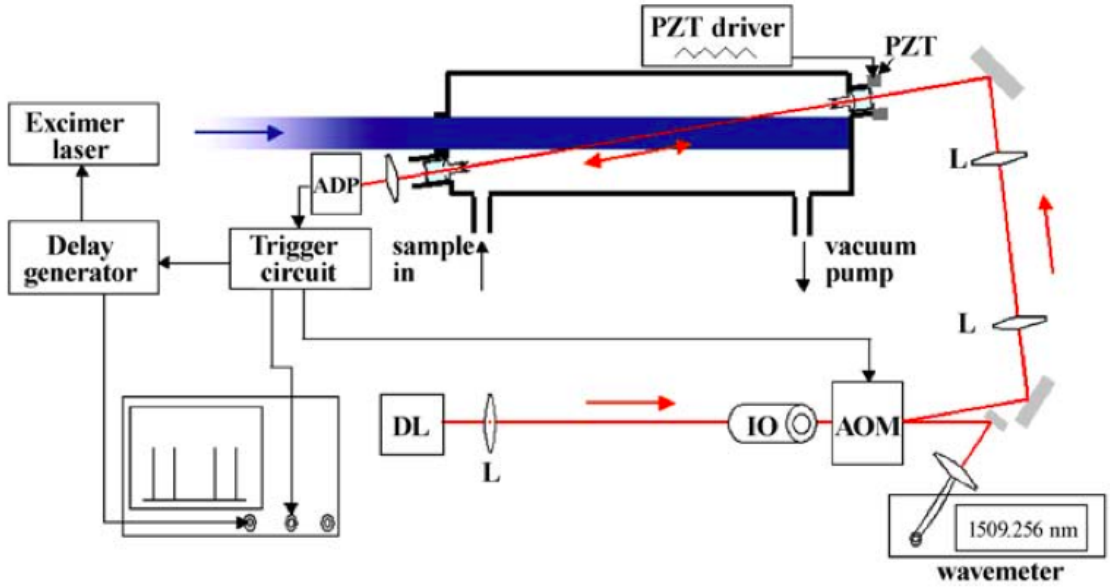

Figure 4.1: Schematic of cw-CRDS experimental set-up. DL: diode laser, OI: optical isolator, AOM: accousto optic modulator, PZT: piezoelectric transducer, APD: avalanche photodiode, L: lens (Thiébaud and Fittschen, 2006)

4.2.2 Apply cw-CRDS within flash photolysis facility and measure water line

The first measurement after setting up the cw-CRDS system will be to measure a water line near 7000 cm^{-1}in the atmosphere. Empirical data is available to compare to (Macko et al., 2004; Mikhailenko et al., 2014).

4.2.3 Characterize and calibrate the cw-CRDS system for HO_2 quantification

After successful measurement of atmospheric water vapor, the next step will be to generate HO_2 in the FPC and measure line position and absorption data of the electronic transition near 1.43 μm and compare to published values (Zahniser et al., 1989)

Once the cw-CRDS system has measured HO_2 in the photolysis cell, the next step is to generate calibration curves including effect of temperature.

4.2.4 Develop and apply stronger electromagnet for use in Flash Photolysis Cell experiments

In order to address the issue of magnetic field strength in the FPC, two tasks will need to be accomplished. Further characterization of the CEMOR signal in relation to magnetic field strength is needed as well as applying a stronger electromagnet to the FPC.

CEMOR: Magnetic Field Strength Characterization Characterization of the effect of magnetic field strength on CEMOR signal will aid in its application to measurement of radicals. This work will inform design decisions related to the source of the magnetic field in application of CEMOR to measurements of HO_2 in the FPC and SCFR.

The PhD Dissertation of Jamie Lane discusses the CEMOR signal, but lacks detail regarding the effect that the strength of the magnetic field has on the CEMOR signal. This task addresses that issue by performing pulsed MOR and CEMOR on OH in flame in a setup similar to that used by Lane (2012). The same permanent magnets will be used, but in movable jigs that precisely control the distance between the magnets which also precisely controls the magnetic flux density across the flame sheet.

Electromagnet As described earlier, the magnetic field strength in the FPC is too weak to cause sufficient Zeeman splitting to register a detectable signal. A method to increase the strength is needed, yet there are limitations with the present design. The electromagnetic coil has been designed to maximize the magnetic field strength within the internal dimensions of the FPC. Magnet wire of 22 AWG was wound on a spool inside the FPC.

An option to increase the strength of the magnetic field without changing the overlap of the lasers is to increase the electrical current supplied to the electromagnet coil. In order to avoid overtemp of the coil, water cooling can be added to dissipate the joule heating from the coil.

Another option to avoid an over-temperature situation with the electromagnet is to more closely control the timing of the high current pulses delivered to it by reducing the duration of the electromagnet's current pulse and the delay between the laser and current pulses.

4.2.5 Characterize the CEMOR technique in the photolysis cell as a function of HO_2 concentration

The first step is to measure CEMOR signal at various concentrations of HO_2 in a "clean" cell. Then controlled amounts of HO_2 can be seeded into the cell in order to measure the ability of CEMOR to select HO_2 over H_2O. It is expected that the increase in concentration of the diamagnetic absorber will reduce the peak intensity and suppress ringup time. Once this step is complete, increased temperature measurements should be applied. And the final step is to generate HO_2 calibration curves and compare to results in Objective 4.2.3.

4.3 cw-CEMOR Development

The incorporation of a continuous wave DFB laser as the light source in this experimental setup causes increased complexity to the spectroscopy system, although the stability and reliability of the system is expected to be an improvement. Although cw-CRDS has been in use for some time (Romanini et al., 1997a), the incorporation of cw-CRDS into CEMOR is novel and requires more specific and stringent capabilities in the selection of optical components in order to maintain the polarization of the diagnostic laser.

Two DFB lasers have been purchased which cover the spectral regions of interest, $A^2A'(000) \leftarrow X^2A''$ at 1.43 μm and the neighboring ν_1 vibrational overtone band at 1.5 μm, along with an amplified photodiode (APD) sensor for the same region.

A micro-controller based resonance tracking system has been designed and constructed to control the resonance, ring-up, and ring-down events within the cw-CRDS/cw-CEMOR system. It is inspired by a controller designed by Votava et al. (2012).

4.4 cw-CRDS/cw-CEMOR system development

The complete cw-CRDS/cw-CEMOR system design is described following. An overview diagram of the system is included as Figure 3.2.

Microprocessor based resonance tracking system

A microprocessor based resonance tracking system (RTS) was designed, constructed, and bench tested. The layout of the microcontroller is shown in Figure 4.2. A more complete description of the system is included in Section 4.4. The concept is based on a design published by Votava et al. (2012) and is expected to increase the data acquisition rate by rapidly reversing the tubular piezoelectric actuator (TPA) scan direction triggered by the occurrence of a ringdown event. This results in less travel of the TPA between scans while still changing the cavity length at an acceptable rate. Changing the cavity length too quickly during ringdown events causes the signal decay rate to appear faster due to part of the ringdown event occurring while off resonance, and resulting in over counting of the absorber molecule. The RTS is designed to have ringdown events occurring at 150-200 Hz.

In case of difficulty implementing the active control scheme described above, a passive control scheme can be used on the same hardware where the amplitude of modulation of the PZT is set to be slightly larger than the free spectral range (FSR) of the cavity in order to achieve resonance in the cavity at least twice per period.

The input to the microcontroller is the avalanche photodiode (PD) measuring signal escaping from the optical cavity, and the outputs are: Triangle wave to TPA, Signal to optical switch (AOM)

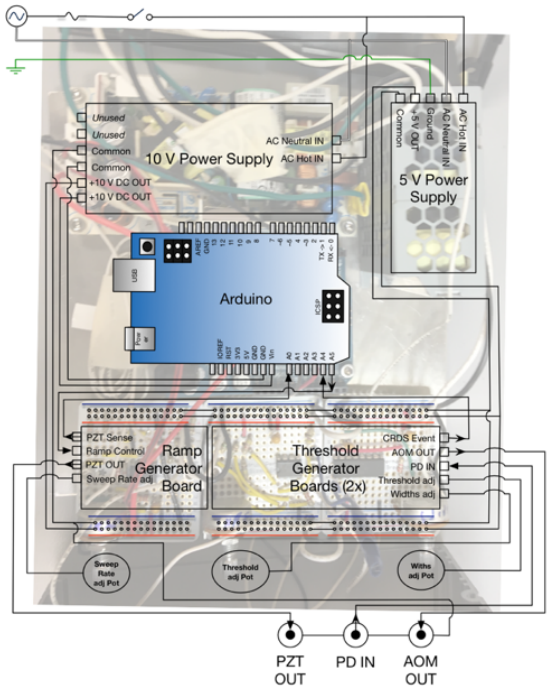

Figure 4.2: Microcontroller layout. The controller is built around an Arduino microcontroller (duemilinove) and uses potentiometers to control triangular wave ramp rate and frequency, as well as the width of the pulse for the optical switch.

driver, Trigger to DAQ.

Basic system description

The resonance control system is designed to control laboratory continuous wave cavity-ringdown spectroscopy (cw-CRDS) measurements. This system consists of a CRDS resonator, resonator photodiode (PD), piezoelectric element (PZT) to vary resonator length, fast optical switch, and a tracking unit. The tracking unit consists of the following subsystems; a microcontroller, ramp generator, threshold detector, and associated power supplies as described in “Microcontroller based resonance tracking unit for time resolved continuous wave cavity-ringdown spectroscopy measurements" by Votava et al. (2012). The RTS is advantageous because the cavity length is partially swept a distance of less than one wavelength, increasing data acquisition rates and temporal resolution.

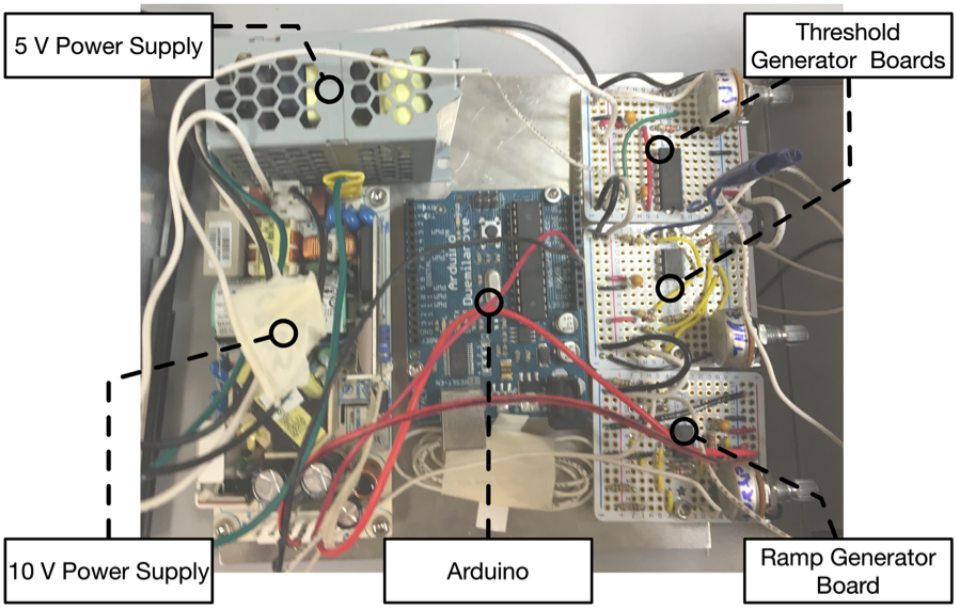

Figure 4.3: System overview of Resonance Tracking System

4.4.1 Rear Panel

The rear panel consists of an IEC C13 socket, 5 A busman type fuse, and power switch. See Figure 4.4

Figure 4.4: Rear Panel

4.4.2 Front Panel

The front panel consists of 3 labeled female BNC connectors and 3 labeled potentiometers for adjusting the Ramp Generator and Threshold Generator. The BNC connectors are grounded to the 10 V power bus on the prototype boards. See Figure 4.5

4.4.3 5 V Power Supply

The 5 V power supply is a 5 VDC 15 W Delta PMC-05V015W1AA panel mount power supply mounted on its side. The five labeled rear connections allow 120 V input and 5 V output. The Ramp Generator and Threshold Generator circuits require 5 VDC supply.

4.4.4 10 V Power Supply

The 10 V power supply is a NPS43-M 12V power supply with the voltage adjust potentiometer turned to minimum. The Ramp Generator and Arduino requires 10 VDC supply. See Figure 4.6

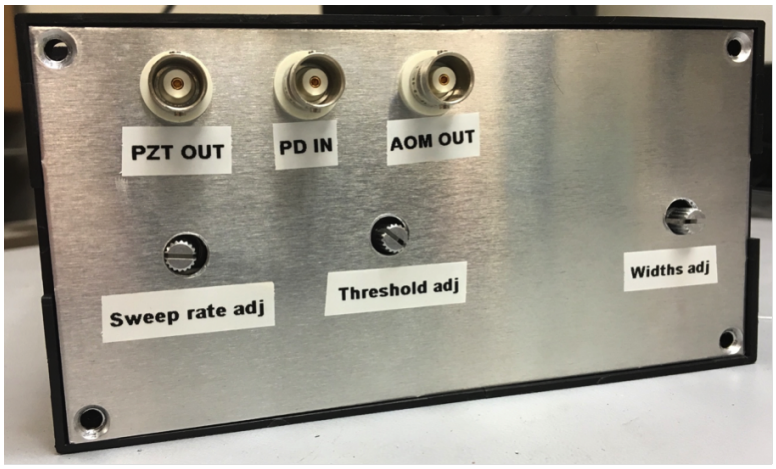

Figure 4.5: Front Panel

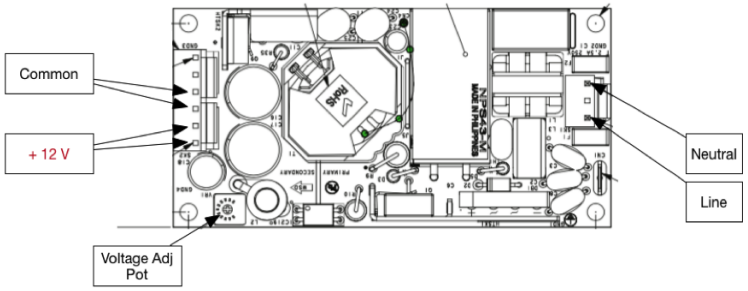

Figure 4.6: 10 V Power supply pin out

4.4.5 Arduino

An Arduino Duemilanove is employed as a microcontroller. A total of five connections are made, Ramp Control IN to AI5, CRDS Event IN to AI5, PZT Sense to AI0, and a feed from the 10 V power supply as shown in Figure 4.7.

4.4.6 Ramp Generator Board

The ramp generator board consists of an Op-amp integrator that transforms the square wave output of the "Ramp Control OUT" pin of the Arduino to a triangle waveform. The "PZT OUT BNC" connector on the front panel provides this triangle wave to the PZT amplifier that drives and sweeps the resonator mirror. Also on the front panel, the "Sweep rate adj" potentiometer adjusts the

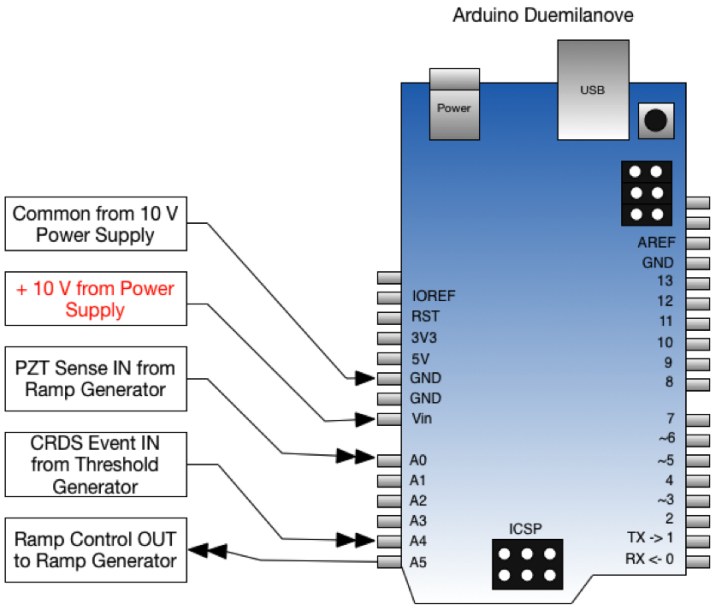

Figure 4.7: Connections to Arduino board

slope of this triangle wave, and thus the velocity and magnitude of the PZT sweep. The circuitry of the Ramp Generator board is constructed as per Figure 4.8 taken from Votava et al. (2012).

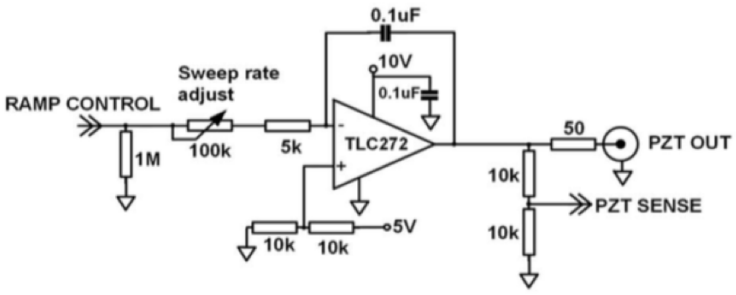

Figure 4.8: Ramp Generator circuit from Votava et al. (2012)

4.4.7 Threshold Generator Boards

The threshold generator board uses an input from photodiode (PD) on the front panel and generates a TTL pulse when a large spike in flux is detected from the PD. This TTL pulse is connected to AI4 on the arduino. The adjustable parameters for resonance detection are on the front panel; the "Threshold adj" potentiometer adjusts the minimum amplitude of resonance, and the "Widths adj" potentiometer adjusts the width of this TTL signal. Another TTL pulse is also generated to actuate the acousto-optical modulator to isolate the diode laser and begin ringdown time measurement. The circuitry of the Threshold Generator board is constructed as per the figure from Votava et al. in Figure 4.9. The 10 nF capacitor connected to 1C was replaced with a 100 nF capacitor in order to increase the off time of the AOM which extends the ringdown time possible with the system.

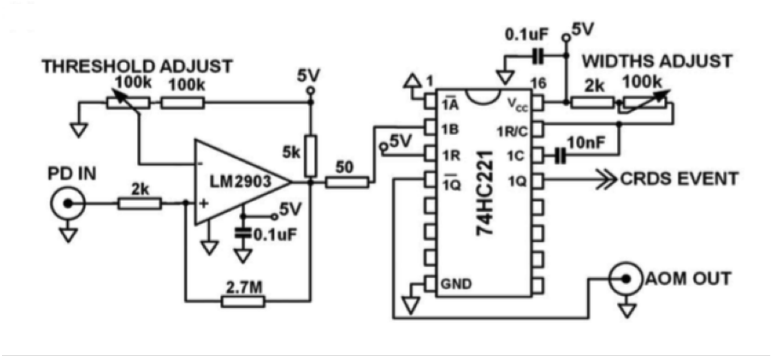

Figure 4.9: Threshold circuit from Votava et al. (2012)

4.4.8 Data Acquisition

Data acquisition may be employed by using AOM OUT as a trigger and capturing PD data as ringdown occurs. The output of the photodiode is collected by an oscilloscope, digitized, and transfered by GPIB to a custom LabVIEW program.

4.4.9 System Interconnection Diagram

An interconnection diagram of the system is shown in Figure 4.10. The RTS system is packaged with 120 VAC incoming power connector and three BNC connectors for signals to the PZT and AOM, and from the photodiode.

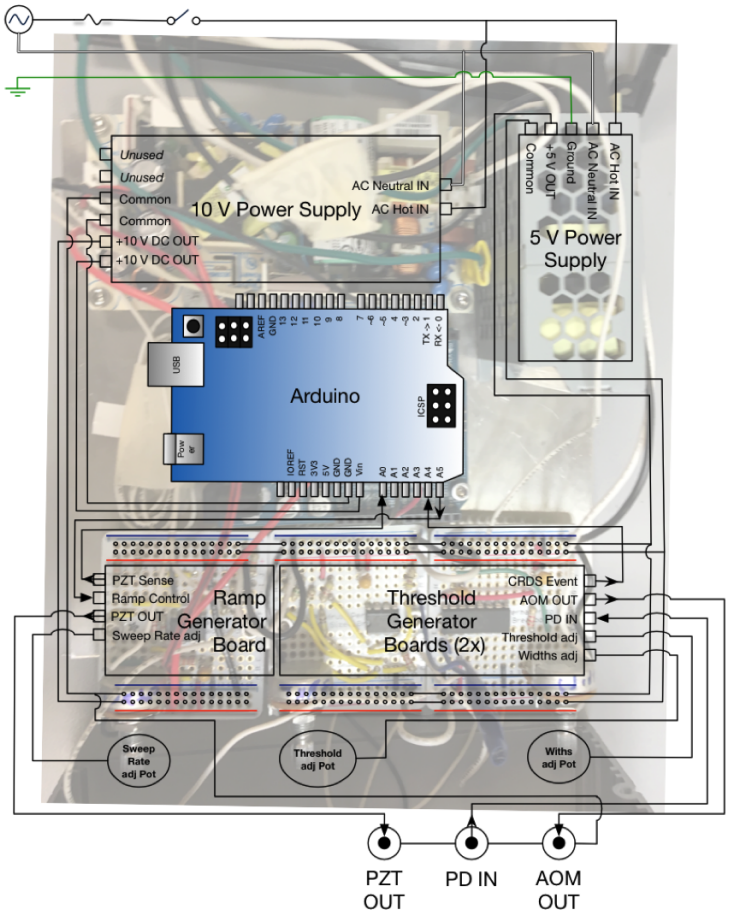

Figure 4.10: RTS System Interconnection. Of note is the Black, White, and Green wires in the top left of the diagram are 120 VAC main hot, neutral, and ground leads, respectively.

Basic startup procedure

Use of a multichannel oscilloscope sampling PD, AOM, and PZT out is recommended to expedite setup and troubleshooting.

1. Laser ON
2. Photodiode ON
3. Resonance Tracking System rear panel power swith ON
4. Load desired program onto Arduino using USB
5. Verify PZT sweep signal and adjust "Sweep rate adj" for desired frequency which resonance will occur
6. Verify resonance via photodiode signal on oscilloscope
7. Verify AOM actuation and adjust "Threshold adj" and "Widths adjust" until AOM is actuated in accordance with resonance peaks

Programming

Programming of the microcontroller was via Arduino Development Environment version 1.6.9 from `http://www.arduino.cc`. It is recommended to use the most recent version for programming. Figure 4.11 shows the pin mapping of the Atmega168 chip

Of importance is the use of C in place of digitalWrite() to decrease the time required to execute each command. **PORTB &= ~_BV(PC5)** is the command to set AI5 to high, and **PORTB |= _BV(PC5)** to set AI5 low. The program is designated per the pin mapping shown in Figure 4.7.

Continuous Wave Laser and Controllers

The initial plan was to use a swept wavelength tunable narrowband laser (Newport NewFocus Venturi 6600). The laser became unavailable after design of the system had begun and alternatives were pursued. Upon suggestion by Dr. Jay Jeffries at Stanford University, a distributed feedback

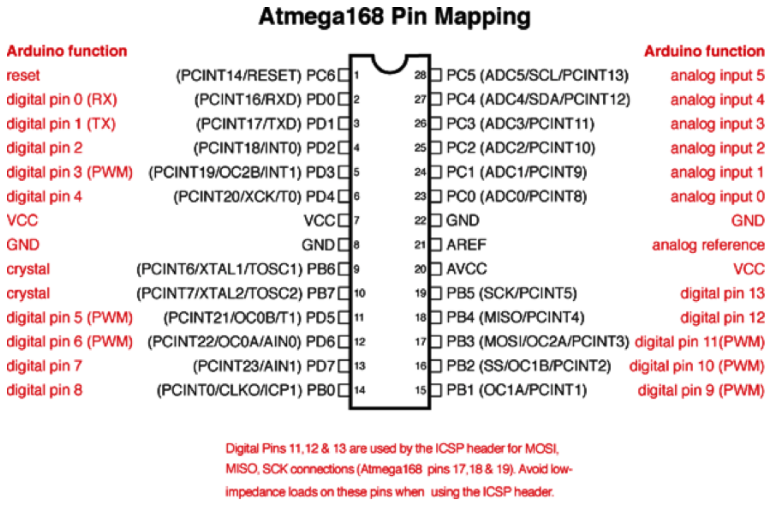

Figure 4.11: Pin mapping for using C commands (Votava et al., 2012)

(DFB) diode laser was purchased from NTT (NLK1E5EAAA 1428.60 nm) [1]. The DFB laser is on a 14 pin butterfly mount which interfaces with thermoelectric cooler (TEC) and current controllers supplied by Arroyo Instruments for the purpose of controlling the wavelength emitted from the laser diode. The temperature control allows a rough control of the laser wavelength within a band of approximately 5 nm. The current controller is used for both laser power and wavelength control. It is important to limit the output of the controller to the laser to less than 20 mA as that is the specification supplied by NTT.

AOM vs. EOM

An acousto-optic modulator (AOM) is most commonly used as the fast optical switch in cw-CRDS. Electro-optic modulators (EOM) have also been used because they are faster at switching, but have sometimes proved problematic for cw-CRDS. Their extinction ratio is limited by the extinction ratio of the polarizers and strain birefringence in the Pockel's cell (Huang and Lehmann, 2008).

An EOM was investigated that is supplied by FastPulse Technology. EOMs work by applying an electric field to a crystal which changes the plane of polarization for linearly polarized light.

[1] A narrative of the search for narrowband laser source can be found in Appendix C.6

A polarizer is placed after the EOM which blocks light that is not in plane with the polarization direction. Although this component has a faster rise and fall time than an AOM - which would provide a cleaner signal during ringdown experiments - the on and off duration are limited to 1 s. Scanning for cavity resonance and ring-up of the signal will take several multiples longer than this. A significant amount of time was spent researching the operation and application of EOMs before recognizing this critical limitation.

AOMs from a few manufacturers have been investigated. They operate by deviating the path of a laser to a 1st order angle and shifting the frequency of the light by the RF acoustic frequency, i.e. 7000 cm^{-1} + 80 MHz = 7000.0026 cm^{-1}. After investigation into the attributes of AOM and EOMs, an AOM has been selected to use with the cw-CEMOR system. It is critical to note that some AOMs do not maintain polarization through the acousto-optic crystal and therefore cannot be used for CEMOR experiments. The AOM used in the cw-CRDS/cw-CEMOR system is from Quanta Tech, model MT80-IIR30-Fio-PM0,5-J1-A-VSF. It is driven by a fixed frequency driver, model MODA80-D41k51k-344575, which has two BNC inputs; a TTL signal for fast triggering by the RTS system based on PD signal, and an input for modulation of the output intensity of the AOM if that is desired. The modulation is not used in this system design.

4.4.10 Wavemeter

The wavemeter used in this system is from Bristol Instruments (821B-NIR). It can measure both cw and pulsed laser sources in the near infrared (630 nm to 1700 nm). This instrument is connected to the data acquisition and control computer (DAQ) via USB cable. Data from the wavemeter can be saved automatically to the computer. Control parameters can be sent from the computer to the wavemeter as well using a custom LabVIEW program.

4.4.11 Optical Isolator and Tap Coupler

An optical isolator (OI) (Fiberon F4M-PMTI-1-43-10-D-9L-25-1) is used to protect the laser diode from reflections back from the optical cavity. This OI also has a tap coupler built in which takes 10% of the incoming light to send to the wavemeter. The remaining 90% is sent to the AOM.

4.4.12 Piezoelectric Transducer/Tubular Piezoelectric Actuator

In the cw-CRDS/CEMOR experimental setup, the second of the cavity mirrors is mounted on a Tubular Piezoelectric Actuator (TPA) to vary the length of the ringdown cavity with a triangle wave signal from the RTS and is driven by a high voltage piezo amplifier.

The TPA (Physik Instrumente PT130.40) is installed between the rear cavity mirror and its mount. It is driven with a matching 1100 V driver (E-508.00) and has a low noise cable to connect them. The cable is attached to the TPA using electrically conductive epoxy (Circuit Works CW2400) which is low temperature oven cured in order to avoid thermal effects of the soldering process on the piezoelectric material. The rear mirror is mounted to the TPA, and the TPA to a kinematic mirror mount, by custom made PTFE mounting pieces (Figures 4.12, B.1, and B.2).

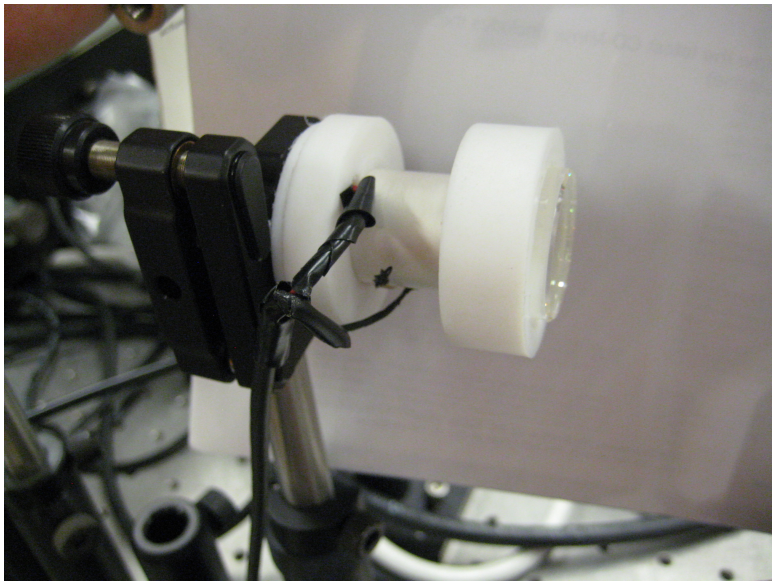

Figure 4.12: The rear mirror mounted to the TPA on a kinematic mirror mount.

4.4.13 Lenses

As with pulsed CRDS, lenses are used to couple the laser into the cavity for spacial filtering and to achieve good mode matching with the fundamental longitudinal cavity mode (TEM_00).

4.4.14 Laser collimator

A collimator (ThorLabs PAF-X-7-C) is used to couple the laser from the fiber to free space before the ringdown cavity. The collimator is designed to have an output which matches the beam waist of the ringdown cavity. The output of bare fiber is uncollimated and expands if not focused using a collimation lens. The collimator provides a beam of specified size (beam waist) with low divergence angle by coupling the fiber to an anti-reflection coated aspheric lens.

4.4.15 Anamorphic prism set

The output cross section of a fiber coupled collimator is elliptical. In order to achieve good mode matching with the circular fundamental Gaussian mode (TEM_{00}) supported by the ringdown cavity, a mounted anamorphic prism pair (Thorlabs PS875-C) is placed in the beam path before mode coupling optics. The prism pair takes the elliptical beam from the laser diode and magnifies it in one direction to create a circular output. The magnification power in the assembled system is 2:1. The prism pair is also antireflection coated in the wavelength of the laser to increase the transmission efficiency. Figure 4.13 shows a cross section of a mounted prism pair.

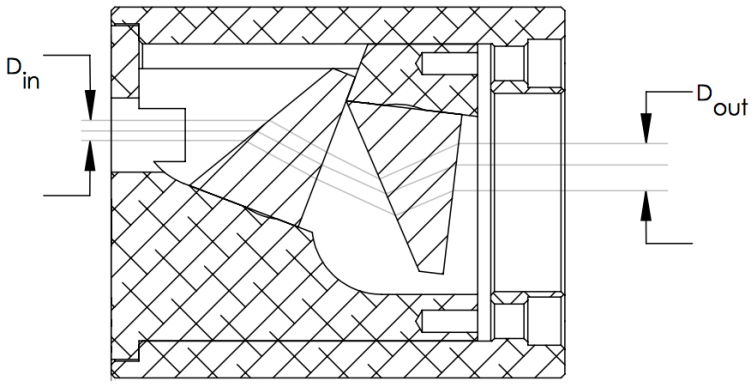

Figure 4.13: A mounted anamorphic prism pair. The ratio of D_{out} to D_{in} is the magnification of the prism pair. (Thorlabs PS875-C)

4.4.16 Avalanche Photodiode

The signal in the ringdown cavity is monitored by an InGaAs amplified photodiode (APD) (Thorlabs PDA10CF) which converts the optical signal to current. This signal is used by the RTS circuitry to trigger the AOM, delay generator, and oscilloscope.

4.4.17 Delay Generator

A four channel delay generator (Quantum Composers Model 9524) is used to coordinate and control the photolysis laser, electromagnet power supply, and wavemeter with the cw-CRDS/CEMOR system.

4.4.18 Power Supply

A solid state interposing relay is used to quickly switch on and off the power supplied to the electromagnetic solenoid. The 600 W power supply can supply up to 117 VDC and 5.1 A to the coil to generate the necessary magnetic field in the FPC.

4.4.19 Data Acquisition and Control Computer (DAQ)

A PC computer (Dell Optiplex 780) is used in order to coordinate control of laboratory instruments and acquire data. This computer replaced an aging one serving a similar purpose, while also integrating the recently acquired instruments for cw-CRDS/CEMOR. The DAQ has LabVIEW integration with the wavemeter, Laser TEC and current controllers, and the oscilloscope.

4.5 Objective: Develop and apply stronger electromagnet for use in Flash Photolysis Cell experiments

We had previously identified that the electromagnet used in the FPC did not provide sufficient magnetic field strength. In order to address this, two tasks were undertaken. The magnetic field strength study described in Section 4.2.4 showed that the strength of the magnetic field has a direct relationship with the MOR signal width and intensity. Further characterization of the CEMOR signal in relation to magnetic field strength is needed.

The first and most simple method to achieve higher magnetic field strength in the FPC is to apply higher current to the solenoid used in previous experiments. The previous power supply was limited to 30 VDC. The solenoid coil had 23.08 ohms. This limited the current to 1.3 A.

A multi-range programmable DC power supply (BK Precision 9206) was purchased for powering the FPC solenoid. This power supply has a maximum power limit of 600 W, 150 VDC and 10 A. For application to our solenoid, it will output 5.1 A at 117 VAC, an increase of nearly three times over the previous maximum current.

4.6 Results and Analysis

To date, there have been no successfully captured ringdown events with the cw-CRDS/CEMOR system. There are a few possible explanations for this.

As described in Section 2.2.5, constructive interference within the ringdown cavity must occur in order for the light intensity in the cavity to build. Constructive interference occurs when the laser frequency matches with a mode supported by the ringdown cavity. The most efficient coupling happens when the beam waist diameter, shape, and focal point of the incoming laser matches the beam waist of the ringdown cavity. A set of lenses is used to precisely match the laser beam waist with the cavity beam waist. It is more difficult to setup this system where constructive interference in the cavity must be achieved in order to see a signal, whereas with a pulsed laser, the linewidth and energy are sufficient to see a signal on each pulse and micro adjustments to the alignment are all that need to be performed in order to achieve a long single exponential decay.

4.7 Magnetic Field Strength

CEMOR: Magnetic Field Strength Characterization

Characterization of the effect of magnetic field strength on CEMOR signal will aid in its application to measurement of radicals. This work will inform design decisions related to the source of the magnetic field in application of CEMOR to measurements of HO_2 in the FPC and cool flame reactors.

Repeating the previous measurements by Lane et al., using MOR and CEMOR on a lean

methane-air slot burner flame forms the basis of this work. Once the system has a baseline, the next step is to vary the distance between the neodymium magnets in order to test the effect of magnetic field strength on the MOR and CEMOR signal.

Initial results are included in Figure 4.14. The chart shows significant noise in the raw data, but also shows the expected exponential decay in signal strength relative to separation distance.

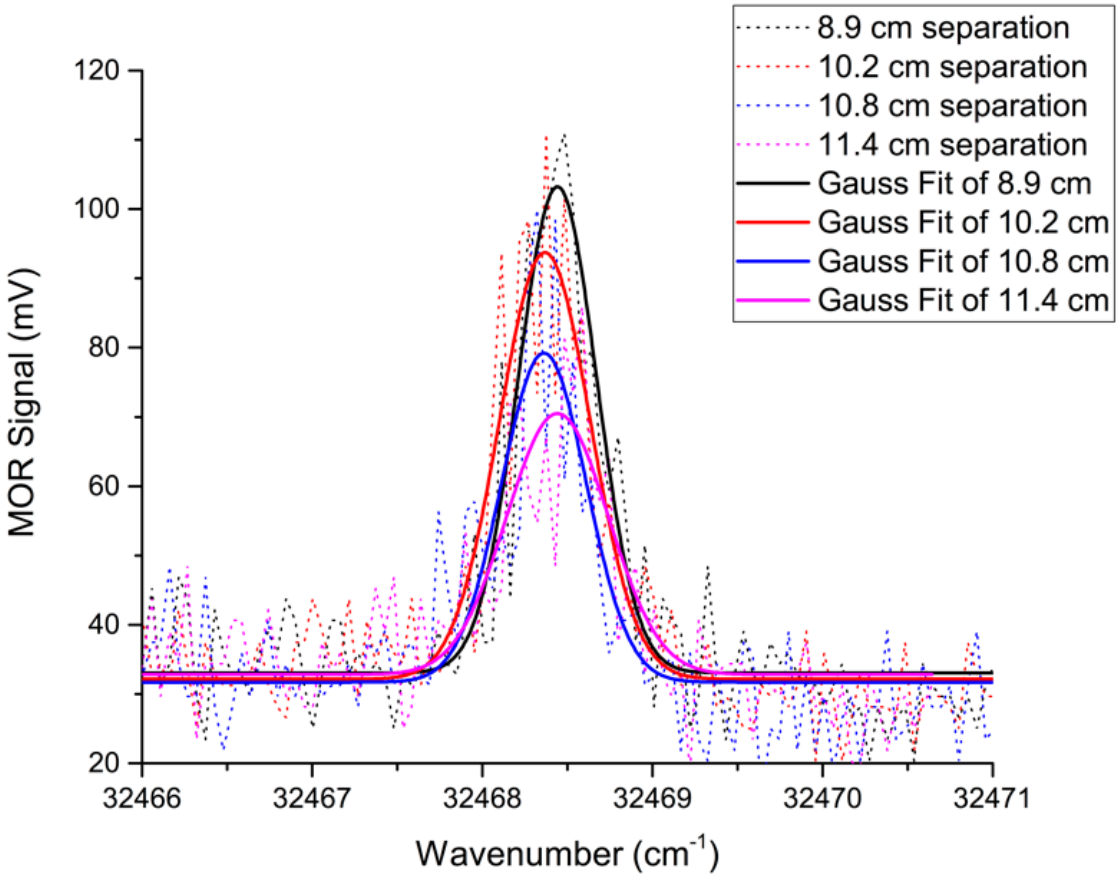

Figure 4.14: Preliminary data from MOR scans of OH $Q_1(1)$ transition in a lean methane-air slot burner flame using pulsed Nd:YAG laser at various separation distance between magnets.

At the conclusion of this experiment we found that the polarizers used were designed for longer wavelength usage. This accounts for the much larger than expected noise and offset in the baseline

signal. The polarizers were crossed, yet unrotated light made it through. Further experimentation with this setup should include the correct polarizers for a stronger signal to noise which will provide improved results with more significant data.

4.7.1 Modeling of Magnetic Field

FEMM

FEMM 4.2 was used for this modeling work. FEMM is designed by David Meeker for magnetostatic modeling. The codes for permanent magnet separation and solenoid modeling can be found in Appendix A where there are also instructions for installing and running the FEMM software on a macOS computer.

Comparison of Magnetic Field Models

Based on the decision to increase the magnetic field strength within the FPC, a modeling study was performed which included FEMM models of permanent magnets and solenoid. Electromagnets are able to achieve higher magnetic field strengths when sufficient power is supplied and cooling is considered.

FPC Electromagnet

As described earlier, the magnetic field strength in the FPC may be too weak to cause sufficient Zeeman splitting to register a detectable signal. The electromagnetic coil has been designed to maximize the magnetic field strength within the internal dimensions of the FPC.

An option to increase the strength of the magnetic field without changing the overlap of the lasers is to increase the electrical current supplied to the electromagnet coil. In order to avoid overtemp of the coil, water cooling can be added to dissipate the joule heating from the coil. Another option to avoid an over-temperature situation with the electromagnet is to more closely control the timing of the high current pulses delivered to it by reducing the duration of the electromagnet's current pulse and the delay between the laser and current pulses.

The software program Finite Element Method Magnetics (FEMM) was used to model the

present magnetic field strength and the effect of using increased current in the present coil to achieve a greater magnetic field strength. The results of this study are presented in Figures 4.15, 4.16, 4.17 and 4.18. Further increasing the magnetic field strength is desirable in order to cause increased Zeeman effect. Application of sufficiently high current to achieve more desirable magnetic field strength would require water cooling to dissipate the heat generated by the coil and a significantly more powerful power supply than is currently in the lab would be necessary.

Ju et al., used a pair of Helmholtz coils to generate the magnetic field in their measurements of HO_2 (Brumfield et al., 2014). Helmholtz coils are designed to have the same radius distance as the separation distance. This allows for a larger open area for chemistry and spectroscopy; especially where the laser and magnetic field are in a Faraday configuration (they are parallel) and they cross the exit of a reactor. Helmholtz coils have the advantage of a nearly homogeneous magnetic field at their axis. The linear relationship of radius and separation distance causes the distance between the axis and the coil to become quite large. It may be because of this that in more recent experiments, they used a water cooled solenoid to generate the required magnetic field (Ju et al., 2016).

4.8 Closure

A continuous wave CRDS/CEMOR system has been designed and constructed for measurement of the $\tilde{A} - \tilde{X}$ band near 1429 nm. This system incorporates lessons learned in previous CEMOR development work with pulsed lasers, and expands upon the capabilities by increasing the resolution through use of narrow band (0.0001 cm^{-1}) DFB laser and associated additional necessary components.

Although successful application of this experimental setup has not been achieved, sources of the problems have been identified for future work to be performed.

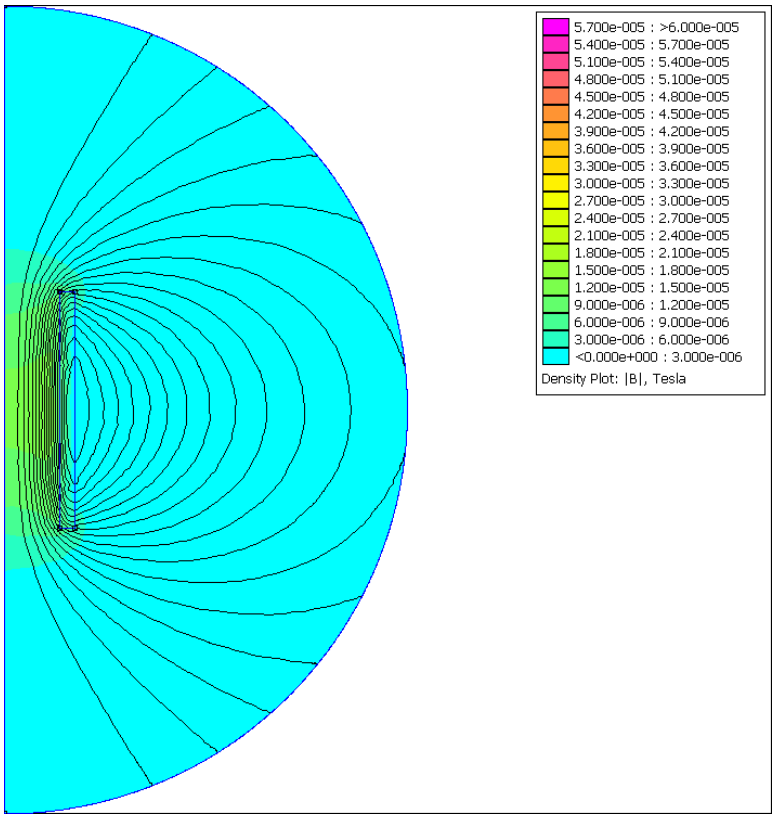

Figure 4.15: Solenoid in FPC with 1.3 A current.

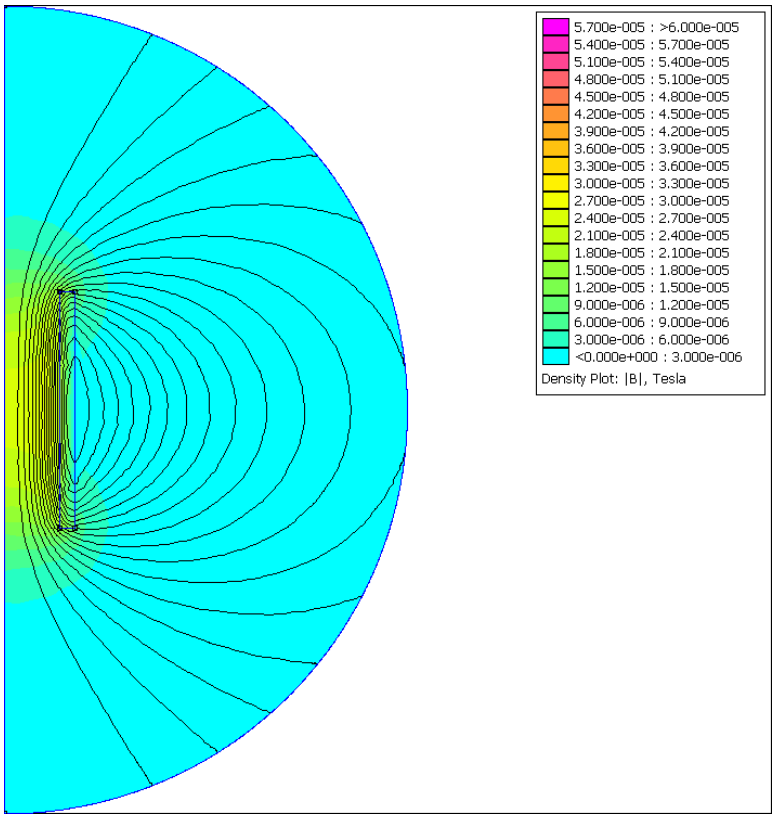

Figure 4.16: Solenoid in FPC with 2.6 A current.

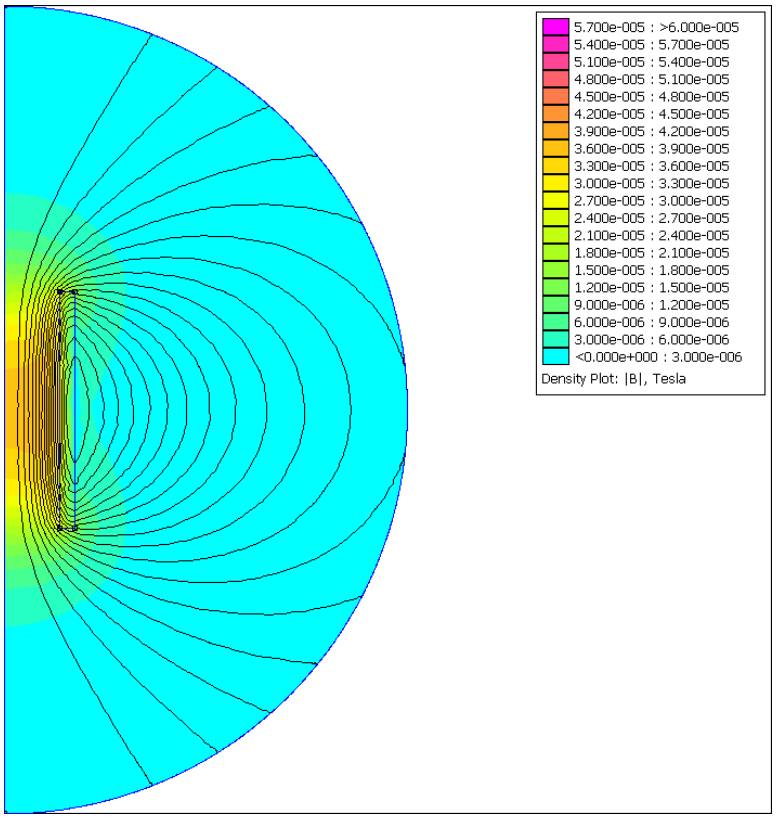

Figure 4.17: Solenoid in FPC with 3.9 A current.

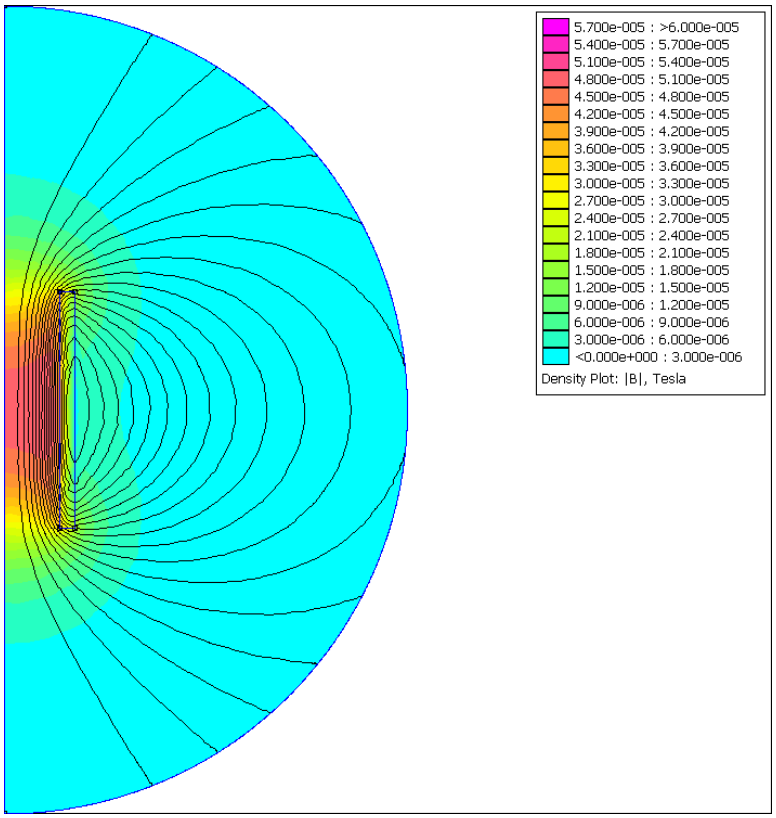

Figure 4.18: Solenoid in FPC with 5.2 A current.

5. Peroxy Radicals in Flash Photolysis Cell

5.1 Introduction

The main goal of this work was to develop the cw-CEMOR method to measure peroxy radicals in our FPC. In order to accomplish that goal modeling studies were performed with CHEMKIN-PRO software and modification of the GRI-Mech chemical kinetic mechanism in conditions similar to the flash photolysis facility where HO_2 was generated and measured with the cw-CEMOR spectroscopy method.

5.2 Experimental Results

5.2.1 CRDS HO_2 Results

Upon experimental setup of the Flash Photolysis Cell (FPC), Lane et al. (2013) performed measurements of HO_2 using CRDS. Results from the CRDS scans in the photolysis cell are shown in Figure 5.1. The initial CRD scan at 30 μs delay from the photolysis pulse provided the orange spectrum shown. The delay between photolysis pulse and probe pulse was changed to 100 μs to achieve the black spectrum. This spectrum has a similar profile but reduced per pass absorption loss due to lower concentration of HO_2 from the self reaction; this decay in signal intensity is expected.

Another CRD scan was performed with the photolysis beam blocked and this scan is shown in red as the baseline. Once again there are some similar peak locations indicating that the presense of some of the same species within the cell while photolysis is on and off. Separately, as part of an investigation of the linewidth of the laser, we introduced air with 25% RH H_2O at 60 Torr into the cell with no photolysis action. When overlaying that scan it can, it can easily be seen that the baseline scan matches well with the water vapor scan along much of the spectrum. Because the experimental conditions (pressure and scan rate) between the H_2O and the HO_2 scans were different, a statistical analysis of the baseline and water vapor scans would not provide meaningful results.

Some of these peaks such as 7000 cm^{-1} and the left portion at 6996 cm^{-1} are present with photolysis on and off, but at 6998 cm^{-1} the peak is very much reduced and nearly absent. There is

strong absorption of HO_2 at this location which corresponds to the ($A^2A' \leftarrow X^2A''$). In this experiment we were able to measure HO_2 with CRDS in the photolysis cell and detected the expected reduction in concentration after the self reaction.

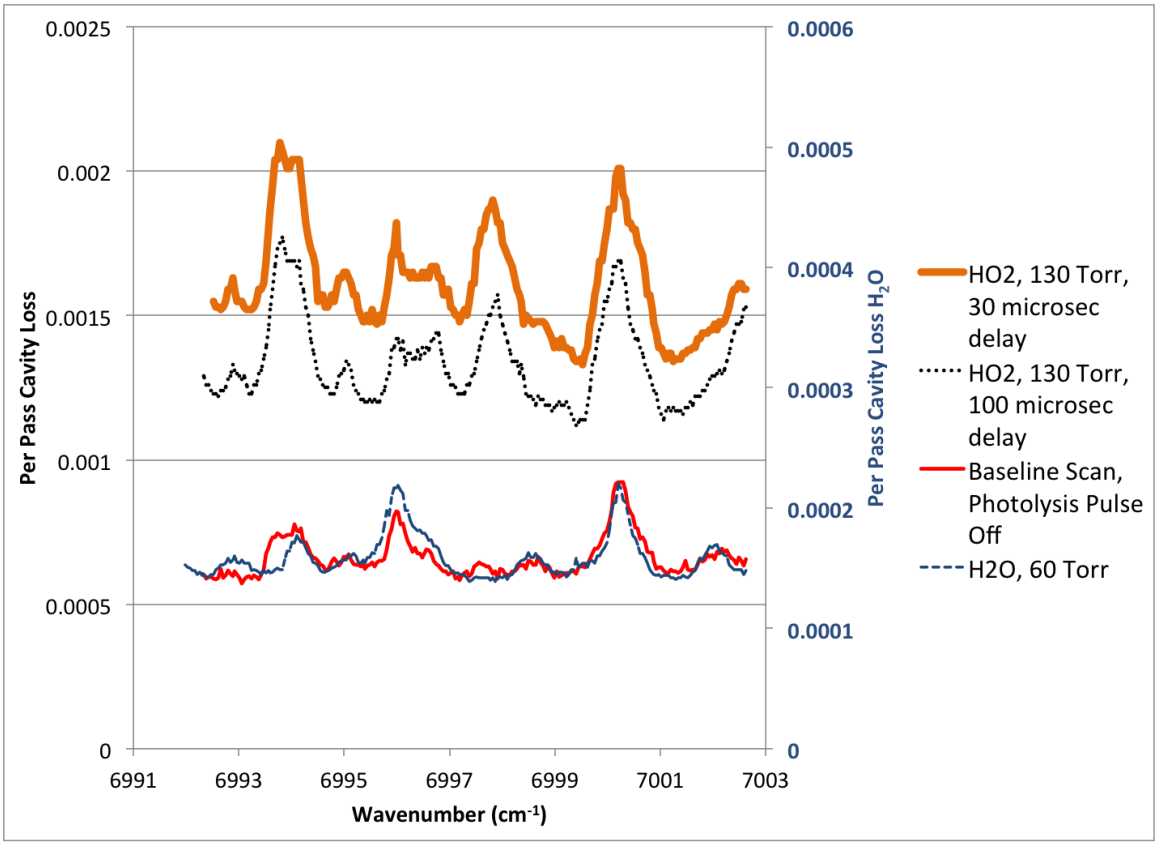

Figure 5.1: Measurements of HO_2 and H_2O in the photolysis cell. The region near 6998 cm^{-1} shows unique HO_2 signal corresponding to the low lying electronic transition band at $A^2A' \leftarrow X^2A''$.

5.3 Modeling

A simple modeling study was performed to show the expected chemical reactions within the photolysis cell.

5.3.1 Mechanism Development

The CHEMKIN PRO software suite was used to simulate the reaction of radicals with methanol under constant volume and energy constraints with GRI-Mech 3 by Smith et al. (2014) as a comprehensive base reaction mechanism. The GRI Mechanism does not include chlorine chemistry. Initially, a tool called Reaction Mechanism Generator (RMG-Py), developed in the Green Group at MIT (Gao et al., 2016), was investigated to generate the needed reaction mechanisms, but after contact with the creaters, this tool was determined to have no ability to include chlorine. NASA polynomials were generated using the THERM program (Ritter and Bozzelli, 1991).

Modeling chlorine photolysis in methane and oxygen was complicated by the lack of resources on chlorine reaction mechanisms. The modeling process involved having to generate a list of possible reactions and choose which are important. This involved having to manually work around the lack of support for chlorine in Reaction Mechanism Generator (RMG) software. The end result is a mechanism for chlorine reactions in a methanol environment complete with thermodynamic data. Table 5.1 lists the reaction rate parameters for several chlorine reactions of interest that were added to rate coefficients from GRI-Mech 3.0 used for modeling the reactions occurring in the FPC.

5.3.2 HO_2

Figures 5.2 and 5.3 show the reaction rates of the six most sensitive reactions relative to HO_2. The reaction of Cl with methanol is the first reaction in the simple mechanism, responsible for generating CH_2OH which combines with O_2 to create HO_2 in second reaction in the simple model. Both of these reactions contribute to the creation of HO_2.

However, reactions not included in the simple model are prominent and serve to limit the creation of HO_2. These include the reaction of CH_2OH with Cl which limits the amount of CH_2OH available for reaction with O_2 to produce HO_2. The product CH_2O from the reaction of CH_2OH can eventually contribute to the production of HO_2 in ways not described by the simple model but nonetheless limits the amount of HO_2 produced. The product CH_3OCl is less reactive and hinders HO_2 production more.

Because of primarily these two reactions, the detailed model indicates a much lower concentra-

Table 5.1: Chlorine reactions in modified Arrhenius format where $T_0 = 298\ K$

Reaction: k(T) = A (T/298 K)n exp(-Ea/RT)	A(cm3/(mole*s)	n	Ea (kJ/mole)
$CH_2OH + Cl \Rightarrow CH_3OCl$	5.25E+13	0.3	0
$CH_2OH + Cl \Rightarrow CH_2O + HCl$	3.99E+14	0	0
$O_2 + Cl \Rightarrow ClOO$	5.22E+14	-3.9	0
$ClOO \Rightarrow O_2 + Cl$	8.79E+14	0	15.13
$CH_3OH + Cl \Rightarrow CH_2OH + HCl$	3.31E+13	0	0
$CH_2OH + HCl \Rightarrow CH_3OH + Cl$	4.37E+11	-0.2	23.52
$HO_2 + Cl \Rightarrow HCl + O_2$	1.08E+13	0	-1.41
$HO_2 + Cl \Rightarrow OH + ClO$	2.46E+13	0	3.74
$OH + ClO \Rightarrow HO_2 + Cl$	1.14E+13	0	0
$H_2O_2 + Cl \Rightarrow HO_2 + HCl$	6.63E+12	0	8.15
$CH_2O + Cl \Rightarrow CHO + HCl$	4.93E+13	0	0.28
$CH_3O + Cl \Rightarrow CH_2O + HCl$	1.15E+13	0	0
$CH_3O_2 + Cl \Rightarrow CH_3O + ClO$	4.63E+13	0	0
$CH_3O_2 + Cl \Rightarrow HCl + CH_2OO$	4.46E+13	0	0
$HCl + Cl \Rightarrow Cl_2 + H$	9.99E+16	0	199
$Cl_2 + H \Rightarrow HCl + Cl$	8.61E+13	0	4.91
$HCl + OH \Rightarrow H_2O + Cl$	1.02E+12	0	1.91
$CH_3O + HCl \Rightarrow CH_3OH + Cl$	1.6E+10	2.5	18.54
$CH_3OH + Cl \Rightarrow CH_3O + HCl$	1.30E+04	13.89	-17.3

tion of HO_2 than the simple model.

5.4 Closure

The HO_2 detection results in the FPC by (Lane et al., 2013) have shown that CRDS measurement of peroxy radicals is possible in our photolysis cell. It is also shown that the background signal is primarily from water vapor. A CHEMKIN-PRO model has been created to compare to the experimental results, but requires some fine tuning.

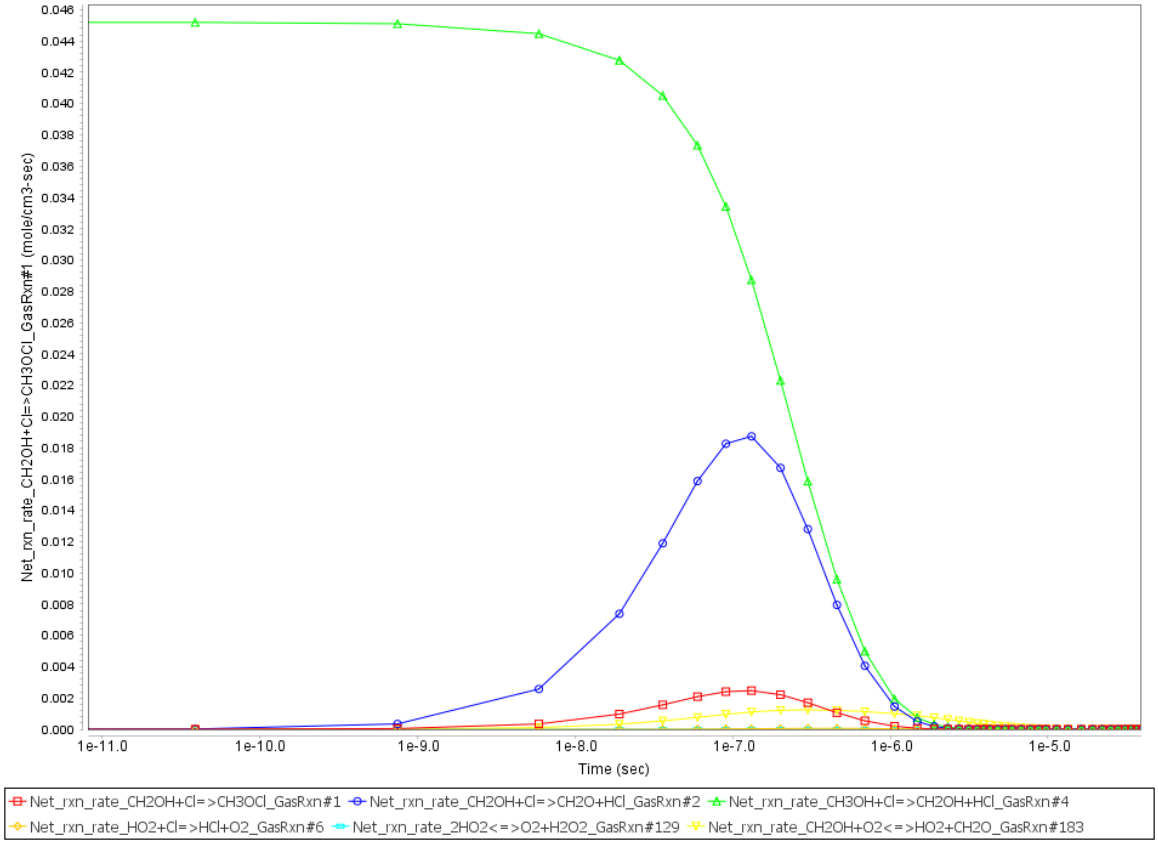

Figure 5.2: Reaction rates of Cl sensitive reactions in FPC for HO_2 production

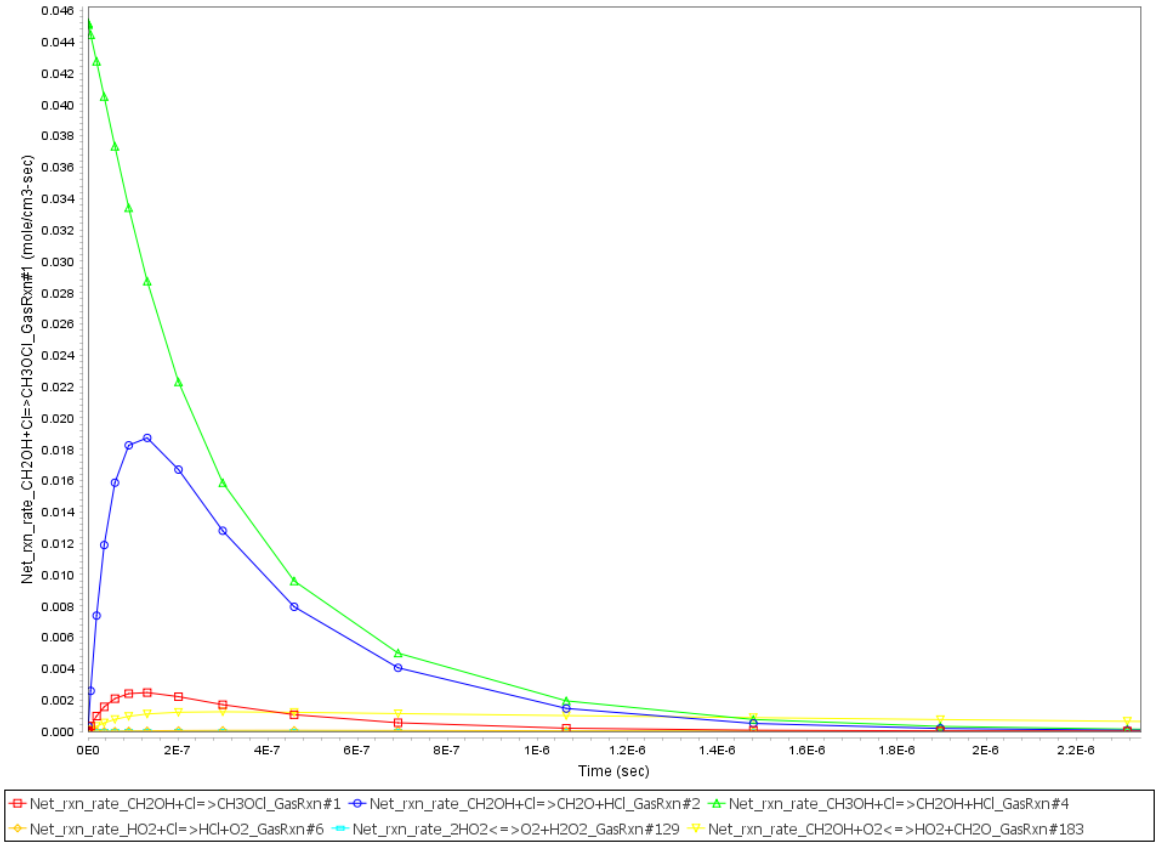

Figure 5.3: Reaction rates of Cl sensitive reactions in FPC for HO_2 production

6. Summary and Conclusion

Analysis of previous results of HO_2 measured in our photolysis cell have shown that a significant contribution to the measured absorption scans using CRDS in the FPC is from water vapor.

In the course of this study a new spectroscopy facility, called continuous wave cavity enhanced magneto-optic rotation (cw-CEMOR) was built at Drexel University.

While simultaneously undertaking the tasks of characterization of magnetic field strength on MOR, and development of cw-CRDS and cw-CEMOR, deficiencies and limitations were found in the pulse laser used and the SCFR. At the same time, the laser lab was moved to storage while a new lab was setup.

The intellectual merit of this work is found in the design of a novel laser spectroscopy technique which is capable of sensitive and selective detection of paramagnetic species. This initial work did not demonstrate successful application of continuous wave CEMOR to measurement of HO_2, yet it provides a path forward for this goal in a flash photolysis cell and cool flame burner. The present work also provides a method which can easily be adapted to measurement of alkyl peroxy (RO_2) radicals.

6.1 Suggestions for Future Related Work

Due to the unsuccessful application of cw-CRDS (and therefore cw-CEMOR) technique in our lab, it is suggested to further investigate the cw-CRDS technique and collaborate with other groups that have successfully applied it to peroxy radical measurements in photolysis reactors and in combustion environments. Section 2.6.1 lists some of the successful efforts in this field. Lehmann and Romanini (1996) describe the sensitivity of mode-matching of cavity modes, and this may be the key to successful application of cw-CRDS.

Once cw-CRDS and cw-CEMOR have been applied to the photolysis cell, the revised objectives of this work can be carried out; specifically,

- Characterize and calibrate the CEMOR system for HO_2 quantification

- Characterize the effect of magnetic field strength on the CEMOR signal
- Measure HO_2 at preignition conditions using CEMOR in Pre-Flame/Cool Flame
- Repeat steps 1-3 to characterize and measure C_3 alkylperoxy radical

Couple CEMOR with our SCFR

Apply the cw-CEMOR technique to the SCFR. This will require customizing the cw-CEMOR and SCFR systems to work together. The end goal of this work is to quantitatively measure HO_2 profiles at pre-flame conditions in our SCFR to complement existing OH and stable reaction intermediate and product data. Some challenges that will need to be addressed for successful completion of this step are mentioned in Jamie Lane's PhD Dissertation (Lane, 2012) and listed below:

- Beam steering due to density fluctuations across the 6 cm flame in the SCFR.
- Air-broadening of HO_2 lines at atmospheric pressures.
- For successful measurement of HO_2 in the SCFR, CEMOR will need to demonstrate detection limits near that of cavity ringdown. This has been demonstrated with previous OH studies in slot burner flame with 99.5% reflective mirrors. 99.9% reflective mirrors will need to be used to measure HO_2 in the SCFR. This will also add to beam steering challenges because of the increased pathlength associated with higher reflectivity mirrors.

Cool Flame Burner

In order to address the beam steering and air-broadening issues, low pressure operation of SCFR for HO_2 measurements should be considered. At low pressure, density fluctuations across the flame will decrease. Doppler and collisional broadening of the HO_2 lineshape is less at lower pressure as well.

6.1.1 Counterflow Burner

Alternatively, a counterflow cool flame diffusion burner such as is used by the Ju group (Won et al., 2015) could be implemented. This type of experimental setup would yield a more stable flame

with reduced thermal gradient fluctuations and more predictable beam steering.

6.1.2 Slot Burner

The slot burner that was used in previous MOR/CEMOR experiments has been considered for stabilization and use for pre-flame reaction zone studies. Testing was performed to qualitatively determine whether high flow rate propane-air flames could be stabilized in such a way that CRDS and CEMOR experiments could be performed. Figure 6.1 shows a lifted turbulent propane-air premixed flame which is stabilized by a screen. The turbulence makes it unsuitable for ringdown diagnostic study due to rapidly changing densities which cause thermal lensing and introduce noise in the ringdown signal. Figure 6.2 shows a zoomed in view of a lifted laminar premixed propane-air flame that could be used either longitudinally or laterally in the pre-flame region. Figure 6.3 shows a partially premixed flame with a wider pre-flame region that could be accessed with a laser in the longitudinal direction.

Figure 6.4 is an example of a propane-air flame in the slot burner that is mostly diffusion. The blue flames are separated enough that a longitudinal beam path could be used to study the preflame region. Care must be taken to consider that the ends of the slot burner will have some flame. This means that the temperature along the full line of sight will not be homogeneous which will contribute to thermal lensing and additional species not found in the preflame region.

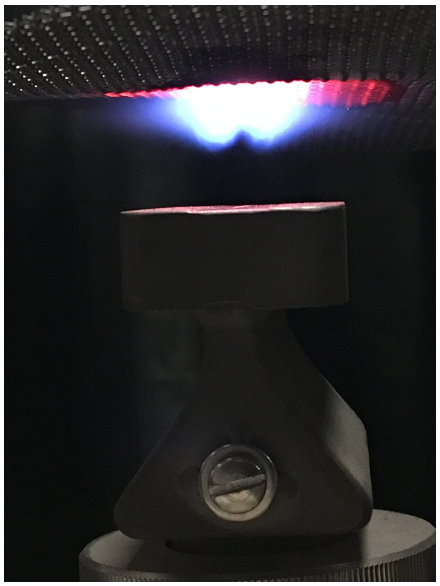

Figure 6.1: Propane-air flame under screen.

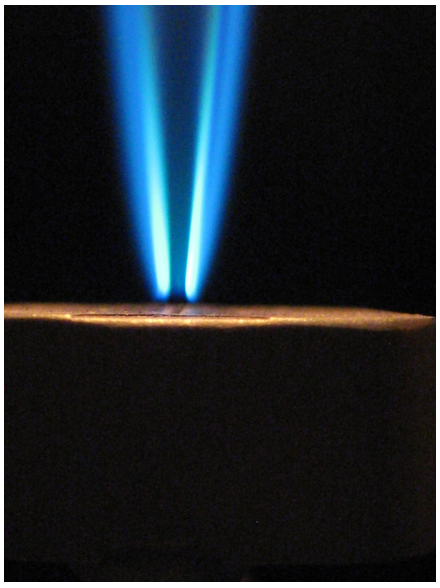

Figure 6.2: A zoomed in view of the lifted flame.

Figure 6.3: Longitudinal path in pre-mixed propane-air slot burner flame.

Figure 6.4: Longitudinal path in diffusion propane-air slot burner flame.

Bibliography

D. Z. Anderson, J. C. Frisch, and C. S. Masser. Mirror reflectometer based on optical cavity decay time. *Applied Optics*, 23(8):1238–1245, Apr 1984.

D. B. Atkinson. Spectroscopy and kinetics of organic peroxy radicals measured using a laser photolysis / CW cavity ring-down reactor. *AGU Fall Meeting Abstracts*, Dec. 2001.

D. B. Atkinson and J. L. Spillman. Alkyl peroxy radical kinetics measured using near-infrared CW-cavity ring-down spectroscopy. *J. Phys. Chem. A*, 106(38):8891–8902, 2002.

R. Atkinson, D. L. Baulch, R. A. Cox, R. F. Hampson, J. A. Kerr, M. J. Rossi, and J. Troe. Evaluated kinetic, photochemical and heterogeneous data for atmospheric chemistry: Supplement V. IUPAC subcommittee on gas kinetic data evaluation for atmospheric chemistry. *Journal of Physical and Chemical Reference Data*, 26(3):521–1011, May 1997.

C. Bahrini, O. Herbinet, P.-A. Glaude, C. Schoemaecker, C. Fittschen, and F. Battin-Leclerc. Detection of some stable species during the oxidation of methane by coupling a jet-stirred reactor (JSR) to cw-CRDS. *Chemical Physics Letters*, 534:1 – 7, 2012.

P. Ballinger and P. Ryason. Isolated stable cool flames of hydrocarbons. *Symposium (International) on Combustion*, 13(1):271 – 277, 1971.

G. Berden and R. Engeln. *Cavity Ring-Down Spectroscopy: Techniques and Applications*. Wiley, 2009. ISBN 978-1-4443-0824-2.

G. Berden, R. Engeln, P. C. M. Christianen, J. C. Maan, and G. Meijer. Cavity-ring-down spectroscopy on the oxygen *A* band in magnetic fields up to 20 T. *Phys. Rev. A*, 58:3114–3123, Oct 1998.

D. S. Bomse, A. C. Stanton, and J. A. Silver. Frequency modulation and wavelength modulation spectroscopies: Comparison of experimental methods using a lead-salt diode laser. *Appl. Opt.*, 31(6):718–731, Feb 1992.

R. J. Brecha, L. M. Pedrotti, and D. Krause. Magnetic rotation spectroscopy of molecular oxygen with a diode laser. *J. Opt. Soc. Am. B*, 14(8):1921–1930, Aug 1997.

B. Brumfield, W. Sun, Y. Ju, and G. Wysocki. Direct in situ quantification of HO_2 from a flow reactor. *The Journal of Physical Chemistry Letters*, 4(6):872–876, 2013.

B. Brumfield, W. Sun, Y. Wang, Y. Ju, and G. Wysocki. Dual modulation Faraday rotation spectroscopy of HO_2 in a flow reactor. *Opt. Lett.*, 39(7):1783–1786, Apr 2014.

T. Carroll. Magnetic rotation spectra of diatomic molecules. *Phys. Rev.*, 52:822–835, Oct 1937.

T. J. Carroll. *The Faraday Effect in Molecular Spectra*. PhD thesis, Yale University, 1936.

R. Chhantyal-Pun, N. D. Kline, P. S. Thomas, and T. A. Miller. Observation of the $\widetilde{A} \leftarrow \widetilde{X}$ electronic transition of the beta -hydroxyethylperoxy radical. *The Journal of Physical Chemistry Letters*, 1(12):1846–1852, 2010.

M. Djehiche, N. L. Le Tan, C. D. Jain, G. Dayma, P. Dagaut, C. Chauveau, L. Pillier, and A. Tomas. Quantitative measurements of HO_2 and other products of n-butane oxidation (H_2O_2, H_2O, CH_2O, and C_2H_4) at elevated temperatures by direct coupling of a jet-stirred reactor with sampling nozzle and cavity ring-down spectroscopy (cw-CRDS). *Journal of the American Chemical Society*, 136 (47):16689–16694, 2014.

M. Emig, R. I. Billmers, N. P. Cernansky, D. L. Miller, and K. G. Owens. Cavity enhanced magneto-optic rotation spectroscopy of combustion generated radicals. In *Lasers and Electro-Optics, 2002. CLEO '02. Technical Digest. Summaries of Papers Presented*, pages 628–629 vol.1, May 2002a.

M. Emig, R. I. Billmers, K. G. Owens, N. P. Cernansky, D. L. Miller, and F. A. Narducci. Sensitive and selective detection of paramagnetic species using cavity enhanced magneto-optic rotation. *Appl. Spectrosc.*, 56(7):863–868, Jul 2002b.

R. Engeln, G. Berden, E. van den Berg, and G. Meijer. Polarization dependent cavity ring down spectroscopy. *The Journal of Chemical Physics*, 107(12):4458–4467, 1997.

R. Engeln, G. Berden, R. Peeters, and G. Meijer. Cavity enhanced absorption and cavity enhanced magnetic rotation spectroscopy. *Review of Scientific Instruments*, 69(11):3763–3769, 1998.

E. P. Faragó, C. Schoemaecker, B. Viskolcz, and C. Fittschen. Experimental determination of the rate constant of the reaction between $C_2H_5O_2$ and OH radicals. *Chemical Physics Letters*, 619: 196 – 200, 2015.

C. Fittschen. Simultaneous time-resolved detection of trace species using high repetition rate LIF and cw-CRDS. In *Lasers, Sources, and Related Photonic Devices*, page LT3B.3. Optical Society of America, 2012.

C. W. Gao, J. W. Allen, W. H. Green, and R. H. West. Reaction mechanism generator: Automatic construction of chemical kinetic mechanisms. *Comp. Phys. Comm.*, 203:212 – 225, 2016.

B. G. Glover and T. A. Miller. Near-IR cavity ringdown spectroscopy and kinetics of the isomers and conformers of the butyl peroxy radical. *The Journal of Physical Chemistry A*, 109(49): 11191–11197, Dec. 2005.

D. Herriott, H. Kogelnik, and R. Kompfner. Off-axis paths in spherical mirror interferometers. *Appl. Opt.*, 3(4):523–526, Apr 1964.

G. Herzberg. *Molecular Spectra and Molecular Structure: Spectra of Diatomic Molecules*, volume 1 of *Molecular Spectra and Molecular Structure*. Van Nostrand, 1945.

G. Herzberg and J. W. T. Spinks. *Atomic Spectra and Atomic Structure*. Dover publications, 1944.

Z. Hong, K.-Y. Lam, R. Sur, S. Wang, D. F. Davidson, and R. K. Hanson. On the rate constants of OH + HO_2 and HO_2 + HO_2: A comprehensive study of H_2O_2 thermal decomposition using multi-species laser absorption. *Proceedings of the Combustion Institute*, 34(1):565 – 571, 2013.

H. Huang and K. K. Lehmann. CW cavity ring-down spectroscopy (CRDS) with a semiconductor optical amplifier as intensity modulator. *Chemical Physics Letters*, 463(1-3):246 – 250, 2008.

N. Ibrahim, J. Thiebaud, J. Orphal, and C. Fittschen. Air-broadening coefficients of the HO_2 radical in the 2v1 band measured using cw-CRDS. *J. Mol. Spect.*, 242(1):64 – 69, 2007.

F. Incropera. *Introduction to Molecular Structure and Thermodynamics*. John Wiley & Sons Canada, Limited, 1974. ISBN 9780471427100.

T. Johnson, F. Wienhold, J. Burrows, G. Harris, and H. Burkhard. Measurements of line strengths in the hydroperoxy ν_1 overtone band at 1.5 μm using an indium gallium arsenide phosphide laser. *The Journal of Physical Chemistry*, 95(17):6499–6502, 1991.

Y. Ju, J. K. Lefkowitz, C. B. Reuter, S. H. Won, X. Yang, S. Yang, W. Sun, Z. Jiang, and Q. Chen. Plasma assisted low temperature combustion. *Plasma Chemistry and Plasma Processing*, 36(1): 85–105, 2016.

J. J. Kankare and R. Stephens. A unified theory of magneto-optic phenomena in analytical atomic spectroscopy. *Spectrochimica Acta Part B: Atomic Spectroscopy*, 35(11-12):849 – 864, 1980.

S. Kassi and A. Campargue. Cavity ring down spectroscopy with 5 x 10^{-13} cm^{-1} sensitivity. *The Journal of Chemical Physics*, 137(23):234201, 2012.

H. Kogelnik. Matching of optical modes. *The Bell System Technical Journal*, 43(1):334–337, Jan 1964.

K. Kohse-Höinghaus and J. B. Jeffries. *Applied Combustion Diagnostics*. Applied Combustion Diagnostics. Taylor & Francis, 2002. ISBN 9781560329138.

J. Lane, M. Stichter, N. Cernansky, and D. Miller. Selective observation of the anomalous Zeeman effect using magneto-optic rotation. *Fall Technical Meeting of the Eastern States Section of the Combustion Institute*, 2011.

J. L. Lane. *Development of a Sensitive and Selective Laser Diagnostic Technique for Measuring Paramagnetic Species*. PhD thesis, Drexel University, June 2012.

J. L. Lane, N. P. Cernansky, and D. L. Miller. A stabilized cool flame reactor for laser diagnostic studies of HO_2 and OH radicals at pre-ignition reaction conditions. *Fall Technical Meeting of the Eastern States Section of the Combustion Institute*, 2009.

J. L. Lane, M. A. Stichter, N. P. Cernansky, and D. L. Miller. A flash photolysis facility for fundamental HO_2 studies. *8th U.S. National Technical Meeting of the Combustion Institute*, 2013.

N. Laurendeau. *Statistical Thermodynamics: Fundamentals and Applications*. Cambridge University Press, 2005.

N. L. Le Tan, M. Djehiche, C. D. Jain, P. Dagaut, and G. Dayma. Quantification of HO_2 and other products of dimethyl ether oxidation (H_2O_2, H_2O, and CH_2O) in a jet-stirred reactor at elevated temperatures by low-pressure sampling and continuous-wave cavity ring-down spectroscopy. *Fuel*, 158:248 – 252, 2015.

K. K. Lehmann and D. Romanini. The superposition principle and cavity ring-down spectroscopy. *The Journal of Chemical Physics*, 105(23):10263–10277, 1996.

P. Macko, D. Romanini, S. Mikhailenko, O. Naumenko, S. Kassi, A. Jenouvrier, V. Tyuterev, and A. Campargue. High sensitivity CW-cavity ring down spectroscopy of water in the region of the 1.5 μm atmospheric window. *Journal of Molecular Spectroscopy*, 227(1):90 – 108, 2004.

M. C. McCarthy, J. C. Bloch, and R. W. Field. Frequency-modulation enhanced magnetic rotation spectroscopy: A sensitive and selective absorption scheme for paramagnetic molecules. *The Journal of Chemical Physics*, 100(9):6331–6346, 1994.

D. Melnik, R. Chhantyal-Pun, and T. A. Miller. Measurements of the absolute absorption cross sections of the $\widetilde{A} \leftarrow \widetilde{X}$ transition in organic peroxy radicals by dual-wavelength cavity ring-down spectroscopy. *The Journal of Physical Chemistry A*, 114(43):11583–11594, 2010.

S. Mikhailenko, D. Mondelain, S. Kassi, and A. Campargue. An accurate and complete empirical line list for water vapor between 5850 and 7920 cm^{-1}. *Journal of Quantitative Spectroscopy and Radiative Transfer*, 140:48 – 57, 2014.

J. Morville, D. Romanini, A. Kachanov, and M. Chenevier. Two schemes for trace detection using cavity ringdown spectroscopy. *Applied Physics B*, 78(3):465–476, 2004.

A. O'Keefe and D. A. G. Deacon. Cavity ring-down optical spectrometer for absorption measurements using pulsed laser sources. *Review of Scientific Instruments*, 59(12):2544–2551, 1988.

B. A. Paldus and A. A. Kachanov. An historical overview of cavity-enhanced methods. *Canadian Journal of Physics*, 83(10):975–999, 2005.

J. Paul and R. Saykally. Peer reviewed: Cavity ringdown laser absorption spectroscopy. *Analytical Chemistry*, 69(9):287A–292A, 1997.

J. Pfeiffer, D. Kirsten, P. Kalkert, and W. Urban. Sensitive magnetic rotation spectroscopy of the OH free radical fundamental band with a colour centre laser. *Applied Physics B*, 26(3):173–177, 1981.

E. R. Ritter and J. W. Bozzelli. THERM: Thermodynamic property estimation for gas phase radicals and molecules. *International Journal of Chemical Kinetics*, 23(9):767–778, 1991.

D. Romanini, A. Kachanov, N. Sadeghi, and F. Stoeckel. CW cavity ring down spectroscopy. *Chemical Physics Letters*, 264(3-4):316 – 322, 1997a.

D. Romanini, A. Kachanov, and F. Stoeckel. Diode laser cavity ring down spectroscopy. *Chemical Physics Letters*, 270(5-6):538 – 545, 1997b.

J. Scherer, D. Voelkel, D. Rakestraw, J. Paul, C. Collier, R. Saykally, and A. O'Keefe. Infrared cavity ringdown laser absorption spectroscopy (IR-CRLAS). *Chemical Physics Letters*, 245(2-3):273–280, 1995.

A. Siegman. *Lasers*. University Science Books, 1986. ISBN 9780935702118.

G. P. Smith, D. M. Golden, M. Frenklach, N. W. Moriarty, B. Eiteneer, M. Goldenberg, C. T. Bowman, R. K. Hanson, S. Song, W. C. Gardiner, V. V. Lissianski, and Z. Qin. Gri-mech 3.0, http://www.me.berkeley.edu/gri mech, 2014.

J. Steinfeld. *Molecules and Radiation: An Introduction to Modern Molecular Spectroscopy. Second Edition*. Dover Books on Chemistry. Dover Publications, 2012.

C. A. Taatjes and D. B. Oh. Time-resolved wavelength modulation spectroscopy measurements of HO_2 kinetics. *Appl. Opt.*, 36(24):5817–5821, Aug 1997.

J. Thiébaud and C. Fittschen. Near infrared cw-CRDS coupled to laser photolysis: Spectroscopy and kinetics of the HO_2 radical. *Applied Physics B*, 85(2):383–389, 2006.

J. Thiebaud, S. Crunaire, and C. Fittschen. Measurements of line strengths in the $2\nu_1$ band of the HO_2 radical using laser photolysis/continuous wave cavity ring-down spectroscopy (cw-CRDS). *The Journal of Physical Chemistry A*, 111(30):6959–6966, 2007.

C. Townes and A. Schawlow. *Microwave Spectroscopy*. Dover Books on Physics. Dover Publications, 1955. ISBN 9780486617985.

E. I. A. U.S. Department of Energy. URL `http://www.eia.gov/totalenergy/data/monthly/previous.php#2015`.

O. Votava, M. Masat, A. E. Parker, C. Jain, and C. Fittschen. Microcontroller based resonance tracking unit for time resolved continuous wave cavity-ringdown spectroscopy measurements. *Review of Scientific Instruments*, 83(4):043110, 2012.

J. U. White. Very long optical paths in air. *J. Opt. Soc. Am.*, 66(5):411–416, 1976.

E. K. Wilson. Cavity ringdown offers sensitivity, simplicity in absorption spectroscopy. *Chemical & Engineering News Archive*, 74(8):34–37, 1996.

S. H. Won, B. Jiang, P. Dievart, C. H. Sohn, and Y. Ju. Self-sustaining n-heptane cool diffusion flames activated by ozone. *Proceedings of the Combustion Institute*, 35(1):881 – 888, 2015.

E. C. Wood and J. R. Charest. Chemical Amplification - Cavity Attenuated Phase Shift spectroscopy measurements of atmospheric peroxy radicals. *Analytical Chemistry*, 86(20):10266–10273, 2014.

L. Wu. *Kinetic Studies of Non-equilibrium Plasma-assisted Ignition and Combustion*. PhD thesis, Drexel University, 2013.

L. Wu, J. Lane, N. P. Cernansky, D. L. Miller, A. A. Fridman, and A. Y. Starikovskiy. Plasma enhanced combustion in methane-, ethane-, propane-, and butane-air mixtures below self-ignition threshold. In *2010 Abstracts IEEE International Conference on Plasma Science*, June 2010.

L. Wu, J. Lane, N. Cernansky, D. Miller, A. Fridman, and A. Starikovskiy. Plasma-assisted ignition below self-ignition threshold in methane, ethane, propane and butane-air mixtures. *Proceedings of the Combustion Institute*, 33(2):3219 – 3224, 2011a.

L. Wu, J. Lane, N. Cernansky, D. Miller, A. Fridman, and A. Starikovskiy. Time resolved PLIF and CRD diagnostics of OH radicals in the afterglow of plasma discharge in hydrocarbon mixtures. In *7th US National Combustion Meeting*, 2011b.

L. Wu, J. Lane, M. Stichter, N. Cernansky, D. Miller, and A. Fridman. Effects of N2(v) and NO in plasma-assisted oxidation and ignition below auto-ignition threshold. In *51st AIAA Aerospace Sciences Meeting*, 2013.

J. Zádor, C. A. Taatjes, and R. X. Fernandes. Kinetics of elementary reactions in low-temperature autoignition chemistry. *Progress in Energy and Combustion Science*, 37(4):371 – 421, 2011.

M. S. Zahniser, K. E. McCurdy, and A. C. Stanton. Quantitative spectroscopic studies of the hydroperoxo radical: band strength measurements for the ν_1 and ν_2 vibrational bands. *The Journal of Physical Chemistry*, 93(3):1065–1070, 1989.

P. Zalicki and R. N. Zare. Cavity ring-down spectroscopy for quantitative absorption measurements. *The Journal of Chemical Physics*, 102(7):2708–2717, 1995.

S. J. Zalyubovsky, D. Wang, and T. A. Miller. Observation of the $\widetilde{A} \leftarrow \widetilde{X}$ electronic transition of the CF_3O_2 radical. *Chemical Physics Letters*, 335(3-4):298 – 304, 2001.

S. J. Zalyubovsky, B. G. Glover, T. A. Miller, C. Hayes, J. K. Merle, and C. M. Hadad. Observation of the $\widetilde{A} \leftarrow \widetilde{X}$ electronic transition of the 1-$C_3H_7O_2$ and 2-$C_3H_7O_2$ radicals using cavity ringdown spectroscopy. *The Journal of Physical Chemistry A*, 109(7):1308–1315, 2005.

P. Zeeman. The effect of magnetisation on the nature of light emitted by a substance. *Nature*, 55 (1424):347, 1897.

Appendix A. Codes for FEMM and RTS

A.1 Running FEMM on macOS

FEMM is a Windows program, but can be successfully installed on macOS using the Wine program. At this time, the 32 bit version of FEMM is the only one that works. Navigate to the location where the install file is located. On my machine this is the path `~/.wine/drive_c/`. Upon execution, this file installs the FEMM program executable for FEMM 4.2 to the folder `~/.wine/drive_c/femm42/bin/`.

A.2 Lua code for FEMM modeling of magnetic flux density at magnet distances between 1" and 8" at 0.25" increments

```
--MORFEMM.lua
 --Jeremy Robbins - MEM Senior Design - Magnet Dist/Field calc
 --Mike Stichter - Slot burner calculations

step=0.125;
for n = 0.5,4,step do -- n corresponds to spacing between ring magnets

open ("Dist_null.fem"); -- open blank solution, ABC bound axisymmetric axis half circle, 8" radius

mi_saveas("dist_"..(n*200)
..".FEM");
--Create "top" magnet
--Add nodes
mi_addnode(0.125,n);
```

```
mi_addnode(0.125,n+2);
mi_addnode(1,n+2);
mi_addnode(1,n);

--connect nodes with segments
mi_addsegment(0.125,n,0.125,n+2);
mi_addsegment(0.125,n+2,1,n+2);
mi_addsegment(1,n+2,1,n);
mi_addsegment(1,n,0.125,n);

--define material
mi_addblocklabel(0.5,n+0.5)
mi_selectlabel(0.5,n+0.5)
mi_setblockprop("N42",1,0,0,90,0,0)

--Create "bottom" magnet, same process as top magnet
mi_addnode(0.125,-n);
mi_addnode(0.125,-(n+2));
mi_addnode(1,-(n+2));
mi_addnode(1,-n);

mi_addsegment(0.125,-n,0.125,-(n+2));
mi_addsegment(0.125,-(n+2),1,-(n+2));
mi_addsegment(1,-(n+2),1,-n);
mi_addsegment(1,-n,0.125,-n);

mi_addblocklabel(0.5,-(n+0.5));
mi_selectlabel(0.5,-(n+0.5));
```

```
43 mi_setblockprop("N42",1,0,0,90,0,0);
44
45 mi_analyze();
46 mi_loadsolution();
47 mi_saveas("dist_"..(n*200)..".FEM");
48
49 --mo showdensityplot(legend,gscale,upper_B,lower_B,type)
50 mo_showdensityplot(1,0,0,1,"bmag");
51 --mo zoom(x1,y1,x2,y2) Zoom to the window defined by lower left
    ↪ corner (x1,y1) and upper right corner (x2,y2).
52 mo_savebitmap("dist_"..(n*200)..".bmp");
53 mo_seteditmode(contour);
54 mo_addcontour(0,.5);
55 mo_addcontour(0,-.5);
56 --mo_makeplot(PlotType,NumPoints,Filename,FileFormat)
57 mo_makeplot(1,100,"dist_"..(n*200)..".txt",0)
58 mo_close()
59 mi_close()
60 end
```

A.3 MATLAB script to import and plot raw magnetic flux across sample area

```
%% Jeremy Robbins - Autoimport & plot raw XY field strength
clear
clc

%% Read data
ref=[100:25:800];

B=zeros(100,30);
plotname = zeros(1,29);

B(:,1)= dlmread('dist_100.txt','\t',[2 0 101 0]);
B(:,1)=B(:,1)-.5;       %center plot at sample

for i = 1:29

filename = strcat('dist_',num2str(ref(i)),'.txt');
plotname(i) = ref(i)/100;

B(:,i+1)= dlmread(filename,'\t',[2 1 101 1]);
end

%% Plot raw data together

figure;
plot(B(:,1),B(:,2:29))

% Add title and axis labels
```

```
28 xlabel('Distance from sample center');
29 ylabel('Magnetic Flux Density (T)');
30 title ('Sample Magnetic Flux Density at Varying Magnet
    ↪ Distance');
31 legend(strcat(num2str(plotname(:)),'"'));
```

A.4 MATLAB script to calculate and plot N42 magnetic flux average across 1 system sample interaction pathway

```
%% Jeremy Robbins - Autoimport & plot avg XY field strength
clear
clc

%% Read data
ref=[100:25:800];

B=zeros(100,30);
dist = zeros(1,29);

B(:,1)= dlmread('dist_100.txt','\t',[2 0 101 0]);
B(:,1)=B(:,1)-.5;       %center plot at sample

for i = 1:29

filename = strcat('dist_',num2str(ref(i)),'.txt');
dist(i) = ref(i)/100;

B(:,i+1)= dlmread(filename,'\t',[2 1 101 1]);
end

%% Find averages
sampleavg = mean(B(31:70,2:30));

%% Plot data
figure;
```

```
27 plot(dist(:),sampleavg)
28
29 % Add title and axis labels
30 xlabel('Magnet Seperation (in)');
31 ylabel('Average Magnetic Flux Density (T)');
32 title ('Average Magnetic Flux Density Across Sample at Varying
    ↪ Magnet Distance');
```

A.5 Script to control Resonance Tracking System

A.5.1 Full FSR Sweep RTS Program

The RTS_Long_Sweep Arduino

```
/*
 * RTS_Full
 * Scans length of TPA (Tubular PZT Actuator).
 * Written by Jeremy Robbins, Ilya Semenov, and Mike Stichter
*/


// defines for setting and clearing register bits
// Necessary for fast pin modification, DO NOT USE digitalWrite() or analogWrite()
#ifndef cbi
#define cbi(sfr, bit) (_SFR_BYTE(sfr) &= ~_BV(bit))
#endif
#ifndef sbi
#define sbi(sfr, bit) (_SFR_BYTE(sfr) |= _BV(bit))
#endif



// Set global variables
int U_PZT = 0; //PZT voltage variable
const int U_MAX = 750; //Max PZT scan limit ----------------------Do not set higher than 800, issues occur
const int U_MIN = 50; //Minimum PZT scan limit -------------------Do not set lower than 10, issues occur
```

```
22
23
24
25 void setup() {
26 // Setup code runs once prior to FULL SWEEP MODE loop or
    ↪ TRACKING MODE loop.
27
28
29
30 //Speeds up microprocessor sample rate at the expense of
    ↪ accuracy
31 //Modifies the Prescale factor to 32, this sets the clock
    ↪ frequency to .5 MHz and sampling rate to 38.4 KHz
32   sbi(ADCSRA,ADPS2) ; //1 * (16) *
33   cbi(ADCSRA,ADPS1) ; //0 * (4)  *
34   sbi(ADCSRA,ADPS0) ; //1 * (2)  =16*2=32
35 // Do not modify without referncing
    ↪ http://yaab-arduino.blogspot.com/2015/02/fast-sampling-from-analog-input.
36
37
38
39   //Configure Pins
40   pinMode(A3, INPUT); //PZT Sense IN
41   pinMode(A4, INPUT); // CRDS event IN
42   pinMode(7, OUTPUT); //Ramp Control OUT
43
44   //Start Initial Sweep up
45   PORTD &= ~_BV(PD7); //set pzt wave to high, pin to low
```

```
46
47  }
48
49
50  //FULL SWEEP MODE
51  void loop() { //Loop to run code repeatedly
52
53    U_PZT = analogRead(A3); //Reads current value of PZT input
54
55    if (U_PZT > U_MAX) {  //if current value is over maximum limit
56
57      PORTD |= _BV(PD7); //sets pzt wave to low, pin to high
58    }
59
60    if  (U_PZT < U_MIN) {  //if current value is less than minimum
      ↪ limit
61
62      PORTD &= ~_BV(PD7); //set pzt wave to high, pin to low
63    }
64
65  }
66  //Full sweep mode reverses the direction of the PZT wave if it
      ↪ goes out of the lower and upper bounds set as global
      ↪ variables
67
68
69
```

```
70 /* Block comment start, (remove to activate mode, comment out
    ↪ Tracking Mode loop() in the same way before running
    ↪ uploading)
71
72
73 ////TRACKING MODE
74 void loop() { //Loop to run code repeatedly
75
76
77
78 //Reads CRDS event input and triggers change in direction of PZT
    ↪ wave when past the threshold set physically
79  if(analogRead(A4) > 700){  //DO NOT MODIFY 700 Threshold, this
    ↪ is done physically, the CRDS event signal does not depend on
    ↪ actual threshold level
80      delayMicroseconds(500); //CHANGE TO SLIGHTLY LONGER THAN
    ↪ AOM OUT WIDTH
81      PORTD ^= (_BV(PD7)); //Toggle PZT pin
82
83  }
84
85  else if(analogRead(A3) > U_MAX){ // If current PZT value
    ↪ higher than upper bound
86      PORTD |= _BV(PD7); //sets pzt wave to low, pin to high
87
88
89      //Reset to middle
```

```
90        while(analogRead(A3)>400){ //While PZT value is in upper
    ↪  half
91          delayMicroseconds(50); //Delay
92        }
93
94
95        }
96     else if(analogRead(A3) < U_MIN){ // If current PZT value lower
    ↪  than lower bound
97        PORTD &= ~_BV(PD7); //set pzt wave to high, pin to low
98
99
100       //Reset to middle
101       while(analogRead(A3)<400){ //While PZT value is in lower
    ↪  half
102         delayMicroseconds(50);  //Delay
103       }
104       }
105
106
107    }
108
109
110 */ //End block comment
111
112
```

A.5.2 Resonance Tracking Mode RTS Program

The RTS_Tracking Arduino program.

```
/*
 * RTS_Full
 * Scans length of TPA (Tubular PZT Actuator).
 * Written by Jeremy Robbins, Ilya Semenov, and Mike Stichter
*/

// defines for setting and clearing register bits
// Necessary for fast pin modification, DO NOT USE digitalWrite() or analogWrite()
#ifndef cbi
#define cbi(sfr, bit) (_SFR_BYTE(sfr) &= ~_BV(bit))
#endif
#ifndef sbi
#define sbi(sfr, bit) (_SFR_BYTE(sfr) |= _BV(bit))
#endif



// Set global variables
int U_PZT = 0; //PZT voltage variable
const int U_MAX = 750; //Max PZT scan limit ----------------------Do not set higher than 800, issues occur
const int U_MIN = 50; //Minimum PZT scan limit -------------------Do not set lower than 10, issues occur

```

```
23
24
25 void setup() {
26 // Setup code runs once prior to FULL SWEEP MODE loop or
    ↪ TRACKING MODE loop.
27
28
29
30 //Speeds up microprocessor sample rate at the expense of
    ↪ accuracy
31 //Modifies the Prescale factor to 32, this sets the clock
    ↪ frequency to .5 MHz and sampling rate to 38.4 KHz
32   sbi(ADCSRA,ADPS2) ; //1 * (16) *
33   cbi(ADCSRA,ADPS1) ; //0 * (4)  *
34   sbi(ADCSRA,ADPS0) ; //1 * (2)  =16*2=32
35 // Do not modify without referncing
    ↪ http://yaab-arduino.blogspot.com/2015/02/fast-sampling-from-analog-input.
36
37
38
39   //Configure Pins
40   pinMode(A3, INPUT); //PZT Sense IN
41   pinMode(A4, INPUT); // CRDS event IN
42   pinMode(7, OUTPUT); //Ramp Control OUT
43
44   //Start Initial Sweep up
45   PORTD &= ~_BV(PD7); //set pzt wave to high, pin to low
46
```

```
47 }
48
49
50
51 /* Block comment start, (remove to activate mode, comment out
    ↪ Tracking Mode loop() in the same way before running
    ↪ uploading)
52
53
54 //FULL SWEEP MODE
55 void loop() { //Loop to run code repeatedly
56
57   U_PZT = analogRead(A3); //Reads current value of PZT input
58
59   if (U_PZT > U_MAX) {  //if current value is over maximum limit
60
61     PORTD |= _BV(PD7); //sets pzt wave to low, pin to high
62   }
63
64   if  (U_PZT < U_MIN) {  //if current value is less than minimum
    ↪ limit
65
66     PORTD &= ~_BV(PD7); //set pzt wave to high, pin to low
67   }
68
69 }
```

```
70 //Full sweep mode reverses the direction of the PZT wave if it goes out of the lower and upper bounds set as global variables
71
72 */ //End block comment
73
74
75
76 ////TRACKING MODE
77 void loop() { //Loop to run code repeatedly
78
79
80
81 //Reads CRDS event input and triggers change in direction of PZT wave when past the threshold set physically
82   if(analogRead(A4) > 700){  //DO NOT MODIFY 700 Threshold, this is done physically, the CRDS event signal does not depend on actual threshold level
83       delayMicroseconds(500); //CHANGE TO SLIGHTLY LONGER THAN AOM OUT WIDTH
84       PORTD ^= (_BV(PD7)); //Toggle PZT pin
85
86   }
87
88   else if(analogRead(A3) > U_MAX){ // If current PZT value higher than upper bound
89       PORTD |= _BV(PD7); //sets pzt wave to low, pin to high
90
```

```
91
92        //Reset to middle
93        while(analogRead(A3)>400){ //While PZT value is in upper
           ↪ half
94          delayMicroseconds(50); //Delay
95        }
96
97
98        }
99    else if(analogRead(A3) < U_MIN){ // If current PZT value lower
       ↪ than lower bound
100       PORTD &= ~_BV(PD7); //set pzt wave to high, pin to low
101
102
103       //Reset to middle
104       while(analogRead(A3)<400){ //While PZT value is in lower
           ↪ half
105         delayMicroseconds(50);  //Delay
106       }
107       }
108
109
110   }
111
112
113
114
```

A.6 Code for temperature, humidity, and vibration monitoring and upload to Google Drive

This code is designed to read the vibrations of the laser optical table so monitors at a high rate and is not suitable for long term testing.

```
#!/usr/bin/env python
#HIH8xxx_read_store.py
#Jeremy Robbins 9/24/14 (HIH8xxx_read and main)
#adapted from
 ↪ http://www.raspberrypi.org/forums/viewtopic.php?f=32&t=29454
#Andy Gnias 7/23/15 (MPU6050read and Google Drive file upload)
#Accelerometer code adapted from:
#http://blog.bitify.co.uk/2013/11/reading-data-from-mpu-6050-on-raspberry.htm
#Google Drive code adapted from:
#https://raspberrypi.org/forums/viewtopic.php?f=43&t=111618
#https://pypi.python.org/pypi/PyDrive

#For Google Drive Usage
from pydrive.auth import GoogleAuth
from pydrive.drive import GoogleDrive

#for HIH & MPU
import smbus
import collections

#for main()
import os
import glob
import gspread
import sys
```

```
25 from datetime import datetime, date
26
27 def file_version(path, filename) :
28         """Sets version number of file, allowing for multiple
           ↪ log files to be
29         created in a day."""
30         date = datetime.now()
31         version = 2
32         vstring = str(version)
33         while os.path.isfile(filename) == True: #creates new
           ↪ version of file if one exists for specific day
34                 filename = 'accel_data_%s_V%s'
                   ↪ %(date.strftime("%m_%d_%y"),vstring)
35                 filename = os.path.join(path, filename)
36                 version += 1
37                 vstring = str(version)
38         return filename
39
40 def HIH8xxx_read():
41      d = []
42      bus.write_quick(addr)
43      d = bus.read_i2c_block_data(addr, 0)
44      status = (d[0] & 0xc0) >> 6
45      humidity = (((d[0] & 0x3f) << 8) + d[1])*100/16383
46      tempC = ((d[2] << 6) + ((d[3] & 0xfc) >> 2))*165/16383 - 40
47      tempF = tempC*9/5 + 32
48
49      #Print values
```

```
50      #stamp1 = datetime.now()
51      #print stamp1
52      #print "Humidity:    ", humidity, "%", " Temperature: ",
         ↪  tempF, "F"
53
54      #named tuples witchcraft
55      data = collections.namedtuple('reading',['h','t'])
56      data_ = data(humidity, t=tempF)
57      return data_
58
59  #Needed for MPU code
60  def read_byte(adr):
61      return bus.read_byte_data(address, adr)
62
63  #Needed for MPU code
64  def read_word(adr):
65      high = bus.read_byte_data(address, adr)
66      low = bus.read_byte_data(address, adr+1)
67      val = (high << 8) + low
68      return val
69
70          #Needed for MPU code
71  def read_word_2c(adr):
72      val = read_word(adr)
73      if (val >= 0x8000):
74          return -((65535 - val) + 1)
75      else:
76          return val
```

```
77
78 #Accelerometer readout
79 def MPU6050read_zaxis():
80         bus.write_byte_data(address, 0x6b, 0) #wakes up
            ↪ accelerometer from sleep mode
81         accel_zout_raw = read_word_2c(0x3f) #reads acceleration
            ↪ in z direction
82         accel_zout = accel_zout_raw / 16384.0 #scale factor from
            ↪ product spec manual (p.16)
83         return accel_zout
84
85 def main():
86         """Creates a file to store acceleration data. Records
            ↪ initial temp and
87         humidity once. Uploads data to Google Drive folder."""
88         start = datetime.now() #switched from date to datetime -
            ↪ second delta
89         filename = 'accel_data_%s'%start.strftime("%m_%d_%y")
90         path = '/home/pi/lab/Acceleration_data'
91         filename = os.path.join(path,filename)
92         filename = file_version(path, filename)
93         #Creates filename for Google Drive folder
94         path_length = len(path) + 1
95         filename_gd = filename[path_length:]
96
97         #Google Drive Authorization
98         #will load login credentials so long as they already
            ↪ exist
```

```
99          #If not, will prompt for new information
100         gauth = GoogleAuth()
101         gauth.LoadCredentialsFile("pydrive_auth.txt")
102         if gauth.credentials is None:
103                 gauth.CommandLineAuth()
104         elif gauth.access_token_expired:
105                 gauth.Refresh()
106         else:
107                 gauth.Authorize()
108         gauth.SaveCredentialsFile("pydrive_auth.txt")
109         drive = GoogleDrive(gauth)
110         print "Google Drive authorization complete"
111
112         #Create Google Drive File
113         #ID is specific folder ID from the folder URL
114         file1 = drive.CreateFile({'title': '%s'%filename_gd,
115                         'mimeType':'text/csv',
116                         "parents": [{"kind":
                             ↪ "drive#fileLink","id":
117                         "0B_4L7SWIO7v2fkFRRGlMX05YTm9rVkRna3dJZFlUaDNWUGN1WHF
118
119         #File header
120         title = ['Timestamp', 'Z-Acceleration', 'Humidity',
             ↪ 'Temperature', ]
121
122         with open(filename, 'a') as f:
123                 f.write( ", ".join( repr(e) for e in title ) )
124                 f.write('\n')
```

```
125                 #Write Temp and Humidity data with initial date
                     ↪ and time
126                 stamp = datetime.now().strftime('%Y-%m-%d
                     ↪ %H:%M:%S.%f')
127                 atm_read = HIH8xxx_read()
128                 values = [stamp, 0, 0, 0, atm_read.h,
                     ↪ atm_read.t]
129                 f.write( ", ".join( repr(e) for e in values ) )
                     ↪ #writes data without brackets
130                 f.write('\n')
131
132                 #set while loop to run
133                 print "Reading Acceleration Data. Press Ctrl-C
                     ↪ to quit."
134                 accel_epoch = datetime.now()
135                 #Performs while loop until broken with keyboard
                     ↪ interrupt
136                 try :
137                         while True: #infinite loop
138                                 read_time=
                                     ↪ datetime.now().strftime('%Y-%m-%d
                                     ↪ %H:%M:%S.%f')
139                                 accel_read = MPU6050read_zaxis()
140                                 read_time = datetime.now() -
                                     ↪ accel_epoch
```

```
141                                 read_time =
                                     ↪ (read_time.microseconds *
                                     ↪ 0.000001) +
                                     ↪ read_time.seconds
142                                 string_seconds =
                                     ↪ round(read_time,4)
143                                 values = [string_seconds,
                                     ↪ round(accel_read,6)]
144                                 f.write( ", ".join( repr(e) for
                                     ↪ e in values ) ) #writes data
                                     ↪ without brackets
145                                 f.write('\n')
146                                 f.flush()
147
148                         except KeyboardInterrupt :
149                                 print '\n'
150                                 f.close()
151                                 with open(filename, 'r') as f : s =
                                     ↪ f.read()
152                                 f.close()
153                                 file1.SetContentString(s) #uploads
                                     ↪ contents of current text file
154                                 file1.Upload() #uploads to Google Drive
155                                 print "File upload to Google Drive
                                     ↪ complete"
156
157 #Globals used for reading from sensors
158 bus = smbus.SMBus(1) #value of 1 used for Rev2 of pi
```

```
159 addr = 0x27 #from i2cdetect, address of the humidity / temp
     ↪ sensor
160 address = 0x68 #also from i2cdetect, address of the MPU
     ↪ accelerometer
161
162 main()
```

A.7 Code for temperature and humidity monitoring

This code is designed to read the temperature and humidity at 30 minute intervals for trending.

```
#!/usr/bin/env python
#HIH8xxx_read_store.py
#Jeremy Robbins 9/24/14 (HIH8xxx_read and main)
#adapted from
 ↪ http://www.raspberrypi.org/forums/viewtopic.php?f=32&t=29454
#Andy Gnias 7/23/15 (MPU6050read and Google Drive file upload)
#Accelerometer code adapted from:
#http://blog.bitify.co.uk/2013/11/reading-data-from-mpu-6050-on-raspberry.htm
#Google Drive code adapted from:
#https://raspberrypi.org/forums/viewtopic.php?f=43&t=111618
#https://pypi.python.org/pypi/PyDrive
#Mike Stichter 6/10/2016
#modified OLab_accelcode.py by Andy Gnias for only Temp Humid
 ↪ and upload to google drive

#For Google Drive Usage
import time
from pydrive.auth import GoogleAuth
from pydrive.drive import GoogleDrive

#for HIH & MPU
import smbus
import collections

#for main()
import os
```

```
25 import glob
26 import gspread
27 import sys
28 from datetime import datetime, date
29
30 def file_version(path, filename) :
31         """Sets version number of file, allowing for multiple
           ↪ log files to be
32         created in a day."""
33         date = datetime.now()
34         version = 2
35         vstring = str(version)
36         #new version of file created if one exists for specific
           ↪ day
37         while os.path.isfile(filename) == True :
38                 filename = 'OLab_Temp_Humid_data_%s_v%s'
                   ↪ %(date.strftime("%m_%d_%y"),vstring)
39                 filename = os.path.join(path, filename)
40                 version += 1
41                 vstring = str(version)
42         return filename
43
44 def HIH8xxx_read():
45         """Returns tuple of humidity and temperature data from
           ↪ HIH8xxx
46         sensor."""
47         d = []
48         bus.write_quick(addr_HIH)
```

```
49          d = bus.read_i2c_block_data(addr_HIH, 0)
50          status = (d[0] & 0xc0) >> 6
51          humidity = (((d[0] & 0x3f) << 8) + d[1])*100/16383
52          tempC = ((d[2] << 6) + ((d[3] & 0xfc) >> 2))*165/16383 -
             ↪ 40
53          tempF = tempC*9/5 + 32
54
55          # Print values
56          stamp1 = datetime.now()
57          print stamp1
58          print "Humidity:    ", humidity, "%", " Temperature: ",
             ↪ tempF, "F"
59
60          data = collections.namedtuple('reading',['h','t'])
61          data_ = data(humidity, t=tempF)
62          return data_
63
64  #Globals used for reading from sensors
65  bus = smbus.SMBus(1) #value of 1 used for Rev2 of pi
66  addr_HIH = 0x27 #from i2cdetect, address of the humidity / temp
     ↪ sensor
67  addr_MPU = 0x68 #also from i2cdetect, address of the MPU
     ↪ accelerometer
68
69  #Google Drive Authorization
70  #will load login credentials so long as they already exist
71  #If not, will prompt for new information
72  gauth = GoogleAuth()
```

```
gauth.LoadCredentialsFile("pydrive_auth.txt")
if gauth.credentials is None:
        gauth.CommandLineAuth()
elif gauth.access_token_expired:
        gauth.Refresh()
else:
        gauth.Authorize()
gauth.SaveCredentialsFile("pydrive_auth.txt")
drive = GoogleDrive(gauth)
print "Google Drive Authorization Complete"

#Create Google Drive File
start = datetime.now()
file1 = drive.CreateFile({'title':
 ↪  'olabatm_cond_%s.csv'%start.strftime("%m_%d_%y"),
                'mimeType':'text/csv',
                "parents": [{"kind": "drive#fileLink","id":
                "0B_4L7SWIO7v2fkFRRGlMX05YTm9rVkRna3dJZFlUaDNWUGN1WHRIZFJlQjN
#ID is specific folder ID from the folder URL

##Old HIH def
# def HIH8xxx_read():
#       d = []
#       bus.write_quick(addr)
#       time.sleep(0.050)
#       d = bus.read_i2c_block_data(addr, 0)
#       status = (d[0] & 0xc0) >> 6
#       humidity = (((d[0] & 0x3f) << 8) + d[1])*100/16383
```

```
100 #       tempC = ((d[2] << 6) + ((d[3] & 0xfc) >> 2))*165/16383 -
     ↪ 40
101 #       tempF = tempC*9/5 + 32
102 
103 #       #Print values
104 #       stamp1 = datetime.now()
105 #       print stamp1
106 #       print "Humidity:    ", humidity, "%", " Temperature: ",
     ↪ tempF, "F"
107 #       #named tuples witchcraft
108 #       data = collections.namedtuple('reading',['h','t'])
109 #       dat = data(humidity, t=tempF)
110 #       return dat
111 
112 
113 def main():
114         #Purpose of module is to create a new log file everyday
             ↪ and log the temp and
115         #humidity at the defined interval. Each file to be named
             ↪ after the date created
116 
117         #define recording interval (sec)
118         interval = 30
119 
120         start = datetime.now()
121         #Create new file for date
122         filename =
             ↪ 'olabatm_cond_%s.txt'%start.strftime("%m_%d_%y")
```

```
123         version = 2
124         vstring = str(version)
125         title = ['Timestamp', 'Humidity', 'Temperature', ]
126         with open(filename, "a") as f:
127                 f.write( ", ".join( repr(e) for e in title ) )
128                 f.write('\n')
129                 f.flush()
130                 os.fsync(f.fileno())
131         #set while loop to run
132         while True: #infinite loop
133           tdelta = 0
134           while tdelta < 86400:
135                 #for x in xrange(10): #non infinite test loop
136                         # tdelta%600 == 0: #uploads data to
                          ↪ Google Drive every 600 seconds (5
                          ↪ minutes)
137                                 stamp =
                                  ↪ datetime.now().strftime('%Y-%m-%d
                                  ↪ %H:%M:%S.%f')
138                                 new = HIH8xxx_read()
139                                 #newer = MPU6050read()
140                                 values = [stamp, new.h, new.t]
141                                 with open(filename, "a") as f:
                                  ↪ #appends data to text file
142                                         #Note: will add to
                                           ↪ existing file of the
                                           ↪ same date if one
                                           ↪ already exists
```

```
143                                     f.write( ", ".join(
                                         ↪ repr(e) for e in
                                         ↪ values ) ) #writes
                                         ↪ data without
                                         ↪ brackets
144                                     f.write('\n')
145                                     f.flush()
146                                     os.fsync(f.fileno())
147                                     now = datetime.now()
148                                     tdelta_temp = now -
                                         ↪ start
149                                     tdelta =
                                         ↪ tdelta_temp.seconds
150                                 print "tdelta", tdelta #print
                                     ↪ for ts
151         #                           f.close()
152                                 with file(filename) as f: s =
                                     ↪ f.read() #variable for text
                                     ↪ file contents
153                                 file1.SetContentString(s)
                                     ↪ #uploads contents of current
                                     ↪ text file
154                                 file1.Upload() #uploads to
                                     ↪ Google Drive
155                     #Note: will add to existing file of the same
                         ↪ date if one already exists
```

```
156                                 f.write( ", ".join( repr(e) for
                                     ↪ e in values ) ) #writes data
                                     ↪ without brackets
157                                 f.write('\n')
158                                 f.flush()
159                                 os.fsync(f.fileno())
160                                 now = datetime.now()
161                                 tdelta_temp = now - start
162                                 tdelta = tdelta_temp.seconds
163                                 print "tdelta", tdelta #print
                                     ↪ for ts
164 main()
```

Appendix B. Technical Drawings

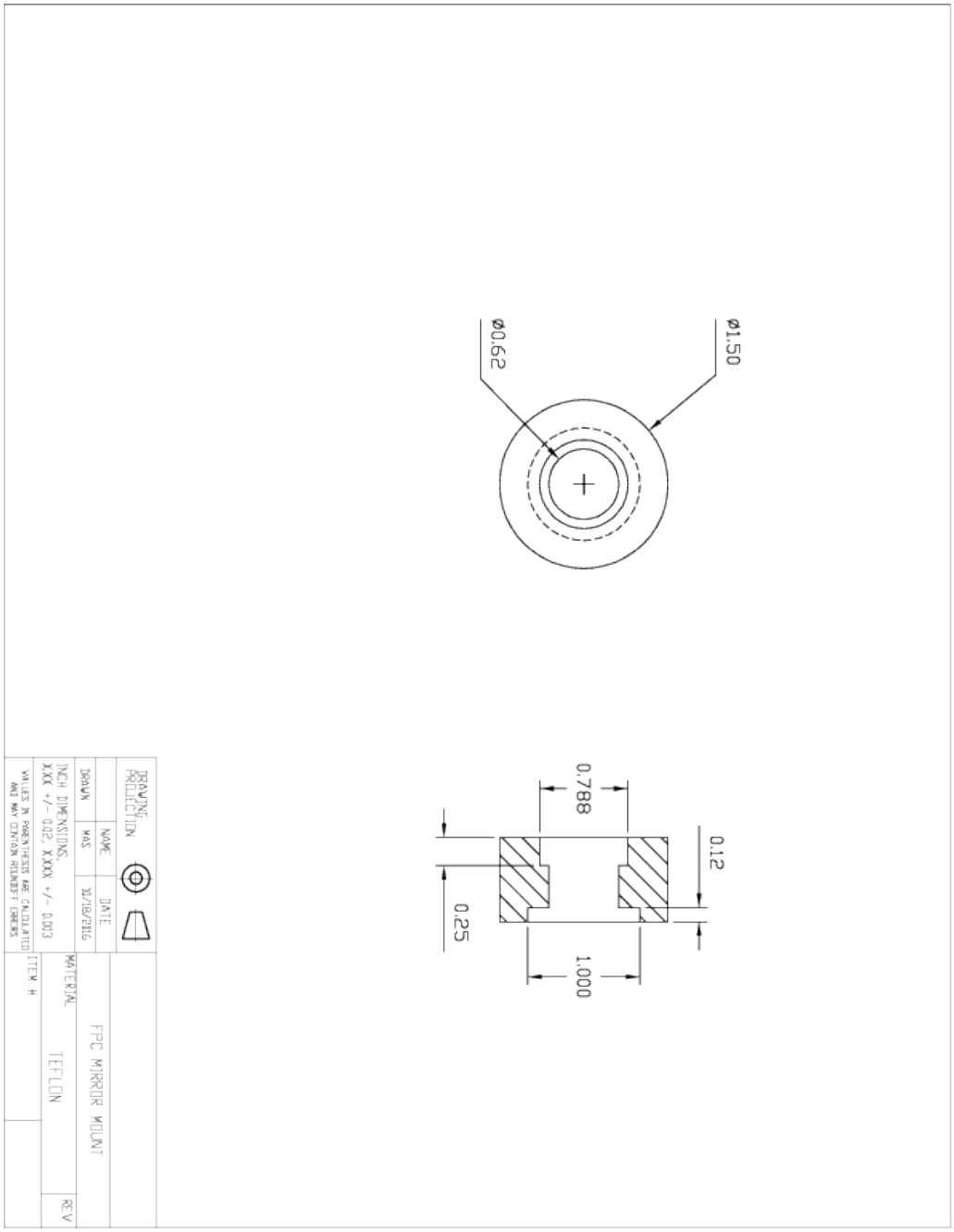

Figure B.1: Adapter to attach TPA to kinematic mirror mount.

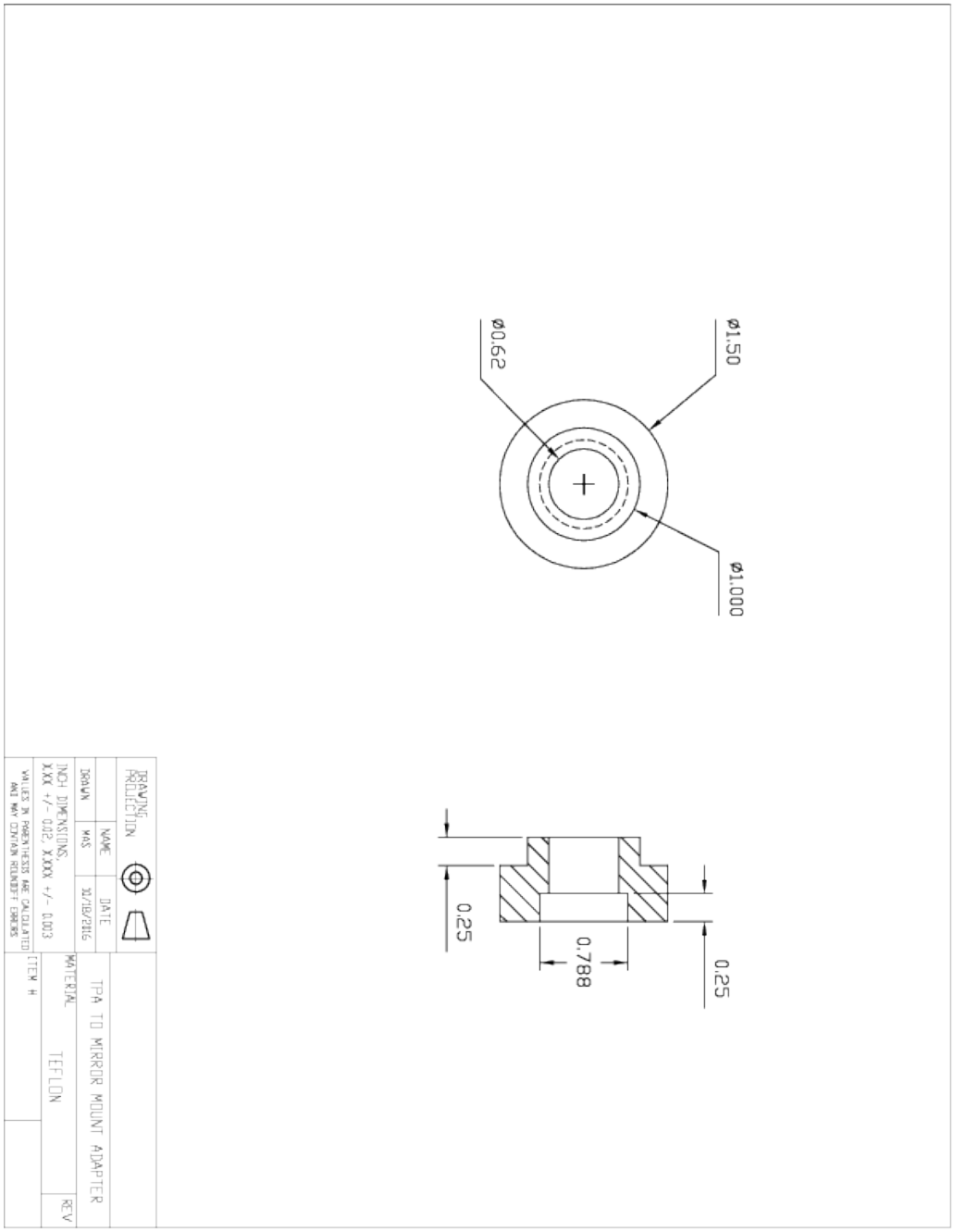

Figure B.2: Adapter to attach CRD mirror to TPA.

Appendix C. Nd:YAG Facility Upgrades, Maintenance, and Troubleshooting

During the course of the experimental campaign utilizing the Nd:YAG laser many upgrades were made, and maintenance and troubleshooting tasks were performed

C.1 Curtain and frame enclosure

Air currents within the lab due to location and pressure differences of air sources and exhausts caused delays to experimentation. These challenges include stabilizing the flame of the slot burner, significant dust collection on all surfaces in the lab during construction near the lab, and large swings in relative humidity which cause problems with laser components and absorption of laser at certain wavelengths. One example of these challenges is that one of the HVAC air supplies to the lab shuts off at 6 PM each day.

C.2 Senior Design - Laser enclosure

A senior design team designed and built a custom environmental enclosure for the Nd:YAG and Dye Lasers. The system was not installed before the lab move. It was moved to the new lab, but has still not been setup. Complete instructions for setup are located in the lab.

The objective of their project was to design, and fabricate an environmental enclosure which maintains temperature and humidity levels within tolerance, while allowing access for adjustments and interfacing with the balance of the laser diagnostic system. A steel structure enclosed with PVC vinyl was fabricated to surround the laser table.

C.3 Lab move

The Optical Diagnostics Lab was shutdown in the Hess building in June of 2013. The laboratory equipment was put into storage until October of 2013, at which time we were first able to move a select few items into the new laboratory space at One Drexel Plaza. Construction of the laboratory space continued through May of 2014, and operational approval was granted in August of 2014.

The building renovation is still a construction zone as of November 2016 where power is unreliable and dust is continually being generated and transfered to the lab.

C.4 Nd:YAG system recommissioning

The Precision 9010 Nd:YAG laser system broke in various ways since setup in One Drexel Plaza Room 276. In March of 2014, we had a factory service person visit to setup the laser in the new lab.

C.4.1 Upgrade Memory in Continuum Laser computer

During the laser system setup service call, Cliff Holt suggested that we upgrade the memory in the computer. We installed the maximum allowed in the system, 2 x 128MB EDO MEMORY NON-PARITY 60NS SIMM 72-PIN 5V 32X32 from newegg.com.

C.4.2 Timing board

In November 2014, the electronic board, Part number 617-9900 which controls the timing of q-switch failed and caused a delay of six weeks to repair.

C.4.3 Seed laser return for replacement

In May of 2015, the seed laser failed to lock to the oscillator cavity and was sent back to the manufacturer for repair along with the PZT controlled by the seed laser. This put the laser out of commission until August 2015. Upon return of the seed laser, the PZT and seed laser were reinstalled in the laser system.

C.4.4 Marx Bank

In January 2016, the Marx bank board and its power supply failed. Precision 9010 - Part numbers 504-3200, PCB PS 750 V ASSY; and 504-3100, PCB Marx Bank HV Assy were installed.

C.4.5 Vibration Isolation and Monitoring

In order to mitigate problems with vibrations caused by external sources, a set of controllers were added to the legs of the optical bench used for MOR, CRDS, and CEMOR slot burner experiments. The table is a 4' x 8' x 12" sealed breadboard top with (Newport XL-A model) vibration isolation legs. An XLPV-KT leveling valve kit was ordered and installed.

An open frame Raspberry Pi model B+ microcomputer was used (700 MHz, 512 Mb RAM) and ordered from Allied Electronics.

A 3 axis accelerometer, part number MMA8451QR1CT-ND, ordered from Digikey. This sensor was found to not work well with the Raspberry Pi, and we discovered that other users were encountering the same problems. An accelerometer was ordered that works better: Adafruit Triple-Axis Accelerometer - MMA8451.

C.5 Humidity and Temperature Monitoring

A humidity and temperature recording system was designed and implimented to monitor the environmental conditions in the new laboratory space. Temperature and humidity changes were felt by laboratory researchers and instability of the laser system prompted further investigation.

The humidity and temperature sensor was part number 480-5706-1-ND, with description: SENSOR HUMIDIDTY 5.5V 2.0% SIP, ordered from Digiky. This sensor interfaced by I2C to the laboratory's Raspberry Pi B+, and results were uploaded for collection and analysis on the web. The Python software code for monitoring temperature, humidity, and vertical acceleration is included in Section A.6.

C.6 Narrow linewidth laser options

While designing the cw-CRDS/CEMOR system, we received indication that Newport NewFocus Venturri TLB-6600 laser was not currently available in the wavelength range that we needed (approx 1430 cm^{-1}) due to the laser diode not being available. No time frame was provided from Newport on the future availability of this laser system. They did find another laser in their lab that turned out to be running with multiple modes so they were unable to supply it to us. They do have

similar lasers available in other wavelengths. As of October 2016, the wavelength range that we need is still not available in this laser although they do have a similar laser, TLB-6726, advertised that would work.

We investigated options with Continuum Lasers as to what could be done to modify the (Precision 9010) Nd:YAG laser system that is currently installed at Drexel University's Optical Diagnostics lab. They suggested that we install an etalon in order to reduce the linewidth. The etalon would also limit the tuning range to approximately 1 cm^{-1}. A new grating that produces a narrower linewidth should allow tuning the laser in the same way that the grating does, however, as the linewidth narrows the power output decreases. We are only interested in the idler beam and do not have to pump the doubler so this shouldn't be a problem. We only need a few mW of power for CRDS/CEMOR experiments. We have an etalon option on the Lamda-Physik dye laser that decreases the linewidth from approximately 0.1 cm^{-1} to 0.03 cm^{-1} and allows tuning over a 1 cm^{-1} bandwidth. This possibility should be pursued further. A grating change in the OPO would be an easy option and probably cost effective. This option will allow use of the LabView programs developed for MOR/CEMOR in the photolysis cell experiments as well.

I had a conversation with Continuum about a way to optimize the the Sunlite OPO linewidth for IR. After discussing the what it is that we are trying to do, they gave me a few suggestions. We discussed the Mirage, and they explained that it was a coffin size piece of equipment that they made about 15 years ago. The software was inadequate for the scanning which it was advertised to do. It worked well at one wavelength, but it did not scan well. Continuum opted not to sink R&D funding into upgrading the software.

Continuum asked if we had ever measured the linewidth. I said that I hadn't, to which he responded that likely the linewidth is better than the 0.08 cm^{-1} that is quoted (when at 550nm signal), and that they use a piece of equipment at the shop which takes a 100 shot average and uses that and some black magic to determine the linewidth.

In June 2011, at the time of a periodic realignment of the oscillator cavity in the Nd:YAG laser, we had decided to replace the flashlamps which where also due for replacement. One of the spares had a manufacturing defect which prevented proper fitment into the laser head. A replacement flashlamp was ordered and installed two weeks later.

Vita

Born in McPherson, Kansas, Michael Stichter grew up in Lebanon, Pennsylvania, where he graduated from Cedar Crest High School. His interest in automobiles, especially antiques, inspired him to start his post-secondary education at McPherson College, in McPherson, KS, where he earned an Associate of Technology degree in Automotive Restoration Technology. This program included heavy lab components in mechanical, body/paint, and trim restoration of antique and classic vehicles. Michael applied this hands-on experience to further education, starting a degree in mechanical engineering at Drexel University. While pursuing his BSME degree, he gained experience in another passion, aerospace. He participated in cooperative education assignments in manufacture of jet engines at Pratt & Whitney; aerospace PEM fuel cell product development and testing at Teledyne Energy Systems; and, at General Electric - Ceramic Composite Products, manufacturing engineering of Carbon-Silicon Carbide (C/SiC) composite parts for on-orbit repair of the Wing Leading Edge and Chin section of the Space Shuttle Orbiter.

After earning his BSME, Michael went to work at Teledyne Energy Systems where he continued working on development projects for aerospace H_2/O_2 PEM fuel cells. He developed systems for micro- and lunar-gravity passive reactant recirculation and water separation, and controls for the fuel cell system. He also engineered, commissioned, and repaired hydrogen (and sometimes oxygen) generation plants at several sites around the world. These systems included the hydrogen electrolyzers, compressors, storage tanks, cooling water, and interconnecting piping.

An opportunity was presented for Michael to return to Drexel to do research with Profs. Cernansky and Miller in their Combustion Chemistry group. While there, Michael performed LIF experiments studying OH in the afterglow of a nanosecond pulsed plasma discharge at temperatures below the auto-ignition threshold; CRDS, MOR, and CEMOR experiments studying OH concentrations in a lean methane-air slot burner; and developed a novel cw-CEMOR spectroscopy system to study small peroxy radicals in a flash photolysis facility.

Upon completion of his PhD, Michael plans to pursue a career in engineering consulting.